Diss. ETH No. 19460

Orographic forcing,
the key for heuristic nowcasting of rainfall
in the Alps

presented by
LUCA PANZIERA
Dipl. Meteor., University of Reading
born 25 August 1982
citizen of Italy

Contents

List of Figures

List of Tables

Abstract

Nowcasting of rainfall in the Alps is a very challenging task. In fact, the mountains strongly modify the mechanisms which produce precipitation, leading to an enhancement of rainfall on the windward slopes, and to a reduction on the lee-side. This process influences the spatial distribution of rainfall from mountain peak to mountain chain scales. As a consequence, strong gradients of rainfall are typically observed in the Alpine region. The large spatial variability of precipitation requires monitoring systems capable to measure rainfall with high spatial and temporal resolution, if the observations are to be used for nowcasting applications. Rain gauges networks are typically not dense enough to reproduce such high spatial variability, whereas **weather radar** is designed for this scope. In this thesis weather radar data are extensively used to create an heuristic tool for nowcasting precipitation in mountainous regions. The system takes advantage of the orographic forcing, which determines a strong relation between mesoscale flows, air-mass stability and rainfall patterns. The thesis consists of two articles.

The **first paper** builds the scientific framework necessary to develop the heuristic system. The relative importance of various environmental parameters in determining orographic precipitation patterns in the Lago Maggiore region in the southern part of the European Alps is investigated. Fifty-eight long-lasting and widespread orographic precipitation events corresponding in total to 106 days of rainfall are examined. The mesoscale winds are estimated by means of Doppler velocity radar measurements, within the layers whose mean wind velocity correlates best with rainfall in the mountains; air mass stability is computed from both radiosoundings and pairs of ground stations located at different heights. High-quality radar-derived rain rates at the ground are used to characterize the precipitation field.
The paper shows that upstream wind velocity has the largest impact on the intensity and frequency of precipitation over the orography, while the direction of the wind determines the spatial distribution of rainfall. Unstable conditions cause more precipitation over the mountains as compared to stable cases; however, differences in air mass stability have a minor impact on the precipitation intensity as compared to wind speed and direction. These findings show that the orographic forcing gives repeatability to the rainfall patterns typically observed in the region given particular environmental conditions.

The **second paper** describes how the findings of the first paper are used for nowcasting of rainfall in the mountains. The past situations with mesoscale flows, air-mass stability and rainfall patterns most similar to those observed at the current instant are identified by searching in a large historical data set; deterministic and probabilistic forecasts are then based on the rainfall observed by radar immediately after the analogous situations. Forecasts are updated every five minutes as new observations are available. The analog method used by the nowcasting system provides a natural way to incorporate into the prediction the evolution of precipitation and to express forecast uncertainty by means of ensembles.
A detailed evaluation of the skill of the system is also presented in the paper, and it shows that the heuristic tool performs better than Eulerian persistence for predictions with lead time larger than one hour, and better than numerical model COSMO2 for forecasts with lead time smaller than 4-5 hours.

Compendio

Il **nowcasting della pioggia nelle Alpi** é un obiettivo ambizioso. Infatti, le montagne influenzano i meccanismi che producono la precipitazione, causando un aumento della pioggia sui versanti sopravento ed una riduzione sui versanti sottovento. Questo processo domina la distribuzione spaziale della pioggia su scale spaziali diverse, da quella della singola cima a quella della catena montuosa. Di conseguenza nella regione alpina si osservano spesso gradienti di precipitazione molto marcati. La grande variabilitá spaziale della precipitazione richiede sistemi di monitoraggio capaci di misurare la pioggia con un'alta risoluzione spaziale e temporale, specialmente se le misure sono utilizzate da applicazioni di nowcasting. Di solito le reti dei pluviometri non sono abbastanza dense da riprodurre questa grande variabilitá spaziale, mentre **il radar meteorologico** é concepito proprio per questo scopo. In questa tesi i dati radar sono utilizzati per creare un sistema euristico di previsione a corta scadenza della pioggia orografica. Il sistema trae vantaggio dal forcing orografico, che determina una forte relazione tra i venti a mesoscala, la stabilitá atmosferica e i pattern di pioggia. La tesi é composta da due articoli.

Il **primo articolo** costituisce il fondamento scientifico del sistema euristico. In esso viene analizzata l'importanza relativa di vari fattori ambientali nel determinare i pattern della precipitazione orografica nella regione del Lago Maggiore nella Alpi meridionali. Cinquantotto eventi di precipitazione orografica duratura ed estesa, per un totale di 106 giorni di pioggia, sono esaminati. I venti a mesoscala sono stimati per mezzo di misure radar di velocitá Doppler negli strati verticali la cui velocitá media si correla al meglio con la pioggia nelle montagne; la stabilitá della massa d'aria é calcolata da radiosondaggi e da coppie di stazioni ubicate ad altezze diverse. Il campo di pioggia é caratterizzato da stime radar di alta qualitá.

L'articolo mostra che la velocitá del vento che va verso l'ostacolo orografico ha l'impatto maggiore sulla frequenza ed intensitá della pioggia sulle montagne, mentre la sua direzione determina la distribuzione spaziale della pioggia. Condizioni atmosferiche instabili causano precipitazioni maggiori rispetto ai casi stabili; tuttavia, le differenze in stabilitá atmosferica hanno un impatto minore sull'intensitá della precipitazione sulle montagne rispetto alla direzione e all'intensitá del vento. Questi risultati mostrano che il forcing orografico determina una certa ripetibilitá nei pattern di pioggia osservati con particolari condizioni ambientali.

Il **secondo articolo** descrive come i risultati del primo articolo sono usati per produrre previsioni di pioggia a corta scadenza per aree montuose. Le situazioni passate con i venti a mesoscala, stabilitá atmosferica e pattern di pioggia piú simili a quelli osservati al momento attuale vengono identificate in un vasto archivio storico; le previsioni deterministiche e probabilistiche di pioggia sono quindi basate sulla pioggia osservata da radar subito dopo queste situazioni analoghe. Le previsioni sono aggiornate ogni 5 minuti, non appena nuove osservazioni sono disponibili. Il meteodo degli analoghi usato dal sistema di nowcasting costituisce un modo naturale di incorporare nella previsione l'evoluzione della pioggia e di esprimere l'incertezza della previsione con un approccio ensembles. Una verifica dettagliata delle previsioni fornite dal sistema euristico mostra che esso produce previsioni di pioggia

migliori rispetto alla persistenza Euleriana se il lead time é piú lungo di un'ora, e migliori rispetto al modello numerico COSMO2 se il lead time é inferiore a 4-5 ore.

Chapter 1

Introduction

1.1 Aims and outline

The first objective of this study is to investigate to what extent the orographic forcing influences precipitation distribution on short spatio-temporal time scales. The investigation is aimed to build the scientific framework for the development of an heuristic system for nowcasting orographic rainfall. The system has to be developed in such a way that it can be used in an operational context, where forecasts of rainfall with high temporal and spatial resolution are needed with short updating frequencies.

The first chapter builds the broader context of orographic precipitation; the basic physical and microphysical elements of orographic rainfall are introduced, followed by a description of the current status of orographic precipitation diagnostic models. The issue of measuring precipitation in a mountainous region is also tackled. The last part of the chapter focuses on orographic precipitation nowcasting, and a concrete example from the Swiss Alps is provided. The second chapter introduces weather radar, which is the instrument upon which is based the nowcasting system built in this work. The methodologies used for the development of the system are presented in chapter 3. In particular, the analogue methods already applied to weather forecasting are revisited, and the methodology by which the wind is estimated by the nowcasting system from Doppler radar measurements is described. The core of the dissertation is presented in chapters 4 and 5, which correspond to the two following scientific papers:

Panziera, L. and U. Germann, 2010. The relation between airflow and orographic precipitation on the southern side of the Alps as revealed by weather radar. *Quarterly Journal of the Royal Meteorological Society*, **136**: 222-238.

Panziera, L., U. Germann, M. Gabella, P.V. Mandapaka, 2010. NORA - Nowcasting of Orographic Rainfall by means of Analogues. *Quarterly Journal of the Royal Meteorological Society*, in review.

The aim of the first article is to identify predictors of orographic precipitation: we search for the most important parameters which regulate the intensity and location of precipitation patterns over the mountains. The aim of this research is to find predictors that can be included in an heuristic nowcasting system of orographic precipitation. At the same time, through this research we also want to understand better the orographic precipitation mechanisms occurring in the Lago Maggiore region in southern Switzerland. We selected a large data set of orographic rainfall, consisting in total of 106 days. We make full use of radar observations of rainfall and wind, for the reasons explained in the previous sections. We identify four mesoscale flows which show a strong relation with orographic precipitation patterns in the Lago Maggiore region; moreover, we prove that also air mass stability can be regarded as a predictor of the intensity of rainfall.

The predictors identified in the first paper are used in the second paper to build an heuristic nowcasting system. The main idea is to look into the past for situations with the predictors most similar to those observed at the current instant. Deterministic and probabilistic forecasts are based on the rainfall observed by radar after the analogous situations. The historical data set was extended to 127 days of orographic rainfall. A verification of the forecasts shows the improvements of this new nowcasting tool with respect to the forecast given by the persistence of rainfall and by the numerical model COSMO2. A final discussion, together with an outlook, follows in chapter 6.

In the appendix the following paper is reported:

Mandapaka, P. V., U. Germann, L. Panziera and A. Hering, 2011. Evaluation of a radar-based lagangian extrapolation rainfall forecast technique (MAPLE) over complex orography. *Weather and Forecasting*, in review.

In such paper a semi-lagrangian extrapolation scheme (MAPLE) is employed to obtain very short-term rainfall forecasts over a large region broadly centered on Switzerland. The high resolution forecasts from MAPLE are then evaluated against the radar observations for 20 summer rainfall events by employing a series of categorical, continuous, neighborhood and spatial verification techniques. The verification results are then compared with Eulerian extrapolation forecasts and a high resolution numerical weather prediction model (COSMO2) forecasts. In general, Lagrangian persistence forecasts outperformed Eulerian persistence forecasts. Although MAPLE performed well for short lead times, the performance deteriorated rapidly with increase in lead time. The results also showed that the predictability of MAPLE model depends on the spatial correlation structure, and temporal evolution of the rainfall field. Some open questions related to the quantitative precipitation forecasting in a complex terrain are also discussed.

1.2   Orographic precipitation

Atmospheric flow is strongly modified by the presence of the mountains, over a wide range of spatio-temporal scales, extending from the scale of boundary layer motions up to that of planetary waves (Barros and Lettenmaier, 2010). One of the most evident effects of the interaction between atmospheric flow and mountains is orographic precipitation, which is the precipitation enhanced by an air flow ascending over a mountain. Pure orographic rainfall is unlikely to occurr, since it is observed a strong dependence of precipitation rates on such factors as cyclonic or frontal convergence, mesoscale convergence associated with mountain-valley winds, atmospheric instability and humidity contents. Thus, as reported by Barros and Lettenmaier (2010), it is more correct to refer to the orographic component of precipitation instead of orographic precipitation alone. The major influence of mountains on precipitation is observed when pre-existing atmospheric disturbances move into mountainous areas, where precipitation is amplified (Smith, 2006).

As reported by Rotunno and Houze (2007), three elements lead to orographic precipitation:

1. A moist, large-scale flow towards an obstacle (hill, mountain or mountain chain).

2. Mesoscale orographically induced lifting of the large-scale flow, which cools the air to saturation and induces condensation

3. Conversion of the condensate to precipitable particles.

These three components highlight how the mechanisms that produce orographic precipitation depend on both airflow dynamics and cloud microphysics, thus involving different spatial and temporal scales. The dynamic aspects depend on the upstream characteristics of the flow and on the terrain configuration, which together determine the ways in which the flow interacts with the orography; microphysical aspects determine how much and how quickly cloud water is converted into precipitation and how

fast precipitation falls (Smith et al., 2005).

One of the most evident features of orographic rainfall is the enhancement of precipitation that typically occurs on the windward slope of the mountains, while the leeward flank receives much less rainfall. This results in the well-known rain-shadow effect, which not only strongly influences the distribution of precipitation over the orography, but also is reflected in sharp transitions in climate, flora, and fauna across the divide. As reported in Roe (2005), the amplitude of the rain shadow and the relation between orography and precipitation at scales smaller than the mountain chain size are complex, and the subject of active research. For example, Foresti and Pozdnoukhov (2011) demonstrate that the enhancement of rainfall due to orography, which leads to stationary rainfall cells, occurs on the meso-gamma scale; moreover, they show that preferred regions for stationary cells are the upwind slopes and the top of hills, in agreement with Anders et al. (2007).

An example of the large spatial variability of orographic rainfall is given in Fig.1.1, where the precipitation accumulated in two heavy orographic precipitation events in the Southern Swiss Alps as measured by weather radar is represented. Such rainfall distribution is typically observed in the region when a cold front remains stationary over the Alpine crest, leading to strong south-easterly winds in the low levels, and accompanied by south-westerly winds in the upper levels. As it can be seen in the figure, there are very strong gradients of precipitation within a few kilometers. For example, in less than 10 kilometers north-west of Maggiore Lake rainfall accumulations can vary from less than 25 mm to more than 100 mm. Moreover, the highest accumulations can be concentrated in very small regions, with spatial scales of less than 5 kilometers.

The behavior of the three elements reported at the beginning of this section can vary greatly not only from one storm to another, but also during a single precipitation event. Orographic rainfall, therefore, is intrinsically a transient phenomenon (Roe, 2005). Precipitation rates can vary substantially even during the course of a single storm, as synoptic conditions change. The temporal scale of orographic precipitation, thus, may be rather short.
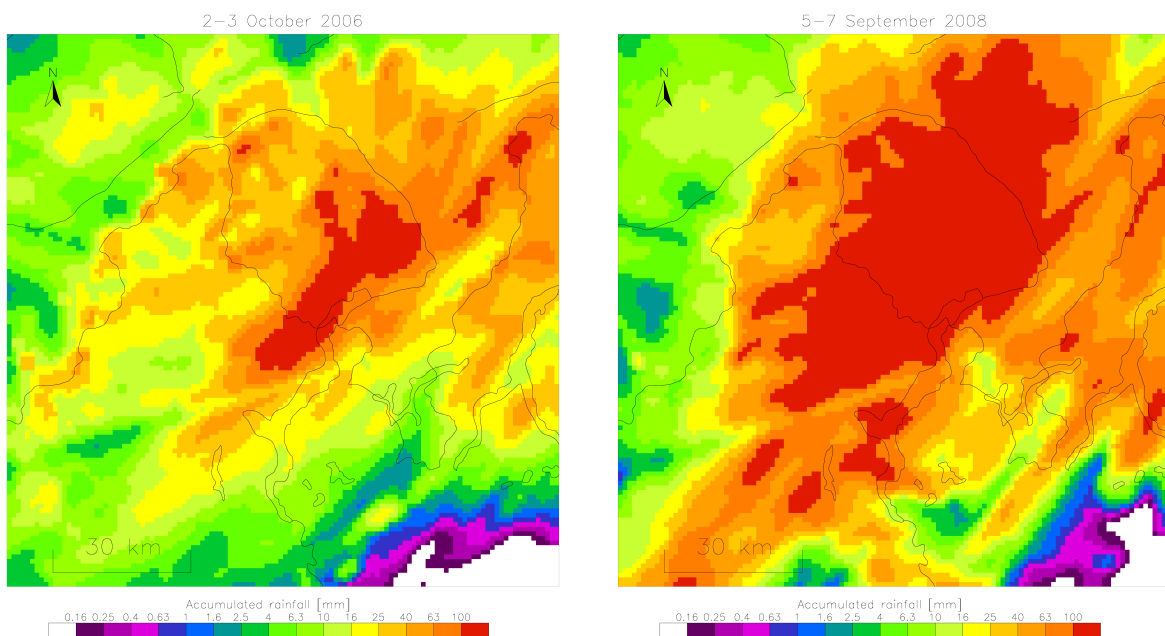
Figure 1.1: *Rainfall accumulated over the Southern Swiss Alps in two heavy orographic precipitation events as measured by weather radar. Black lines denote lakes, rivers and borders. Left: 31 hours of precipitation (2-3 October 2006). Right: 55 hours of precipitation (5-7 September 2008).*

1.2.1 Moist airflow dynamics

The nature of the interaction between mountains and the atmosphere depends on the relative position of the topographic barrier with respect to the location of incoming weather systems (Barros and Lettenmaier, 2010). The characteristics of both topography and synoptic disturbances also determine the way in which this interaction takes place. The terrain-induced ascent is dependent on the width of the hills (e.g. Smith, 1979a): whereas for narrow hills the vertical penetration of the forced ascent is limited to about the size of the obstacle, for wider hills density stratification and latent heat release are also to be considered.

A measure of the effect of density stratification, and therefore of the strength of the buoyancy force, is the Brunt-Väisälä frequency, which is the frequency at which an air parcel will oscillate whan subjected to an infinitesimal perturbation in a stably stratified atmosphere. In unsaturated air the Brunt-Väisälä frequency (N^2) is given by:

$$N^2 = \frac{g}{T}\left(\frac{dT}{dz} + \Gamma_d\right)$$

where T is the temperature of the atmosphere, Γ_d is the dry adiabatic lapse rate, and g is the gravitational acceleration. Under typical tropospheric conditions $\frac{dT}{dz} = -6.5°C/km$, $\Gamma_d = -0.98°C/km$, $T = 273°K$, so that $N = 0.01s^{-1}$. It follows that the natural buoyant oscillation period of the air is $T = 2\pi/N \approx 600s = 10min$. If the atmosphere is saturated, the Brunt-Väisälä frequency changes (e.g. Durran and Klemp, 1982). In fact, whereas in an unsaturated atmosphere an air parcel slightly displaced upward will cool by adiabatic expansion, in a saturated atmosphere upward displacements are accompanied by condensation and release of laten heat. This heating tends to compensate for the cooling associated with the adiabatic expansion, with the effect that the difference between the parcel and the surrounding air is less than in the dry case, and the buoyancy restoring force is decreased. Therefore, the Brunt-Väisälä frequency is lower in a saturated atmosphere with respect to an unsaturated environment. Various expressions for the saturated Brunt-Väisälä frequency have been derived in the literature (e.g. Dudis, 1972; Fraser et al., 1973). Lalas and Einaudi (1974) proposed the following expression:

$$N_m^2 = \frac{g}{T}\left(\frac{dT}{dz} + \Gamma_m\right)\left(1 + \frac{Lq_s}{RT}\right) - \frac{g}{1+q_w}\frac{dq_w}{dz} \tag{1.1}$$

where Γ_m is the saturated adiabatic lapse rate, q_s the saturation mixing ratio, L the latent heat of vaporization, R the ideal gas constant for dry air, and q_w the total water mixing ratio, i.e. the sum of q_s and the liquid water mixing ratio q_L. For a detailed explanation of the significance of the various terms of equation 1.1 see Durran and Klemp (1982). In this thesis we derive the moist Brunt-Väisälä frequency N_m^2 according to the expresison proposed by Durran and Klemp (1982):

$$N_m^2 = g\left\{\frac{1 + Lq_s/RT}{1 + \epsilon L^2 q_s/c_p RT^2} \cdot \left(\frac{dln\theta}{dz} + \frac{L}{c_pT}\frac{dq_s}{dz}\right) - \frac{dq_w}{dz}\right\} \tag{1.2}$$

where $\epsilon = R/R_v$ with R_v the gas constant for water vapor, c_p the heat capacity for dry air and θ the potential temperature of the atmosphere.

The behavior of a flow encountering an orographic barrier is commonly described by the two following scenarios: blocking and forcing the flow around a mountain or unblocking with subsequent lifting of the flow over the windward slopes. The accepted criterion which states which of these two conditions is based on the Froude number Fr:

$$Fr = \frac{U}{Nh} \tag{1.3}$$

where U is the upstream flow speed perpendicular to the terrain, N is the Brunt-Väisälä frequency (defined later) and H is the height of the mountain barrier. The Froude number indicates whether or not the upstream flow has enough kinetic energy to rise over the barrier (Durran, 1990; Houze, 1993). Flow with an high Fr rises easily over a mountain, resulting in a robust upslope flow which

can enhance precipitation over the windward side of the obstacle (unblocked situation); flow with low Fr tends to be deflected by the mountain, and lifting and enhancement of rainfall can also occurr upstream of the barrier (blocked situation). In order to take into account the effect of latent heat release caused by water vapor condensation during the ascent, N is to be replaced with N_m in the calculation of Fr. Since typical values of N_m are significantly less than N, often only one-half to one-third as large (e.g. $N_m \approx 0.005 s^{-1}$), moist air will could rise over hills two or three times as high as dry airflow could. Even though blocking phenomena strongly affect atmospheric dynamics in the vicinity of prominent mountain ranges, it does not appear to influence long-term precipitation distributions in a significant way. The latter, in fact, are dominated by the enhancement of rainfall observed over the widward slopes typical of unblocked situations.

1.2.2   Orographic precipitation mechanisms

As introduced in the previous subsections, orographically induced flow is able to produce or influence precipitating clouds. Figure 1.2, which is taken from Houze (1993), represents the mechanisms by which orographic precipitation is produced or enhanced. The seeder-feeder mechanism (panel (a)) results from the interaction between a non precipitating stationary cap cloud (feeder) and a precipitating cloud system (seeder) moving with passing fronts or cyclones. Small droplets falling from the higher cloud grow through coalescence with the droplets of the lower cloud, forming bigger drops. Since the atmosphere is close to saturation in the areas covered by the feeder cloud, and because the fall distances between cloud base and the ground are short, raindrop evaporation is small in this situation. This mechanism plays an important role in the enhancement of precipitation over small hills, that are too low to induce an ascent able to generate precipitating clouds. Panel (b) represents upslope condensation: if the air forced over a mountain is sufficiently moist through a large portion of the lifted layer, condensation may occurr through a deep layer. This mechanism is representative of an unblocked situation, in which the flow easily ascend over the barrier, as introduced in the previous subsection. Panels (c) to (g) of figure 1.2 represent different mechanisms by which flow over and around a mountain can trigger or enhance convection upstream of the mountain, on the windward slope, directly over the peak, on the lee slope, or downwind of the mountain. If the air flowing over the terrain is potentially unstable, the induced lifting can lead to the release of instability. In this case, the orographic clouds appear as cumulus or cumulonimbus rather than fog or stratus. Such clouds, that can produce large amount of rainfall, are largely governed by the dynamics of the convective clouds. However, as long as they remain in the vicinity of the mountain, a complex interaction between convective and orographic dynamic takes place. Triggering of convection can also be observed upstream of the orographic obstacle (panel (d)), as long as the lifting induced by the terrain is felt at the upper levels at a large distance upstream of the mountain. The blocking already introduced can be regarded as an upstream triggering of convection mechanism. Panel (e) represents thermal triggering of convection, which occurs when the heating during the day produces an heat source and a thermal circulation with convergence at the top of the mountain. The enhancement of convection may also happen in the lee of the mountain, in particular in low Froude number cases characterised by flow around an isolated obstacle (panel (f)). Finally, panel (g) depicts a situation in which the convection triggered on the windward slope over the crest of a ridge is enhanced on the lee side. The combined effect of midlevel upward motion associated with a vertically propagating wave induced by flow over a mountain and low level thermally induced flow leads to the enhancement of convection in the lee of the barrier.

1.2.3   Microphysical aspects

Orographic precipitation characteristics are strongly dependent on the microphysical processes that lead to the formation of clouds and precipitation. In fact, even though these processes operate at
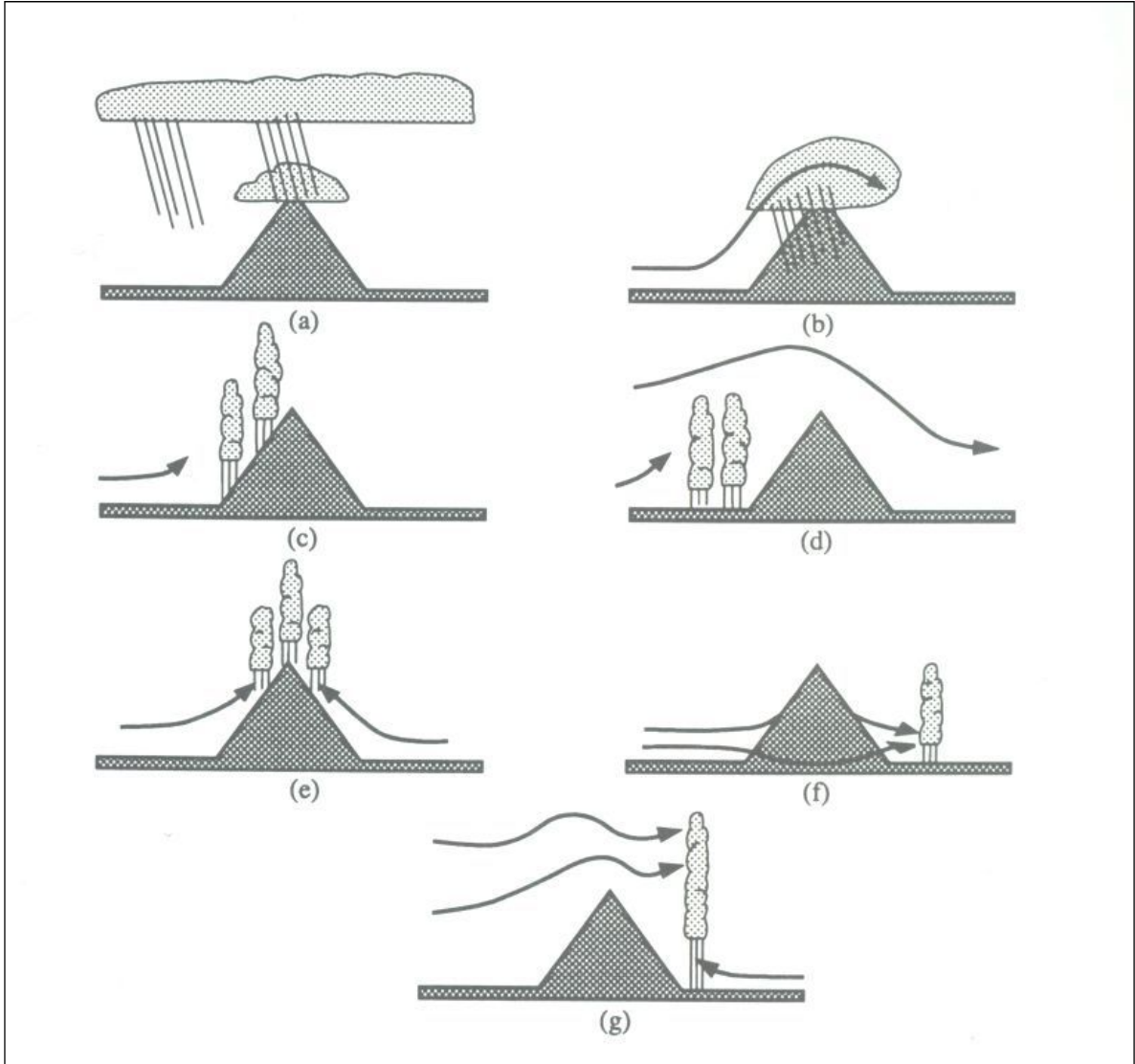
Figure 1.2: *Orographic precipitation mechanisms. (a) Seeder-feeder mechanism; (b) upslope condensation; (c) upslope triggering of convection; (d) upstream triggering of convection; (e) thermal triggering of convection; (f) lee-side triggering of convection; (g) lee-side enhancement of convection. Clouds are lightly stippled. Slanted lines below cloud base indicate precipitation. From Houze (1993).*

scales much smaller than those typically involved in orographic precipitation, their effects determine how condensation gets distributed over the landscape as precipitation (e.g. Roe, 2005).

The formation of clouds occurrs when moisture in the air exceeds its ability to carry water as vapor. A parcel will become saturated as long as the partial pressure of the water vapor within it, e, reaches a treshold value, the saturation vapor pressure e_{sat}. The latter is a function of temperature, as given by the Clausius-Clapeyron equation:

$$\frac{de_s}{dT} = \frac{L_{12}(T)}{(\alpha_2 - \alpha_1)(T)T} \tag{1.4}$$

where T is temperature, L_{12} is the latent heat of the transition from the phase 1 to phase 2, α_1 and α_2 the specific volumes. From equation 1.4 it is possible to obtain the saturation vapor pressure over water e_{sat} as a function of temperature:

$$e_s[mb] = 6.11 e^{5413.2(\frac{1}{273} - \frac{1}{T})} \tag{1.5}$$

6

Homogeneous nucleation of liquid drops from the vapor phase requires supersaturation levels (i.e., e/e_{sat}) of several hundreds percent, which are not observed in nature. As long as the atmosphere contains aerosol particles, however, condensation may occurr also in presence of lower supersaturation levels. This process is called heterogeneous nucleation, and the aerosol particles are referred to as cloud condensation nuclei (CCN). Ice particles can be nucleated through homogeneous and heterogeneous nucleation on so-called ice nuclei (IN). The concentration of CCN and IN affects the number and the evolution of the cloud particles: more CCN and IN lead to smaller and more numerous cloud particles for a given condensation rate. With fewer CCN and IN, on the other hand, a smaller number of cloud particles will condense, but they will reach large sizes, which mean larger fall speeds. The growth mechanisms also influence the evolution of the cloud particles: in warm clouds, with temperatures above 0°C, cloud droplets grow by the diffusion of water vapor onto the droplets (condensation), or by collisions between droplets creating bigger drops (coalescence). In cold clouds with temperatures below 0°C, ice particles can grow at the expenses of the supercooled water droplets, because the saturation vapor pressure over ice is less than that over liquid water at the same temperature (Bergeron-Findeisen mechanism). Freezing of supercooled droplets can also occurr onto ice particles (riming), leading to particles with large fall speed. In completely glacieted clouds, ice particles can also grow via diffusion of water vapor (deposition) and collision (aggregation). These growth mechanisms, as highlighted above, have also a strong relation with the observed patterns of orographic precipitation, as particles with lower fall speed can be advected for longer distances before reaching the surface (e.g. Hobbs et al., 1973).

For example, whereas in warm cumulus clouds growth through condensation and coalescence alone can be slow (30 to 60 minutes), condensation accreted onto falling hydrometeors via coalescence, riming or aggregation can be much faster (100 to 2000 s) (e.g. Smith and Barstad, 2004). Taking terminal velocities between 1 and 10 m/s (relative to snow and heavy rain respectively), and a range of horizontal wind speeds from 5 to 30 m/s, a particle originating at 3 km altitude can get advected anywhere between 1.5 and 90 km before reaching the surface. These conversion and fallout time scales are of primary importance in orographic precipitation, because the lifting caused by the terrain is temporary. The multitude of interactions and mechanisms by which cloud ice and cloud water particles grow and form precipitation, therefore, has a primary role in describing orographic precipitation features.

1.3   Orographic precipitation models

A large number of diagnostic models of orographic precipitation have been developed in the past. Such models calculate the atmospheric flow, the amplitude and the patterns of orographic precipitation for given large-scale atmospheric conditions, assuming a steady state. The simplest models consider the basic physics that orographic precipitation tends to increase with the steeper windward slopes due to the enhanced lifting and subsequent moisture condensation, and tends to decrease with elevation due to the exponential reduction in the quantity of the available moisture (Clausius-Clapeyron effect, see equation 1.4). These models consider the total condensation rate S in a vertical column of saturated air as the upper bound on the precipitation rate that can be achieved owing to stable upslope ascent, assuming that at every level the vertical velocity equals the orographically forced lifting at the surface (e.g. Sawyer, 1956; Smith, 1979b; Alpert, 1986):

$$S = -\int_{z_s}^{\infty} \vec{u} \cdot \nabla z_s \frac{d}{dz}(\rho q^{sat})dz = \rho_0 q_0^{sat}\vec{u} \cdot \nabla z_s e^{-z_s/H_m} \qquad (1.6)$$

where z_s is the surface elevation, $\vec{u}$ the wind speed, ρ the air density, q^{sat} the saturation mixing ratio. In this basic model the generation of condensation decreases exponentially with height, which is an important effect for mountains with elevations comparable to the moisture scale height (comprised between 2 and 4 km depending on season and latitude). This is also the main reason for which on

such ranges maximum precipitation rates are observed on the windward slopes. For typical midlatitudes values ($|\vec{u}| \simeq 10m/s, \nabla z_s \simeq 2/50$, $\rho_0 \simeq 1.2kg/m^3$, $q_0^{sat} \simeq 8g/kg$), and surface wind normal to the local slope, equation 1.6 gives $S = 14mm/h$. Simple orographic pecipitation models based on such kind of simple physics need a downwind smoothing of the condensation rate to generate precipitation rates consistent with observations, and to produce rainfall also on the leeside. This correction is required in order to take into account the growth and downwind advection of hydrometeors. Precipitation efficiency is defined as the ratio of the measured precipitation to S, and it is commonly used as a measure of the effectiveness with which moisture is removed from the atmosphere by the orography.

The behavior of the atmospheric flow in presence of a mountain and the generation of orographic rainfall are calculated in a more realistic way by diagnostic models which take into account also effects other than instantaneous fallout of condensed water. For example, Hobbs et al. (1973) and Bader and Roach (1977) included a description of raindrop and snow fall speed and washout of cloud water. The advection of hydrometeors was taken into account in the models developed by Alpert and Shafir (1989), Sinclair (1994) and Smith et al. (2003). The agreement between the precipitation produced by such models and station and radar data was improved, due to the drift distances. However, as discussed in Smith and Barstad (2004), these simple upslope-advection models have two major limitations. First, the assumption that the terrain-induced vertical velocity penetrates upwards through the moist layer without changes, thus neglecting that such motions may either decay or oscillate with altitude, depending on the features of the mountain, static stability and wind speed. This cause an overestimation of the condensation rate. The second limitation is the assumption that only upslope regions influence precipitation. If instantaneous conversion and fallout is assumed, only the windward slope will receive rainfall; when including time delays, precipitation is produced also downstream, but the evaporation of hydrometeors caused by descending air is not considered, again overestimating the total precipitation. The overestimation of rainfall resulting from these two effects can reach a factor of 5 if the terrain rises with scales of 20 km or less, while the results are more reasonable for smooth hills with scales of 100 km. Smith et al. (2003) showed that the upslope rainfall estimate for the Italian Alps was so much overestimated to exceed the incoming moisture flux, an obvious violation of water conservation principle.

The orographic precipitation model of Smith and Barstad (2004) is simple to apply and has a small set of free parameters, including the basic physical elements: airflow dynamics, condensed water conversion, delays and downstream advection and fallout of hydrometeors, and downslope evaporation. It is analytically tractable so that its properties can be easily understood, and it is applicable to actual complex terrain and arbitrary wind direction so that it can be tested against real data. The model is based on the equation for the advection of vertically integrated condensed water:

$$\vec{U} \cdot \nabla q_c = S(x,y) - q_c/\tau_c \tag{1.7}$$

and for the advection of hydrometeors:

$$\vec{U} \cdot \nabla q_f = q_c/\tau_c - q_f/\tau_f \tag{1.8}$$

where $q_c(x,y)$ is the cloud water density, $q_f(x,y)$ the hydrometeor density, τ_c the constant characteristic time scale for cloud water conversion, τ_f the constant characteristic time scale for hydrometeor fallout. Such time constants were estimated to be between 200 and 2000 s (e.g. Smith et al., 2003). The advecting wind vector $\vec{U}$ is assumed to be independent of time and space. $S(x,y)$ is the source term of cloud water, the sum of a background rate of cloud water generation and local variations created by terrain-forced uplift. If the background rate is neglected, $S(x,y)$ reduces to the raw upslope model of Smith (1979a), i.e. $S(x,y) = \rho_{v0}\vec{U}\nabla h(x,y)$, where ρ_{v0} is the average water vapor density at the surface and $\nabla h(x,y)$ the terrain slope. The final term in equation 1.7 is the conversion of cloud water to hydrometeors, which appears as a source term in equation 1.8. The final term in 1.8 is the loss of hydrometeors associated with precipitation. To obtain the general solution for the orographic precipitation, equations 1.7 and 1.8 can be solved using Fourier transforms in the two

horizontal directions (Smith et al., 2003). See Smith and Barstad (2004) for further details.

Both the pattern of precipitation and the total amount of rainfall predicted by this model can be described by two nondimensional parameters. First, the nondimensional moist layer depth

$$H = NH_w/U \tag{1.9}$$

where N is the moist stability frequency, H_w the water vapor scale height, U the magnitude of the wind. Large values of H reduce the amount of condensation, as the uplift does not penetrate the moist layer. Second, the nondimensional cloud drift time

$$\tilde{\tau} = U\tau/a \tag{1.10}$$

where τ is the conversion and fallout time, a the mountain half-width. Large values of $\tilde{\tau}$ indicate that condensed water will drift onto the lee slopes and evaporate, instead of converting and falling on the windward slopes. Therefore, the location of maximum precipitation is determined by a competition between the upstream shift caused by dynamics and the downstream shift caused by cloud delays. Its location shifts from the windward slopes to the hilltop as mountain width decreases. For narrow mountains and high wind speeds, spillover is possible. The amount of precipitation depends on the vertical penetration of the forced ascent relative to the depth of the moist layer and by the conversion and fallout delay times.

Several strong assumptions are made in the formulation of the model of Smith and Barstad (2004): linear steady wave dynamics, near saturation, constant wind and moist stability with height and location, constant time delays, equal hydrometeor growth and decay times. The model only treats the vertically integrated condensed water. Both the airflow and condensed water formulations become problematic in situations with fast conversion and fallout and persistent descent, and in an unstable atmosphere. Barstad and Smith (2005) present an evaluation of the orographic precipitation model comparing the predicted rainfall rates with data from three field camapigns. They also consider observations taken during the Mesoscale Alpine Program, that took place in the fall season of 1999 (Bougeault et al., 2001). One of the target areas of this project was the Lago Maggiore region in the central southern part of the Alps, the same region which is studied in this dissertation. Barstad and Smith (2005) compare the model results with the observations for the events MAP IOP2b and IOP8. The first was warm and nearly unstable, with some embedded convection, whereas the second was cold, stable with some low-level blocking. Since the model of Smith and Barstad (2004) is steady, the comparison was performed by averaging the time series for the most intense precipitation period of each event, and giving a single value for each station; the model data are then interpolated to the station location. Barstad and Smith (2005) also identify other challenges in evaluating an orographic precipitation model: poor data coverage, errors in the observations, uncertainty in the model input variables and misleading statistical measures of goodness. They demonstrate that the model of Smith and Barstad (2004) performs better than simple upslope models, but with rainfall predictions that hardly reflect the observed precipitation. The main reason for this is that the flow steadiness assumption is not supported by the behavior of the observed orographic precipitation. Thus, the usage for operational forecasting of precipitation of orographic precipitation models as the one of Smith and Barstad (2004) is strongly limited, mainly because the assumptions already illustrated require a too simplified flow behavior.

1.4   Precipitation measurements in the mountains

The large spatial variability of orographic precipitation requires monitoring systems capable to measure rainfall with high spatial and temporal resolution. This requirement is particularly important if the precipitation data are to be ingested in nowcasting systems, which need frequently updated information on rainfall rates observed with the highest possible spatial resolution. Rain gauges and ground-based radars constitute the two main systems for monitoring precipitation over the mountains.

1.4.1 Rain gauges

It has long been recognized that rain gauges networks are typically not dense enough to reproduce the high spatial variability of orographic precipitation. For example, in 1961 Bergeron wrote: "I venture to state that in no country is the official network of rainfall stations dense enough to give even just a summary picture of the precipitation conditions "(Bergeron, 1961). Precipitation measurement by means of rain gauges is particularly critical in the mountains, where the representativity of point measurements is very limited and rain gauges are sited preferentially in valleys (Frei and Schar, 1998). Even in the European Alps, one of the regions with the densest rain gauge network, typical spacing between stations is 10 km (Frei and Schar, 1998), whereas the precipitation distribution varies at scales smaller than 10 km (Smith et al., 2003). Moreover, gauges suffer from a number of errors as, for example, inappropriate siting, the disturbance of local airflow (e.g. Nespor in Joss et al., 1998), the undercatch of blowing snow or catching of snow drifted by wind.

1.4.2 Ground-based radars

Ground-based radars are designed to monitor precipitation over large areas with high spatial and temporal resolution. Therefore, they are widely used for developing nowcasting applications. However, using weather radars for precipitation measurements in mountainous regions is a challenge. In fact, ground clutter and beam shielding strongly affect the accuracy of radar estimates, and need to be treated properly if quantitative estimates of precipitation amounts are to be produced in a routine manner (Joss and Waldvogel, 1990). Other factors, both instrumental and meteorological, influence radar rainfall estimates: instability of the hardware, enhancement of the signal by melting snow (Austin, 1987b), vertical profile of reflectivity (Joss and Waldvogel, 1990; Kitchen et al., 1994; Joss and Lee, 1995; Vignal et al., 1999; Germann and Joss, 2002; Bellon et al., 2005), overshooting in shallow precipitation (Koistinen et al., 2004), signal attenuation in heavy rain (Delrieu et al., 1991), signal attenuation by water on the radome (Germann, 1999), non-uniform beam filling, variations in rain-drop size distributions (Joss and Gori, 1978; Sempere-Torres et al., 1994; Lee and Zawadzki, 2005) and enhancement of the signal by the presence of hail (Austin, 1987b).
The MeteoSwiss approach to radar precipitation measurements, resulting from more than 40 years of research in this field, is illustrated in Joss et al. (1998) and Germann et al. (2006). Significant improvements were obtained optimizing hardware stability and data processing (Cavalli, 1998; Joss et al., 1998; Germann and Joss, 2004). Recent modifications in the algorithms of rainfall estimation resulted in a significant reduction of bias, scatter and false alarms (Germann et al., 2006). The quantitative precipitation estimation product has been specifically developed for a mountainous region; it has 1 square km resolution and is updated in real-time every 5 minutes. The C-band Doppler weather radar network of MeteoSwiss consists of the three radars located on Monte Lema, La Dole and Albis (see Fig.1.3).
A detailed description of the functioning of weather radars will follow in section 1.6.

1.5 Nowcasting of orographic precipitation

Orographic rainfall is responsible for most of the floods which affect the Alpine region. During intense precipitation events, meteorological and hydrological services need frequently updated very short-term predictions of the intensity, location and evolution of orographic rainfall. Thus, nowcasting tools, covering the 0-6 hours time frame, assume high importance in the last stage of the weather forecasting process, as recently confirmed by the hydrometeorological forecast demonstration project MAP D-PHASE (Rotach and co authors, 2009) and IMPRINTS (http://imprints-fp7.eu).
A lot of field experiments conducted in the last twenty years were devoted to precipitation over complex terrain: TAMEX (Kuo and Chen, 1990), CALJET (Ralph et al., 1999), IMPROVE (Stoelinga

Figure 1.3: *The MeteoSwiss radar network.*

et al., 2003), MAP (Rotunno and Houze, 2007). The main objective of these projects was a better understanding of orographic precipitation mechanisms, without giving a special emphasis to nowcasting issues. Thus, there is a lack of nowcasting systems specifically developed for orographic rainfall. The inclusion of orographic precipitation producing mechanisms in nowcasting tools is the subject of active research. Recently Roberts et al. (2010) employed high resolution observations collected during TiMREX (Lee et al., 2007) over Taiwan to examine storm formation and evolution, with the aim to develop a tool for nowcasting heavy orographic rainfall.

Nowcasting of precipitation in mountainous regions is a very challenging task, because of the complexity of the meteorological phenomena occurring over the orography and the difficulty to obtain detailed and precise observations of rainfall (Mecklenburg et al., 2000). In fact, the mechanisms that produce orographic precipitation depend on both airflow dynamics and cloud microphysics, thus involving different spatial and temporal scales, as described in detail in section 1.2.

The usage of numerical models, which are the main source of information in weather forecasting, has some limitations in the nowcasting time frame. Even though they include the full set of equations which describe the atmospheric processes, there are some limitations to their usage for operational nowcasting of precipitation. First, current numerical models are not able to fully digest the observations at the scale required by the applications. Second, the assimilation and the initialisation cycles and the time required to obtain the forecast are too long with respect to the demands of the forecasters and end users. Third, the spatial resolution and the updating frequency of the forecasts are too coarse for nowcasting applications. For example, COSMO2 numerical model (http://cosmo-model.org) is updated every 3 hours, the forecasts require about 2 hours to be computed and disseminated, and the spatial resolution of 2.2 km enables to resolve processes occurring on the spatial scales of 8 km or larger. Such values are too coarse for the nowcasting requirements. Most of the radar-based nowcasting techniques, on the other hand, do not suffer from these limitations. However, such methods do not take into account growth and dissipation of precipitation, which are fundamental processes to

11

be considered in forecasting orographic rainfall.

An attempt to adjust numerical weather prediction forecasts of rainfall over the mountains with observations is made by Neiman et al. (2009). They combine wind observations from wind profiling radars with vertically integrated water vapour measurements derived from GPS to estimate the bulk transport of water vapour. The resulting real-time diagnostic water vapour flux tool is used to evaluate and to improve numerical model forecasts over the mountains.

1.5.1 The challenge of nowcasting rainfall in the mountains: an example from the Swiss Alps

Fig.1.4 shows four Alpine catchments located in the Swiss Alps near the Monte Lema radar. In these basins, heavy and persistent orographic precipitation combined with rapid runoff can lead to flash floods, which are characterized by rapid occurence resulting in a very limited opportunity for warnings to be issued. For example in Verzasca Valley, a small and steep catchment (186 km^2), the time between a precipitation impulse and the main runoff response at the outlet (time of concentration) is on the order of 1 to 2 hours (Germann et al., 2009). This means that coupling radar observations with a runoff model results in 1-2 hours lead time for predicting a flash flood peak, if no precipitation forecast is available. Nowcasting of orographic rainfall is aimed to extend such short lead times. The large spatial variability of orographic rainfall, on the other hand, makes this task very difficult, as errors of a few kilometers in the location of the predicted rainfall, if negligible for large catchments, can have a large impact on river runoffs of small basins. Moreover, it is not trivial to have reliable precipitation measurements over the orography, for the reasons explained in section 1.4; very few rain-gauges of those shown in Fig.1.4 register data every 10 minutes. Fig.1.5, on the other hand, shows how radar beams can be shielded by mountains, highlighting the difficulties to estimate rainfall at the ground level in the inner alpine valleys. To conclude, the challenge of nowcasting methods is to provide forecasts of precipitation up to 6-8 hours ahead, with an updating frequency not larger than 1 hour and a spatial resolution of a few kilometers.

1.6 Weather radar

In this section weather radar is illustrated. Section 1.6.1 introduces the radar equation, section 1.6.2 the Doppler velocity.

The four main components of a weather radar are:

1. the transmitter, which generates the high-frequency signal

2. the antenna, which sends the signal out into space and receives the echo back from the target

3. the receiver, which detects and amplifies the signal to make it strong enough to be useful

4. the visualization system, in order to see what the radar detects.

In Monostatic radars the same antenna is used for both transmitting and receiving the signal. If two different antennas are used, the radar is called bistatic.

1.6.1 Radar equation

In this section the equation that relates the power received by the radar with the power transmitted is derived, following Rinehart (2004). We begin by considering a point target. The energy that is transmitted by an isotropic antenna is directed into space by the antenna, and it propagates at the
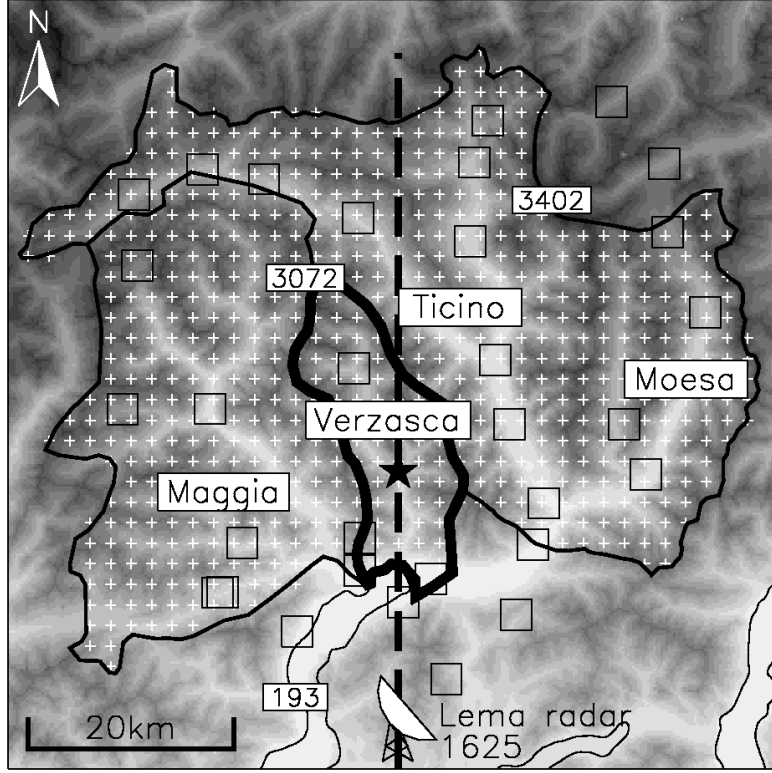
Figure 1.4: *Example of Alpine catchments. Three- and four-digit numbers are heights (m asl) of lakes and mountain peaks. Square boxes indicate the location of rain-gauges which measure daily accumulations (only five of them register data every 10 minutes). The black star shows the location of the Verzasca hydrometer. Fig.1.5 shows a vertical cross-section along the thick dashed line. From Germann et al. (2009).*

speed of light, forming a spherically expanding shell of energy. The area covered by a single, expanding pulse of energy is equal to the area on the surface of a sphere at the corresponding distance:

$$area = 4\pi r^2 \tag{1.11}$$

where r is the range from the radar, the radius of the sphere. The transmitted power p_t divided by this area is the power density S, the power per unit area:

$$S = p_t/4\pi r^2 \tag{1.12}$$

In the case of a real antenna, the amount of power along the center of the beam axis at some distance is greater than it would be if an isotropic radiator is used. This increased power is given by the gain g of the antenna times the power that would have been there if an isotropic antenna had been used. Introducing a target with an area A_σ, the power that it will intercept is:

$$p_\sigma = p_t g A_\sigma/4\pi r^2 \tag{1.13}$$

where subscript σ represents the target. Such power intercepted by the target is reradiated isotropically back into space, and some of this energy is received back by the radar (p_r):

$$p_r = p_\sigma A_e/4\pi r^2 = p_t g A_\sigma A_e/(4\pi^2)r^4 \tag{1.14}$$

where A_e is the effective area of the receiving antenna, that can be written also as a function of the gain of the antenna and the wavelength λ of the radar:

$$A_e = g\lambda^2/4\pi \tag{1.15}$$

13
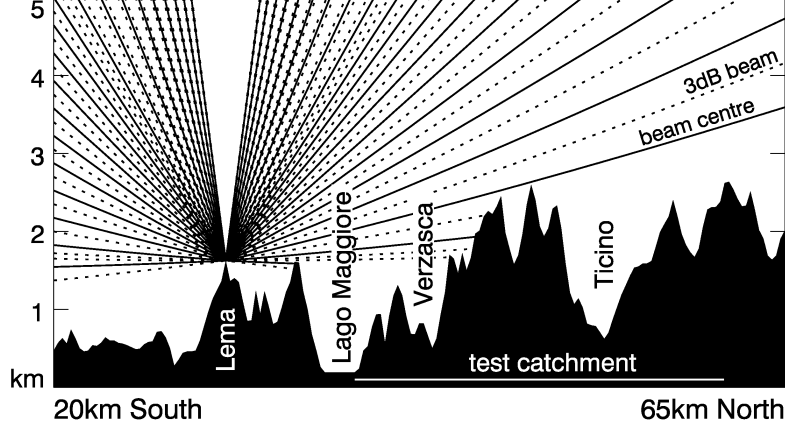
Figure 1.5: *Vertical cross-section of Monte Lema radar scan geometry over the catchments shown in Fig.1.4. the cross-section clearly reveals severe shielding of the radar beam by mountains and increasing pulse volume with increasing distance from the radar antenna. From Germann et al. (2009).*

Substituting this expression in equation 1.14 we get:

$$p_r = p_t g^2 \lambda^2 A_\sigma / 64\pi^3 r^4 \tag{1.16}$$

The area of the target A_σ should be replaced in this equation with a parameter σ called the backscattering cross-sectional area, which is a function not only of the size, shape and kind of matter making up the target but also of the wavelength of the radar. The backscattering cross-sectional area, which has the units of area, cannot always be calculated analytically. Since most of the hydrometeors are approximately spheres, we assume the meteorological target to be spherical. If the sphere is larger than the wavelength of the radar (i.e. $D/\lambda > 10$), the backscattering cross-sectional area of the target σ is equal to the geometric area:

$$\sigma = \pi r^2 \tag{1.17}$$

If the sphere is smaller than the wavelength of the radar (i.e. $D/\lambda < 0.1$, Rayleigh region), σ is proportional to the sixth power of the diameter D:

$$\sigma = \pi^5 |K|^2 D^6 / \lambda^4 \tag{1.18}$$

where $|K|^2$ is a parameter related to the complex index of refraction of the material. In the Mie or resonant region, the diameter of the sphere is comparable with the wavelength; in this case the backscattering cross-sectional area can also decrese with increasing size of the particle.

Weather radars, however, do not observe point targets: within the sample volume scanned by the radar, there are many raindrops or cloud particles at the same time. For example, in continental clouds $2 \cdot 10^8$ cloud droplets are contained in a cubic meter; for a radar with a $1°$ antenna beamwidth, the beam will be 1 km in diameter at a range of 57 km. If the radar uses $1\mu s$ pulse length, the effective sample volume in space will be 150 m. Therefore, $2 \cdot 10^{16}$ cloud droplets are scanned simultaneously within the same volume scan. If we consider only raindrops, typical densities are on the order of a few to a few hundred per cubic meter. Thus, in a single radar sample volume there might be something like 10^9 to 10^{12} raindrops. The total backscattering cross-sectional area of a meteorological target σ_t is the sum of all the individual backscattering cross-sectional areas σ_i:

$$\sigma_t = \sum \sigma_i \tag{1.19}$$

The volume of a radar pulse can be written as:

$$V = \frac{\pi r^2 \theta \phi h}{16 ln(2)} \tag{1.20}$$

where θ and ϕ are the horizontal and vertical beamwidths, r is the distance from the radar to the sample volume, h the pulse length. Substituting this equation and equation 1.19 into the radar equation for a point target (eq. 1.16), the radar equation for a beam-filling meteorological target is obtained:

$$p_r = \frac{p_t g^2 \lambda^2 \theta \phi h \sum \sigma_i}{1024 ln(2) \pi^2 r^2} \tag{1.21}$$

Substituting equation 1.18 in 1.21:

$$p_r = \frac{\pi^3 p_t g^2 \theta \phi h \left|K\right|^2 \sum D_i^6}{1024 ln(2) \lambda^2 r^2} \tag{1.22}$$

which serves to calculate the power received from a sample of raindrops, provided that we know the diameters of all the raindrops in an unit volume. Since this does not happen, a parameter called the radar reflectivity factor z is defined:

$$z = \sum_{vol} D^6 \tag{1.23}$$

Substituting this equation in 1.22 we get:

$$p_r = \frac{\pi^3 p_t g^2 \theta \phi h \left|K\right|^2 zl}{1024 ln(2) \lambda^2 r^2} \tag{1.24}$$

which is a general equation that can be applied to any radar for particles in the Rayleigh region. The term l was introduced in order to take into account the attenuation; it is always between 0 and 1. Since all of the parameters associated with a specific radar can be grouped together as a constant (p_t, g, θ, ϕ, λ and t) which also include the term $\left|K\right|^2$, the radar equation can be simply written as:

$$p_r = cz/r^2 \tag{1.25}$$

Therefore, the power received by a given radar is proportional to the radar reflectivity factor of the storm and inversely proportional to range squared.

Since the reflectivity factor is a parameter that depends on the number and size of the hydrometeors present in a sample volume, it can range from very small values in fog to very large values in very large hail. Thus it is convenient to compress it to a smaller range of values. The most common way to do this is to use logarithmic values instead of a linear scale. The logarithmic radar reflectivity is defined as:

$$Z = 10 \cdot log_{10} \left(\frac{z}{1mm^6/m^3} \right) \tag{1.26}$$

where Z is the logarithmic radar reflectivity factor measured in units of σ (i.e., decibels relative to a reflectivity of $1mm^6/m^3$), and z is the linear radar reflectivity factor in mm^6/m^3. Logarithmic radar reflectivity values can range from -30 dBZ for fog and +76.5 dBZ for large hail.

1.6.2 Doppler velocity

When a stationary radar observes moving targets, these will shift the frequency of the radar signal an amount depending on their speed. Considering a single target at a distance r from the radar, the total distance a radar pulse will have to travel to detect this target is $2r$ since the wave has to go out to the target and back to the radar. Thus, in terms of the number of wavelengths from the radar to the target, the distance will be:

$$dist[wavelengths] = 2r/\lambda \tag{1.27}$$

In terms of radians:

$$dist[radians] = (2r/\lambda) \cdot 2\pi = 4\pi r/\lambda \tag{1.28}$$

If a radar signal is transmitted an initial phase of ϕ_0, then the phase of the returned signal will be:

$$\phi = \phi_0 + 4\pi r/\lambda \tag{1.29}$$

whereas the change of phase with time between two successive pulses will be:

$$\frac{d\phi}{dt} = \frac{4\pi}{\lambda}\frac{dr}{dt} \tag{1.30}$$

where

$$V = \frac{dr}{dt} \tag{1.31}$$

is the velocity of the object.

The time rate of change of phase is the angular frequency ω:

$$\omega = \frac{d\phi}{dt} = 2\pi f \tag{1.32}$$

where f is the frequency shift in cycles per second (hertz). By combing equations 1.30, 1.31 and 1.32, the frequency shift caused by a moving target can be obtained:

$$f = \frac{2V}{\lambda} \tag{1.33}$$

The frequency shift caused by a target moving relative to the radar, therefore, is linearly proportional to the velocity and inversely proportional to the wavelength. As a result, the frequency shift is dependant only on the velocity of the target.

However, there are limitations in the velocities and ranges that a weather radar is able to resolve unambiguously. First, if a target is not moving towards or away from the radar, it will have zero radial velocity, but this does not necessarily mean that the target is stationary: any movement would be perpendicular to the radar beam. Moreover, there is a limit in the phase shift a radar can detect: the maximum velocity a Doppler radar can detect correctly or unambiguously is given by the velocity which produces a phase shift of $\pm\pi$ radians. This is called the Nyquist frequency or Nyquist velocity:

$$V_{max} = \pm f_{max}\lambda/2 \tag{1.34}$$

$$f_{max} = PRF/2 \tag{1.35}$$

where PRF is the pulse repetition frequency of the radar. Thus, the maximum unambiguous velocity detectable by a Doppler radar is:

$$V_{max} = \pm PRF\lambda/4 \tag{1.36}$$

Therefore, if we want to be able to detect high velocities, we must use long wavelengths, larger PRFs or both.

The rate at which the radar transmits the pulses is given by the PRF. So the time T between pulses is:

$$T = 1/PRF \tag{1.37}$$

The maximum range a radar signal can travel and return before the successive pulse is sent out is:

$$r_{max} = cT/2 = c/2PRF \tag{1.38}$$

The combination of maximum unambiguous velocity and maximum unambiguous range originate two constraints which must be considered in choosing the PRF for a Doppler radar. In fact, by solving both equations 1.36 and 1.38 for PRF and equating them:

$$v_{max}r_{max} = c\lambda/8 \tag{1.39}$$

This has been called the Doppler dilemma: since the right side of the equation is a constant for a given radar, if we want to have large v_{max} we need to have small r_{max}. On the other hand, if we want to detect echoes at long ranges, we can only detect unambiguous velocities at small ranges.

1.7 Methodologies

1.7.1 Analogue methods

Forecasting using analogues is one of the oldest methods for weather forecasting; the word *analogues* means two states of the atmosphere which resemble each other rather closely (Lorenz, 1963). The main hypothesis of analogues based forecasting is that similar atmospheric conditions will evolve in similar ways. Thus, once an analogue is found for the current situation, the forecast for a given period of time can be obtained by the evolution of the meteorological conditions observed after that similar past situation (e.g. Duband, 1970; Radinovic, 1975; Bergen and Harnack, 1982). The major limitation of the analogue approach is the size of the archive in which the analogues are searched, which has to be very long for the global scale (e.g Toth, 1991; Van den Dool, 1994). However, it is possible to find good analogues even in short data sets if the search for analogues is performed over a small area, in particular if the flow is persistent (e.g. Van den Dool, 1989; Root et al., 2007). The advantages of analogue forecasting lies in its simplicity: although it does not introduce any simplification in the physics of the atmosphere, it can provide realistic weather forecasts (e.g. Radinovic, 1975; Bergen and Harnack, 1982; Van den Dool, 1989). In fact, the past observed values used to make the forecast contain the orographic, diabatic and other local effects which characterize the area of interest and influence the behavior of the quantities to be predicted (e.g Ruosteenoja, 1988; Obled et al., 2002; Diomede et al., 2008). With the advent of fast computer processors, analogue forecasting is now applied to a large variety of problems (e.g. Fraedrich et al., 2003; Bo et al., 2009).

In this work an analogue method is applied for the first time to the issue of nowcasting precipitation over the orography at the mesoscale, over short time scales. The analogues are found by means of specific predictors observed to have a strong relation with orographic precipitation at the mesoscale (four winds and air mass stability) and by means of properties derived by the radar image. This constitutes a novelty with respect to previously developed analogue methods used to forecast rainfall, which searched the analogy at a larger scale through synoptic maps (e.g. Obled et al., 2002; Diomede et al., 2008). In their case, the analogy criterion had to compare two gridded fields, such as surface pressures, geopotential heights, temperatures, and to assign an index of similarity between them. Scores as S1 score, mean squared error or anomaly correlation (e.g. Wilks, 1995) can be used for this aim. However, such scores do not take into account the circulation pattern: two fields can be reasonably close in absolute departure, while undulating in opposition of phase with different centres of action. Obled et al. (2002) used the Teweless-Wobus score (Teweless and Wobus, 1954), as it emphasises analogy in shape, and therefore in circulation, between two fields. The Teweless-Wobus score considers, for any grid node, the south-north (i) and west-east (j) gradients:

$$TW = \frac{\sum_i \left| e_G^i \right| + \sum_j \left| e_G^j \right|}{\sum_i \left| G_L^i \right| + \sum_j \left| G_L^j \right|} \tag{1.40}$$

where e_G is the difference, around a given node, between the geopotential gradients selected for the two fields, and G_L is the maximum of these two gradients in the direction considered. When multiplied by 100, TW varies between 0 (for perfectly parallel fields) and 200 (if the two fields undulate in complete phase opposition). A score of 100 corresponds to totally independent fields.

In this work the analogy has not to be searched between two gridded fields, but rather considering a set of predictors that do not vary within the region of interest. In particular, as it will be illustrated in chapter 5, the quantities used as predictors are 4 mesoscale winds, air mass stability, the portion of the radar image exceeding a certain rain rate threshold and the average rainfall of the radar image. For this reason we work in a so-called phase-space, which in essence is a coordinate system in two or more dimensions (e.g. Benestad et al., 2008). In such space, any ipotetical state can be described entirely by a number of predictors equal to the number of its dimensions. The similarity criterion that we selected, able to identify the most similar situations within this space, is the Euclidean distance, which is the

17

distance between two points that one would measure with a ruler. The Euclidean distance between two points $\vec{x}$ and $\vec{y}$ is the length of the line segment connecting them. In Cartesian coordinates, if $\vec{x} = (x_1, x_2, ..., x_n)$ and $\vec{y} = (y_1, y_2, ..., y_n)$ are two points in Euclidean n-space, then the distance from $\vec{x}$ to $\vec{y}$, or from $\vec{y}$ to $\vec{x}$, is given by:

$$d(\vec{x}\vec{y}) = d(\vec{y}\vec{x}) = \sqrt[2]{(x_1 - y_1)^2 + (x_1 - y_2)^2 + ... + (x_n - y_n)^2} = \sqrt[2]{\sum_{i=1}^{N}(x_i - y_i)^2} \qquad (1.41)$$

As it will be illustrated in chapter 5, we calculate Euclidean distance between the observed predictors and the predictors measured in a large historical data set. The points of the archive with the smallest Euclidean distance are assumed to be the most similar to the current observed situation.

1.7.2 Wind estimation from radar

An algorithm has been developed in order to estimate the direction and the intensity of the mesoscale wind in specific areas (horizontally and vertically limited) of the volume scanned by the radar from Doppler velocity measurements. It has been created for the estimation of the flows which play a fundamental role in the evolution of orographic precipitation in the Lago Maggiore region in Southern Switzerland. These flows will be introduced in chapter 4.

Since the original Doppler velocity data are folded, as described in section 1.6, a dealiasing algorithm needs to be applied to the data before estimating the wind. We use the scheme developed by James and Houze (2001), which exploits not only the continuity of the radar measurements in space (three dimensions), but also in time (fourth dimension).

The wind estimation algorithm reads the unfolded data only in the regions selected for each flow, performing a quality control of the wind values. If the controls are successful, the intensity and direction of the mesoscale wind are estimated. The algorithm, is described in detail in this section.

Preparation of the Doppler products

At the beginning of the algorithm the radar Doppler velocities estimates corresponding to the different elevation angles of the radar beam are specified. Since the number of elevation angles to be considered depends on the flow to be estimated, an initial loop on the elevations for the considered flow prepares the data to be fitted through the following actions:

1. Making use of specific functions, the areas in which the data have to be considered are determined.

2. The file containing the unfolded data is read, and if the data are corrupted, that particular elevation is no more considered.

3. The Doppler velocity data are read only in the regions of interest.

4. The number of Doppler data for each elevation has to be larger than 10, in order to not consider isolated echoes, which probably are due to not-weather phenomena. The value of 10 is just a reasonable preliminary threshold on the number of data, since the following criteria are even more restrictive.

5. The radial wind values are corrected for the elevation of the radar beam, in order to get only the horizontal component of the wind. To this aim, the radial wind value is multiplied by the cosine of the elevation angle.

At the end of this loop on the elevations, a matrix containing the azimuth and the radial velocity value for all the needed elevations is obtained. Before the regression starts, the following quality controls are performed on the data:

1. The number of Doppler data for all the considered elevations has to be larger than 60, in order to do the regression with a significant amount of data.

2. The number of 1-degree rays that contain velocity data has to be larger than 60. Also this control is done in order to not consider isolated patches of data.

3. The azimuthal arc covered by the data has to be at least of 80 degrees. The goal of this control is to take into account only data which are spread on a reasonable azimuthal arc, and then which enable a successfull regression.

If these three criteria are not satisfied, the program does not move to the regression. The threshold values have been chosen looking at the wind estimates of 6 events of heavy precipitation, corresponding to about 100 hours of precipitation, for 10 different flows (regions).

Linear regression

If the wind in the selected region is $\vec{V} = (u, v)$, the algorithm has to estimate the regression coefficients u and v such that:

$$V_r(\alpha) = u\cos(\alpha) + v\sin(\alpha) \tag{1.42}$$

where $V_r(\alpha)$ is the dealiased radial wind measured by the radar at an azimuthal angle α.

The normal equations, which minimize the sum of the square differences between the left and right sides, are resolved by means of Singular Value Decomposition (e.g. Press et al., 1992). Singular Value Decomposition (SVD) is based on the following theorem of linear algebra: any $M \times N$ matrix A whose number of rows M is greater than or equal to its number of columns N, can be written as the product of an $M \times N$ column-orthogonal matrix U, an $N \times N$ diagonal matrix W with positive or zero elements (the singular values), and the transpose of an $N \times N$ orthogonal matrix V:

$$[A] = [U] \cdot [W] \cdot [V^T] \tag{1.43}$$

where

$$[W] = \begin{bmatrix} w_1 & & & \\ & w_2 & & \\ & & ... & \\ & & & w_N \end{bmatrix} \tag{1.44}$$

The matrices U and V are each orthogonal, i.e. $U^T \cdot U = V^T \cdot V = 1$.

If the matrix A is square, $N \times N$, then U, V, and W are all square matrices of the same size. Since U and V are orthogonal, their inverses are equal to their transposes; as W is diagonal, its inverse is the diagonal matrix whose elements are the reciprocals of the elements w_j. From equation 1.43 it follows that the inverse of A is:

$$[A^{-1}] = [V] \cdot [diag(1/w_j)] \cdot [U^T] \tag{1.45}$$

if one or more of the w_j's is zero or too small so that its value is dominated by roundoff error and therefore unknowable, the matrix is even more singular. The ratio of the largest of the w_j's to the smallest of the w_j's is called the condition number of a matrix. A matrix is singular if its condition number is infinte, and it is ill-conditioned if its condition number is too large, i.e. if its reciprocal approaches the machine's floating point precision.

Following Press et al. (1992), the expression:

$$[A] \cdot \vec{x} = \vec{b} \tag{1.46}$$

19

where A is a square matrix, x and b are vectors, defines A as a linear mapping from the vector space x to the vector space b. If A is singular, then there is some subspace of x that is mapped to zero, i.e. $A \cdot x = 0$; such subspace is called the nullspace. There is also some subspace of b that can be reached by A, i.e. that there exists some x which is mapped there. This subspace is called the range of A. The dimension of the range is called the rank of A. If A is nonsingular, then its rank is N. If A is singular, then the rank will be less than N.

SVD explicitly constructs orthonormal bases for the nullspace and range of a matrix. Specifically, the columns of U whose same-numbered elements w_j are nonzero are an orthonormal set of basis vectors that span the range; the columns of V whose same numbered elements w_j are zero are an orthonormal basis for the nullspace. If A is singular, the set of homogeneous equations given by 1.46, if $b = 0$ is solved immediately by SVD: any column of V whose corresponding w_j is zero yelds a solution. When the vector b on the right-hand side is not zero, if it lies in the range of A then the singular set of equations have a solution x; in fact it has more than one solution, since any vector in the nullspace can be added to x in any linear combination. If one wants to find one particular member of this solution-set of vectors as a representative, the one with the smallest length $|x|^2$ can be taken, replacing $1/w_j$ by zero if $w_j = 0$ and computing (working from right to left):

$$\vec{x} = [V] \cdot [diag(1/w_j)] \cdot ([U^T] \cdot \vec{b}) \tag{1.47}$$

This is the solution vector of smallest length; the columns of V that are in the nullspace complete the specification of the solution set.

Once the coefficients u and v of equation 1.42 are thus solved, the sinusoidal function which is the best fit of the wind can be found.

After-regression controls

Even though the dealiased data which are fitted to a sine satisfy the previous controls, the regression may still lead to a wind estimate which does not represent the real wind in the whole region in which the data are taken, due to the following different reasons:

1. Despite their good localization in space, the velocity values may be erroneous, due to a wrong performance of the dealiasing scheme.

2. The presence of a small number of outliers strongly influences the regression, which then does not represent the real wind.

3. A small variability of the velocity values along the azimuthal arc does not allow a good performance of the regression, which consequently may be ambiguous.

4. The presence of small-scale features in the wind field in the region of interest may lead to a fitted sine which does not represent the real flow. It is questionable whether the flow in the regions of interest may be considered as linear. Since we are interested in the general mesoscale wind, then to a certain degree the approximation of the linear wind is accepted (in reality the flow is more complex than idealized conceptual model - e.g. shearing, streakes, small maxima, etc.).

In order to consider these possible sources of bad wind estimate, four scores which evaluate the performance of the linear regression are calculated. The wind estimate is then taken into account or rejected depending on the values of the scores. If the wind estimate is considered as valid, an index of quality (PT) which takes into account the value of the four scores is assigned to each estimate. The value of this index ranges from 9 to 20, and if it is smaller than 16 the wind estimate is considered to be of low quality. To calculate the value of PT, a number ranging from 2 (worst quality) to 5 (best quality) is assigned to each parameter depending on its value. Then the sum of the 4 values represents

PT. The large number of threshold values has been chosen looking at the large data set of 6 events of heavy rain (about 100 hours of rain). The threshold values depend on the considered flow, since the geographical extension of the flows is different in both horizontal and vertical dimensions (the flows will be introduced in chapter 4). In particular, the criteria to be satisfied by the data for the Low Level Flow, Mid Level Flow and Cross Barrier Flow are less restrictive than that for Upper Level Flow, since the latter has a larger extension and it is spread over the whole azimuthal circumference, making easier the wind estimate. Moreover, since the Cross Barrier Flow, the Mid Level Flow and the Low Level Flow are closer to the ground than the Upper Level Flow, they may show a bigger variability due to frictional effects which cause small scale features, making more difficult the wind estimation. The four scores are:

1. Normalized Root Mean Square Error. It is the root mean square error between each measured velocity value and the fitted velocity value at the same azimuth, divided by the amplitude of the sine. Thus this parameter takes into account the distribution of the data around the fitted sine, i.e. their average distance from the curve relative to its amplitude. The best fits have values approaching 0, whereas larger values indicate a bad wind estimate.

2. Correlation Coefficient. It is the correlation coefficient between each measured velocity value and the fitted velocity value at the same azimuth. It represents the general quality of the fitting, since it considers how well the data fit to the found sinusoidal curve. The best fits have values approaching 1, the worst values up to -1.

3. Normalized 90 Percentile. It is the 90 percentile of the distance between the measured velocity values and the fitted sine, divided by the amplitude of the sine. Also this parameter takes into account the spread of the data around the fitted sine, relative to the amplitude of the curve.

4. Ratio of Singular Values. It is the ratio of the singular values which are obtained from the Singular Value Decomposition, and it describes the variability of the data along the azimuthal direction. Values close to 1 indicate that the data points are quite uniformly spread over the range of azimuths, whereas values close to 0 correspond to bad azimuthal distribution of the data points.

Second regression

If the velocity data satisfy all the previous controls, a second linear regression is performed, taking into account only the Doppler data whose distance from the fitted sine is less than the 90 percentile of the distance between the measured velocity values and the sine fitted through the first regression. Therefore, this second regression tends to not be influenced by the presence of outliers. The controls that were made before the first regression, and already illustrated, are performed again before proceeding with the second regression. The amplitude and the phase of the fitted sine which result from this second regression represent the best estimate of the wind in the region of interest.

Chapter 2

The relation between airflow and orographic precipitation on the Southern Side of the Alps as revealed by weather radar

Abstract

The relative importance of various environmental parameters in determining orographic precipitation patterns in the Lago Maggiore region in the southern part of the European Alps is investigated. Fifty-eight long-lasting and widespread orographic precipitation events corresponding in total to 106 days of rainfall are examined. The mesoscale winds are estimated by means of Doppler velocity radar measurements; air mass stability is computed from both radiosoundings and pairs of ground stations located at different heights. High-quality radar-derived rain rates at the ground are used to characterize the precipitation field.

The mesoscale flows are estimated within the layers whose mean wind velocity correlates best with rainfall in the mountains, which are located around 1 km asl upstream of the Alps and around 3 km above the first alpine peaks. Upstream wind velocity has the largest impact on the intensity and frequency of precipitation in the mountains, while the direction of the wind determines the spatial distribution of precipitation. Unstable conditions cause more precipitation over the mountains as compared to stable cases; however, differences in air mass stability have a minor impact on the precipitation intensity as compared to wind speed and direction. The intensity of the flow dominates rainfall patterns also in different Froude number airflows.

This study builds the scientific framework necessary to develop an heuristic system for nowcasting orographic precipitation in the Alpine region by exploiting the presence of the orographic forcing. The latter is shown to give repeatability to the rainfall patterns typically observed in the region with particular environmental conditions.

2.1 Introduction

There is an increasing interest in the operational meteorological and hydrological services in specific short-term predictions of the intensity, location, onset and termination of orographic rainfall. Numerical models are the main source of information in long-range forecasting widespread and long-lasting orographic precipitation. However, they have difficulties in predicting the exact timing, intensity and location of the rain; moreover, the time needed to produce the forecast is often too long with respect

to the demands of the forecasters and end-users. For these reasons numerical models are used together with a number of observational systems if short-range forecasting (0-6 hours) is required. In this context, nowcasting tools assume a particular relevance in the last stage of the weather forecasting process, as highlighted by the hydrometeorological forecast demonstration project MAP D-PHASE (Rotach and co authors, 2009).

The goal of this study, which is part of COST-731 (see *http://cost731.bafg.de*), is to build the scientific framework over which a tool for nowcasting orographic precipitation associated with baroclinic systems approaching a mountain chain can be developed. To this end, an observational sensitivity study aimed to find the environmental parameters which regulate the intensity and the distribution of the orographic precipitation is performed. The focus of the analysis is the Lago Maggiore region, which is located in the southern part of the European Alps between Italy and Switzerland (figure 3.1). In the Lago Maggiore region, which is notorious for heavy rainfall and floods, some of the highest amounts of rain in the Alps are registered during the autumn season (Frei and Schar, 1998); moreover, this region was chosen as one of the target zones of the Mesoscale Alpine Programme (MAP). During the MAP Special Observing Period (September-November 1999) a large number of observational instruments collected a considerable amount of meteorological data in the region (Bougeault et al., 2001). Thus several studies investigated the synoptic, mesoscale and microphysical processes leading to orographic precipitation in the area; an organic review of these studies is given by Rotunno and Houze (2007).

By considering all precipitation events during autumn 1998 and 1999, Houze et al. (2001) found a clear relation between the upstream flow direction, velocity and air mass stability and the intensity of precipitation. In the Lago Maggiore region most of the rain was observed when the flow at 2 km was strong and southerly or south-easterly, i.e. when it was almost perpendicular to the alpine barrier. Houze et al. (2001) also proved that the spatial distribution of precipitation depended on whether the upstream flow was blocked or unblocked. In the unblocked cases (high Froude number), a great enhancement of precipitation was observed over the lower windward alpine slopes; in the blocked cases (low Froude number), precipitation was enhanced also upstream of the barrier. Similar findings were also obtained by Neiman et al. (2002) and James and Houze (2005), who studied orographic precipitation enhancement mechanisms over California's coastal mountains. A conceptual model for the orographic precipitation mechanisms in stable blocked and unstable unblocked flows was proposed by Medina and Houze (2003). This conceptual model highlights the leading role of the upstream mesoscale flow kinematic and thermodynamic characteristics in originating different precipitation regimes over the mountains and the nearby areas. The relative importance of different mesoscale factors in producing orographic precipitation was also investigated by Yuter et al. (2011) in the Portland region (Oregon). They found that the upstream wind speed and freezing level height have the largest impact on the intensity and duration of precipitation in the mountains. Wind direction derived from numerical models is also operationally used in some areas of North-West USA to determine the spatial distribution of rainfall over the mountains (Rhea, 1996; Schaake et al., 2004). The water vapour content is another fundamental element of orographic precipitation mechanisms (e.g. Browning et al., 1974; Alpert, 1986; Ralph et al., 2004, 2005; Neiman et al., 2009). However, its role in regulating the intensity of rainfall is not explored in this study, since Neiman et al. (2009) showed that most of variations in rainfall rates in the mountains can be explained, in first approximation, to variations in the upslope flow velocity.

This paper investigates the dependence of orographic precipitation on mesoscale winds and air mass stability in the Lago Maggiore region. The data set consists of 58 orographic precipitation events observed from 2004 to 2008, corresponding in total to 106 days of rainfall. The paper is both an original contribution to orographic precipitation science and an interesting basis for the development of nowcasting techniques. Its strength lies in the following aspects:

1. The precipitation field is characterised by a quality controlled radar map of surface precipitation based on sophisticated data processing specifically developed for a mountainous region.

2. The wind is characterised by Doppler radar estimates of the mean mesoscale flow averaged over pre-defined significant regions.

3. Atmospheric stability is calculated both from radiosoundings and pairs of adjacent ground stations located at different heights.

4. All data are also available in real-time and can thus be used in a later step for the development of a nowcasting system.

In Sect.2.2 of the paper, the data and methods used in this study are described in detail. Sect.2.3 is a preliminary investigation of the main kinematic and thermodynamic characteristics of the atmosphere upstream and within the Lago Maggiore region during the selected precipitation events. In Sect.2.4 the layers whose mean wind velocity correlates better than others to the mean rainfall measured in the Lago Maggiore region are searched. A rationale for the choice of the mesoscale flows, which are estimated in these significant layers, is given in Sect.2.5. In Sect.2.6 the relation between airflow, air mass stability and orographic precipitation is investigated by means of statistical methods: maps of frequencies of rain rate exceeding particular thresholds corresponding to some specific ranges of atmospheric dynamic and thermodynamic parameters are presented; this section represents a 5-years climatology of orographic precipitation events in the Lago Maggiore area. The main findings of this study are reported and discussed in Sect.3.5.

2.2 Data and methods

2.2.1 Radar data

The primary source of data for this study is the MeteoSwiss weather radar located on the top of Monte Lema (figure 3.1), one of the southern-most mountains of the Alpine ridge in the Lago Maggiore region (figure 3.1). Radar data were used to estimate rainfall at the ground and mesoscale winds in selected areas of the volume scanned by the radar. The time period considered in the analysis ranges from January 2004 to December 2008. Information on rainfall is obtained by the operational radar product for quantitative precipitation estimation, which is the result of sophisticated data processing based on 40 years of experience in radar operation in the Alpine environment at MeteoSwiss (Joss and Lee, 1995). Such product represents the best estimate of precipitation at the ground, and it is retrieved through a weighted mean of all the radar observations aloft. To account for growth and phase change of hydrometeors between the heights of a radar measurement and the ground, an average vertical profile of radar reflectivity observed within 70 km from the radar is used (Germann and Joss, 2002). The horizontal spatial resolution of the precipitation map is 1km x 1km, the temporal resolution is 5 minutes. A preliminary large-sample evaluation has been performed by Gabella et al. (2005) by analysing two years of radar and gauge data. The results of this and other studies (e.g. Germann and Joss, 2004) have been used to further improve the algorithm in recent years. A comprehensive description of the radar data processing implemented at MeteoSwiss has been presented by Germann et al. (2006). In brief, radar data processing includes automatic hardware calibration, ground clutter elimination, visibility correction, correction for vertical profile of reflectivity, removal of residual non-weather echoes and bias correction. The latter compensates for systematic errors due to non-uniform beam filling, low-level growth not seen by the vertical profile correction and attenuation. An objective verification of the radar performances for individual regions of the Swiss Alps is also presented in Germann et al. (2006). Since the last major change in radar algorithms was made in 2003, skill scores presented in Sect.5 and figure 8 of Germann et al. (2006) represent the quality of the precipitation estimates which are part of the data set of this study. The largest portion of the Lago Maggiore area is part of the region labeled 'S Ticino', whereas the northern-most band of the study area belongs to the region 'Alps Ticino'. After local bias correction residual biases are small.
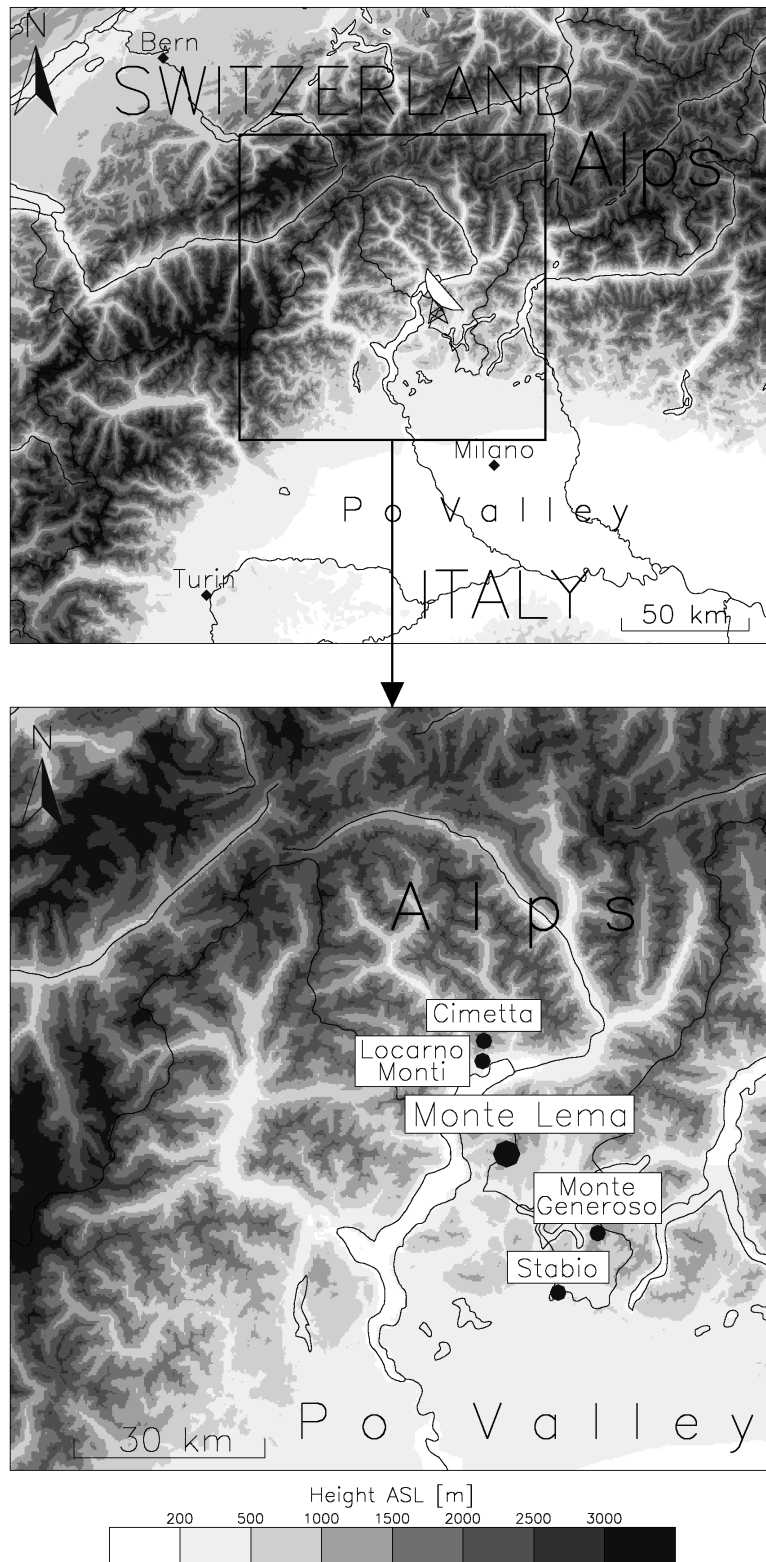
Figure 2.1: *Top: Orographic map of the Central Alps between Italy and Switzerland. The location of MeteoSwiss Monte Lema radar is indicated by the radar symbol. Bottom: Zoom into the Lago Maggiore region, with the location of the radar and of the ground stations considered in this study: Locarno Monti (LOM, 383 m), Cimetta (CIM, 1672 m), Stabio (SBO, 353 m), Monte Generoso (GEN, 1608 m). The spatial domain of the bottom panel is also used in the following figures, which show the results of the precipitation frequency analysis (120x120 km).*

In 'S Ticino' only 3% of the rainy days are totally missed by the radar, which corresponds to 0.2% of the total rainfall amount, see discussion of figure 10 in Germann et al. (2006). In 'Alps Ticino' the percentage of missed rainy days is larger, i.e. 20%. This, however, accounts to no more than 4% of total rainfall amounts. This suggests that in the Lago Maggiore region radar quantitative precipitation estimation misses only very weak events, which are not the focus of this study.

The mesoscale wind is estimated by Doppler velocity measurements, which are taken over 20 elevation angles and are updated every 5 minutes with a spatial resolution of 1 degree in azimuth and 1 km in range (Joss et al., 1998). Vertical profiles of the mean wind field above the radar station, derived from the two highest radar beam measurements, are also used in this study (Germann, 1998).

2.2.2 Selection of cases

Long lasting and widespread precipitation events are investigated in this study. In the Lago Maggiore region they are typically caused by a large-scale supply of moisture towards the Alps, which is forced to ascent over the alpine southerly slopes. Precipitation due to isolated convection and air-mass thunderstorms, on the other hand, is less extended in space and time, and it is triggered not only by the large-scale orographic forcing but also by other smaller-scale mechanisms as, for example, diurnal local circulations. In order to find an objective method able to identify long lasting and widespread rainfall and to exclude isolated thunderstorms, the 2006 operational radar product for quantitative precipitation estimate was taken into account. Radar data have been used instead of rain-gauges measurements because the need to detect long-lasting and widespread precipitation was more important than the requirement to have precise punctual rain estimates. In fact, radar precipitation estimates have higher spatial resolution with respect to rain-gauges, and this is particularly important in mountainous regions where precipitation varies greatly from one place to the other.
In 2006 there were 103 days in which at least 0.63 mm/h of rain have been detected by the radar in at least 1000 km^2 within the Lago Maggiore region (which comprises ~8000 km^2); the time periods with missing data in that year corresponded to 9.4 days (data gaps occurred because of preventive maintenance and failures of power supply, telecommunication and radar system). Various rain rate threshold values were applied to this data set in order to isolate long lasting and widespread rainfall. Depending on the threshold values used, a number of rain events of different severity was found. A simple statistical analysis of the radar-derived rain rates of these events permitted to identify the criterion which better than the others both filters out thunderstorms and preserves intense phases of orographic precipitation potentially dangerous for humans and infrastructures. The criterion that turned out to be most suitable for this purpose is the following: the rain rate within the Lago Maggiore region has to exceed 4 mm/h in at least 1000 km^2 for at least 2 hours, and in at least 2000 km^2 for at least 1 hour. Grid points affected by heavy rain not necessarily have to be contiguous. Once an event was identified, its duration was defined as the time period in which the rain rate exceeded 0.63 mm/h over an area of at least 100 km^2. By using this criterion, 58 events were found in the 5-years period from January 2004 to December 2008, corresponding in total to 106 days of precipitation (2547 hours). 19 events were observed in summer (June to August), 2 in winter (December to February), 20 in Spring (March to May) and 17 in Autumn (September to November). The distribution of hours of rainfall per month is shown in figure 2.2. As it is seen in the figure, spring and autumn are the seasons in which most of the hours of rainfall were observed.

2.2.3 Automatic stations and sounding data

To characterize the atmospheric conditions upstream and within the Lago Maggiore region, this study makes use of radiosoundings and ground stations data.
Radiosoundings data stem from the Milano Linate operational site, which is located about 50 km

south-east of the Lago Maggiore area (see figure 3.1) and it is managed by the National Centre for Aeronautical Meteorology and Climatology of Italy. The observational frequency was four per day up to February 2006 (00,06,12 and 18 UTC), two per day from February 2006 to February 2008, (00,12 UTC), and three per day after that (00,06,12 UTC). A total of 286 soundings were launched during the selected precipitation events and are considered in this study. Each value derived from radiosoundings was considered representative for the period ranging from two hours before to two hours after the time of launch; a single sounding was thus associated to no more than four hours of precipitation.

Ground stations data are derived from the MeteoSwiss automatic stations network, consisting of 115 automated meteorological stations all over Switzerland which measure the main meteorological parameters every 10 minutes. Two pairs of adjacent stations were used to estimate the stability of the lower atmosphere within the Lago Maggiore area: Locarno Monti (383 m) and Cimetta (1672 m), which are located at the northern edge of Maggiore Lake, Stabio (353 m) and Monte Generoso (1608 m), placed on the first slopes of the Alps very close to the Po Valley (see figure 3.1). These stations are located at different altitudes, thus permitting to have an estimate of the mean stability of the layer between the two stations.

2.2.4   Wind estimation from radar

In order to estimate the mesoscale winds in the Lago Maggiore region, radar Doppler measurements are used in this study. To obtain the radial velocity of a target, Doppler weather radars determine the Doppler frequency of the backscattered signal. If the pulse repetition frequency of the radar is too low to resolve the phase shift that occurs between successive pulses reflected by moving precipitation particles, aliasing occurs. In this case the apparent phase shift detected by the radar differs from the true one by plus or minus some integer multiple of 2π. Therefore Doppler radar measurements need to be dealiased before the wind can be estimated. The four-dimensional Doppler dealiasing scheme developed by James and Houze (2001) is employed. This algorithm exploits not only the continuity of the radar measurements in space (three dimensions), but also in time (fourth dimension). After the dealiasing process, the intensity and direction of the flows are estimated by fitting a linear wind to all valid Doppler measurements within pre-defined regions. Fitting is done by multiple regression using normal equations and Singular Value Decomposition (Press et al., 1992). A number of automated quality controls is performed before and after the fitting in order to reject the data which lead to wrong flow estimates and to detect the low quality flow estimates.

The performance of this wind estimation technique is good if there is a sufficient number of echoes
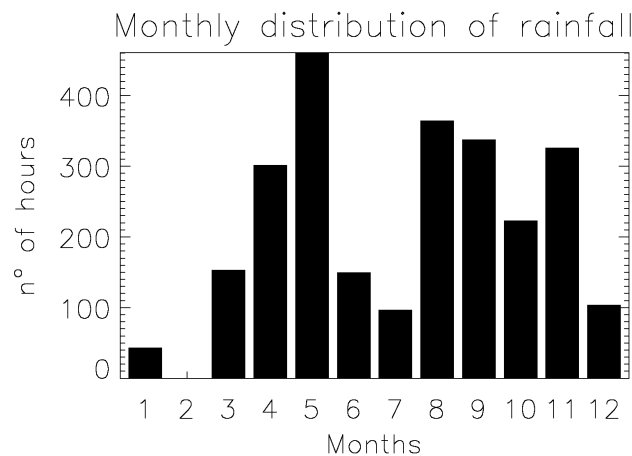
Figure 2.2: *Distribution per month of the 2547 hours of orographic precipitation relative to the 58 events considered in this study.*

and if the wind field within the region of interest is approximately linear. These flow estimates are more reliable than ground station measurements because they are not affected by very local winds due to the obstacles located in proximity of the anemometer. Moreover, the mesoscale flow can be estimated at different heights and in each part of the volume scanned by the radar. The resulting wind vector is representative of the wind present in the region in which the Doppler measurements are taken; an higher resolution wind field is not required for the scope of this study.

2.2.5 Statistical analyses

The general relation between different flow regimes and orographic precipitation in the Lago Maggiore region is investigated by means of statistical analyses. Two main methods were used: precipitation frequency and mean rain rates analyses. Both select from the 106-days data set rainfall rates corresponding to particular environmental conditions. Then statistical quantities are calculated at each grid point: percentage frequencies of rain rate exceeding specific thresholds and mean rain rates. Figures are only shown for the precipitation frequency method (except figure 2.7). The text, however, discusses both results for the frequency and the mean rain rates analysis. Figure 2.3 illustrates how the precipitation frequency method is performed. In the example of the figure, the parameter used to stratify the radar images is the intensity of the Low Level Flow (LLF, which will be introduced in Sect.2.5). Wind estimates from short parts of two distinct events of orographic rain are considered (for simplicity a data set consisting of only 14 5-minutes time steps is used). Radar precipitation images corresponding to the times in which LLF velocities are within the required interval are taken into account; percentage frequencies of rain rate exceeding a threshold value of 1 mm/h are calculated at each grid point of the image, and shown for the entire domain.
The objective of this investigation is first to understand how mesoscale flows and air mass stability affect the character of orographic precipitation, and second to demonstrate whether or not any nowcasting tool based on the behaviour of such parameters would improve operational nowcasting of rain. A large number of rain rate maps are considered in the analysis, thus reducing the stochastic part of the uncertainties in radar rainfall estimates. The remaining uncertainty is not critical in this context, as the focus here is not on the absolute values of rainfall frequencies or mean rain rates, but rather on their variability in space and time.

2.3 General mesoscale features during orographic rainfall

A preliminary investigation of the main kinematic and thermodynamic characteristics of the atmosphere is performed in this section, in order to give a general overview of the main mesoscale features upstream of the Alps and within the Lago Maggiore region during orographic rainfall.

2.3.1 Vertical profiles of wind from Milan radiosoundings and from radar

Figure 2.4 shows the mean wind intensity and direction measured by the radar above the radar site and by Milano radiosoundings during the selected precipitation events. Radar wind measurements are derived by the two highest sweeps, and thus they represent the vertical profile of the wind above the radar site (see Sect.3.3.1). Also radiosoundings measurements can be considered as a vertical profile of the wind, since the balloon covers just a few kilometers in the horizontal direction while ascending the first kilometers of the atmosphere. Only radar-derived wind averaged over the hour following the launch of the radiosondes was considered, thus permitting the comparison of this profile with the radiosoundings data. As clearly shown by the radiosoundings profile (thick barbs), in the low levels there is a veering with height of the wind, which indicates warm advection. This change from easterly to southerly winds with height at low levels is typically observed during heavy orographic precipitation (Kappenberger and Kerkmann, 1997; Ferretti et al., 2000; Rotunno and Ferretti, 2001;
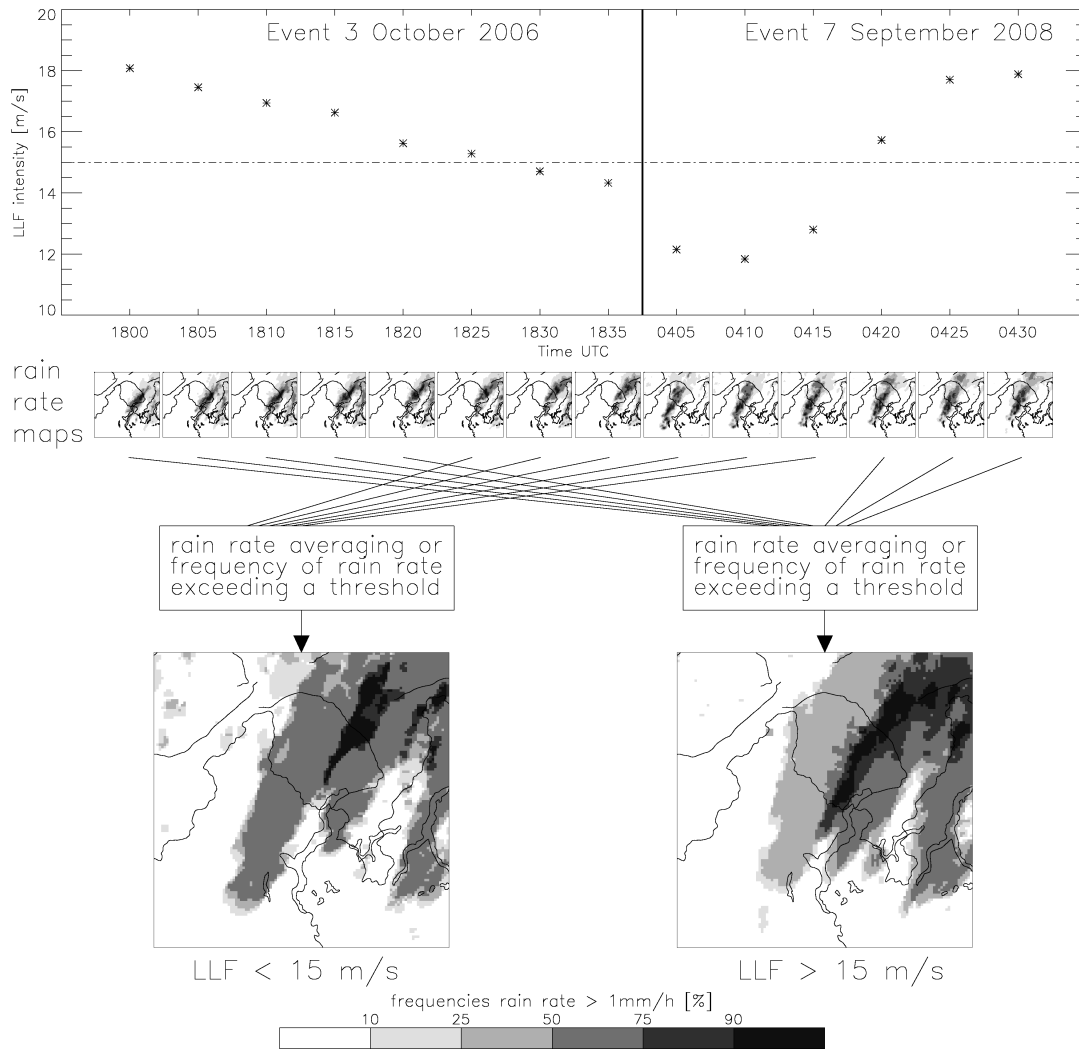
Figure 2.3: *Schematic illustration of the precipitation frequency analysis. In this example the parameter used to stratify radar images is the Low Level Flow (LLF) intensity; the threshold value is 15 m/s. Wind estimates from short parts of two distinct events of orographic rain are considered. Radar precipitation images corresponding to the times in which LLF velocities were within the required interval are taken into account; the percentage frequencies of rain rate exceeding a threshold value are calculated at each grid point of the image, and shown for the whole spatial domain. In the case of mean rain rates analysis, which was also performed in this study, rain rates are averaged at each grid point in order to produce a mean precipitation field.*

Ralph et al., 2005) and it is associated with an upper level trough which, approaching the Alps from the West, provides the moist large scale flow responsible for the heavy rain (Grazzini, 2007). The radiosounding profile of figure 2.4 does not show the presence of a strong low-level jet, although this is an element which is commonly observed when extratropical cyclones impinge upon mountain chains (e.g. Browning et al., 1975; Neiman et al., 2002; Ralph et al., 2005). The reason for this might be that figure 2.4 shows a mean profile which includes different stages of the precipitation events and not only the most intense phases of orographic precipitation, in which the low-level jet is more likely to be present (Neiman et al., 2002). The vertical profile of the wind above the radar site is given by the thin barbs in figure 2.4. This wind appears to be slightly stronger respect to the wind which is measured by radiosoundings over the Po Valley up to about 5.5 km, smaller at higher altitudes. Moreover, it is more easterly at all the altitudes. The differences in wind direction, resulting from the different geographical location of the measurement sites, are probably caused by two effects acting

at the same time. First, the deflection of the southerly flow by the Alps, which cause a wind more parallel to the ridge (particularly marked below the height of the crest over the first Alpine peaks). Second, the winds associated with the low pressure system are different at the two sites: moving from Milano (radiosoundings profile) towards Monte Lema (radar profile) at constant height the wind tends to rotate counterclockwise because of the cyclonic circulation.
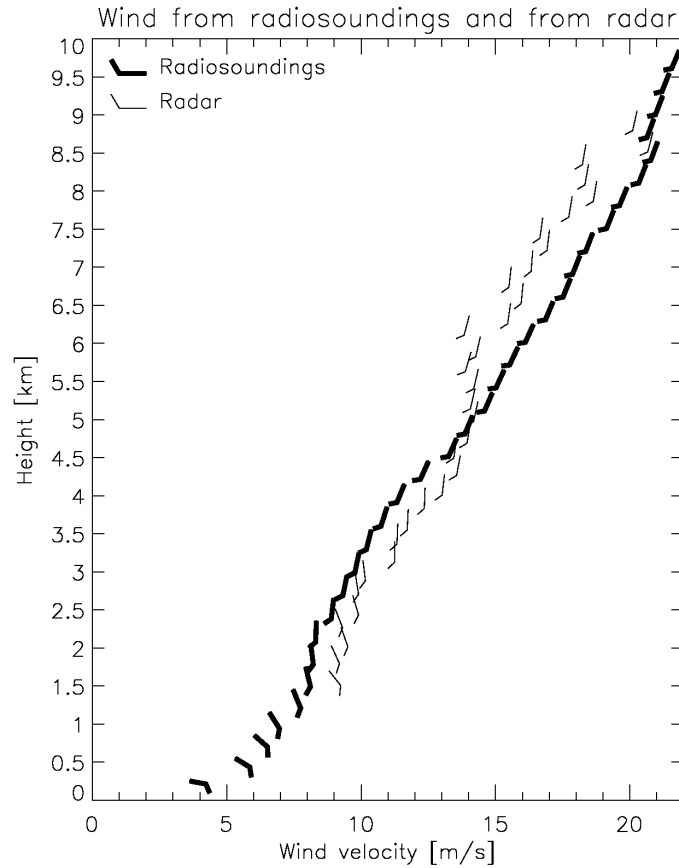
Figure 2.4: *Vertical profile of mean wind measured by the Milano radiosoundings (thick barbs) and from radar above Monte Lema (thin barbs) during the 106 days of rainfall. Wind barbs are indicative only of the direction of the wind; their x-coordinate gives the intensity of the wind vector. Radar-derived wind is averaged over the hour corresponding to the launch of the radiosondes; radar measurements start at 1.7 km asl.*

2.3.2 Composite of Milan radiosoundings

Thermodynamic profiles measured by the 286 radiosoundings (see Sec.2.2.3) were averaged over 100m-deep layers to produce a composite sounding representative of typical conditions upstream of the Alps during orographic precipitation. The resulting skew T-log$p$ diagram, shown in figure 2.5, depicts a nearly saturated low atmosphere. Neutral stratification with respect to moist ascent is a feature commonly observed in orographic precipitation events (Ralph et al., 2005; James and Houze, 2005; Yuter et al., 2011). Following an approach similar to that of Ralph et al. (2005), the profile of figure 2.5 served to justify the use of the moist instead of the dry static stability of the low atmosphere, which is a basic element of this study. For the profile of figure 2.5, the mean vertical displacement required to reach saturation in the first 2 km of the atmosphere is 410 m. This value is much smaller than the scale height of the Alps in the Lago Maggiore area, assumed to be comprised between 1500 and 3000 m. Therefore, the air approaching the Alps in the first 2 km of the atmosphere is

considered to be orographically lifted to saturation for a vertical displacement which is much smaller than the height range. Nearly saturated conditions of the low levels are also proved by the mode of the distribution of the Lifting Condensation Level of Milan radiosoundings, which is located at 370 m asl. For these reasons the air is assumed to be saturated by the time it produces rainfall over the Alps, so that the stability of the lower atmosphere was calculated using the moist Brunt-Väisälä frequency, following equation (36) of Durran and Klemp (1982).

2.3.3   Stability distribution

Distributions of mean squared moist Brunt-Väisälä frequencies of various vertical layers derived from Milano radiosoundings were computed. The dispersion of these distributions tends to decrease with increasing altitude and vertical extension of the layer in which the data are averaged. Therefore, the distributions with the largest dispersions are the ones obtained by averaging radiosoundings data in the lowest atmospheric layers. Figure 2.6(a) shows the distribution of the squared moist Brunt-Väisälä frequencies averaged in the lowest kilometer of the troposphere. The bottom of this layer was taken to be 350 m asl, in order to exclude data measured in the proximity of the ground. As it is seen in figure 2.6(a), the range of values of moist static stability measured above the area of Milano during rainfall in the Lago Maggiore region is large, and it is centered around almost neutral values.
Figure 2.6(b), on the other hand, shows the squared moist Brunt-Väisälä frequencies distribution computed from Stabio (353 m) and Monte Generoso (1608 m) ground stations measurements, which are located within the Lago Maggiore area (see figure 3.1). Such distribution, as shown by figure 2.6(b), is centered around slightly unstable values. In order to compare the two different estimates of stability, the distribution of the static stability derived from radiosoundings averaged between 350 and 1600 m was also computed (not shown). This height interval corresponds to the layer extended from the altitude of Stabio to the one of Monte Generoso. Such distribution was found to be very similar to figure 2.6(a), denoting that lower atmospheric conditions within the Lago Maggiore region during rainfall tend to be more unstable than above the area of Milano. However, when interpreting the estimates from ground stations it has to be considered that these values can be affected by a number of surface effects as, for example, diurnal cycle of heating and cooling, friction, etc.

2.3.4   Total precipitation frequencies and mean rain rates

Figure 2.7 represents percentage frequencies of rain rate exceeding 1 mm/h (panel a) and mean rain rates (panel b) at the ground in the Lago Maggiore area considering all the 58 orographic precipitation events. As it is seen in the figure, rain frequencies and mean rainfall are significantly larger in the northern part of the Lago Maggiore region than over the southern part and the Po Valley. The two artificial lines seen in figure 2.7 approximately at 40 and 250 degrees are due to the beam shielding caused by obstacles in proximity of the radar site. These artefacts, which are seen also in the following figures, are thus to be ignored.

2.4   Correlation analysis

In this section, the dependence of rain rates in the mountains on the intensity of the upstream flow at different heights is investigated. The goal of this analysis is to find the layer whose mean wind velocity correlates best with the mean rainfall measured in the Lago Maggiore region. Such layer is searched both upstream of the Alps and over the first alpine peaks, in order to find the regions in which to estimate the mesoscale flows for the precipitation frequency analysis later presented. This work is based on the correlation coefficient analysis performed by Neiman et al. (2002), who investigated the relation between low-level upstream flow and windward precipitation in California's coastal mountains. Figure 2.8 presents vertical profiles of correlation coefficients between mean rain rates in the Lago
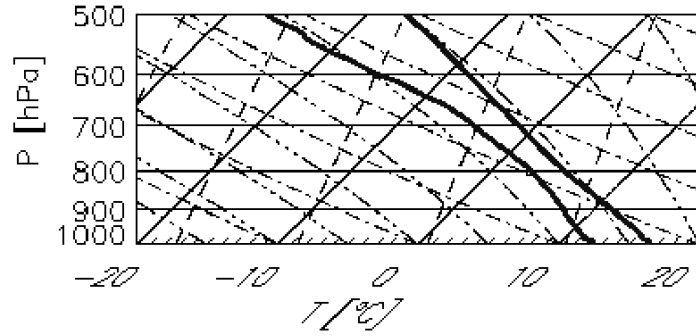
Figure 2.5: *Composite mean sounding (100m vertical resolution) on a skew T-logp diagram based on the 286 Milan radiosoundings launched during orographic rainfall in the Lago Maggiore region.*

Maggiore region and wind intensity measured by Milano radiosoundings averaged over 500m-deep layers, which are thin enough for the purposes of this work. Only the upslope component of the wind, which is the one perpendicular to the orientation of the barrier and thus the most favourable to the production of orographic rainfall, was considered. To determine this component, the Alps were assumed to be oriented from south-west to north-east in the Lago Maggiore region. Therefore, only
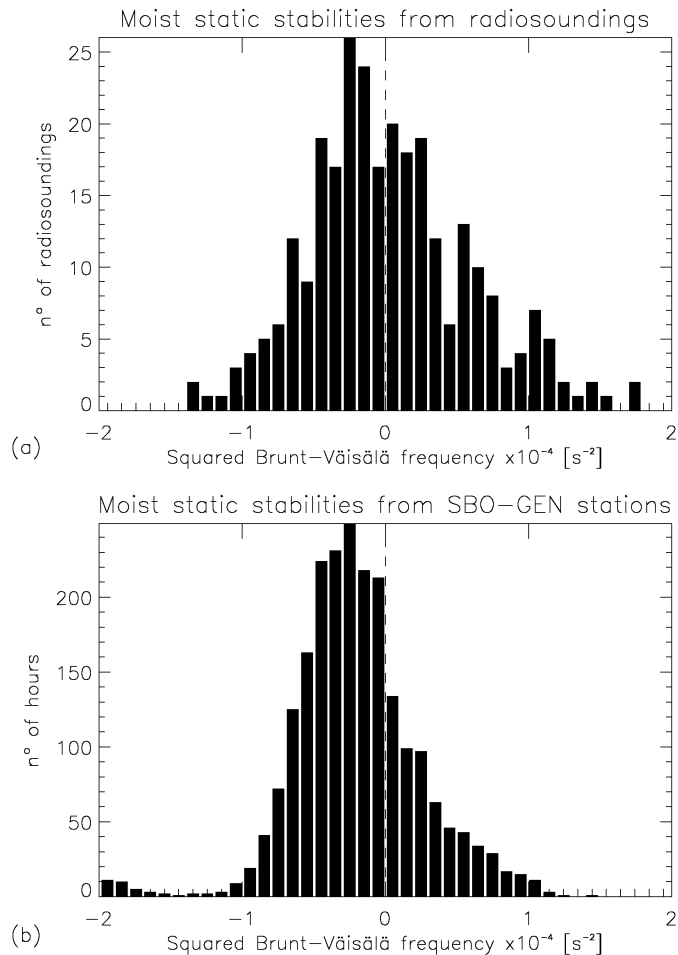
Figure 2.6: *Distribution of (a) squared mean moist Brunt-Väisälä frequency in the layer 350-1000 m derived from the 286 Milano radiosoundings launched during rainfall in the Lago Maggiore region and (b) squared moist Brunt-Väisälä frequency obtained from Stabio and Monte Generoso ground stations data (six measurements per hour, the total number of hours is 2369).*
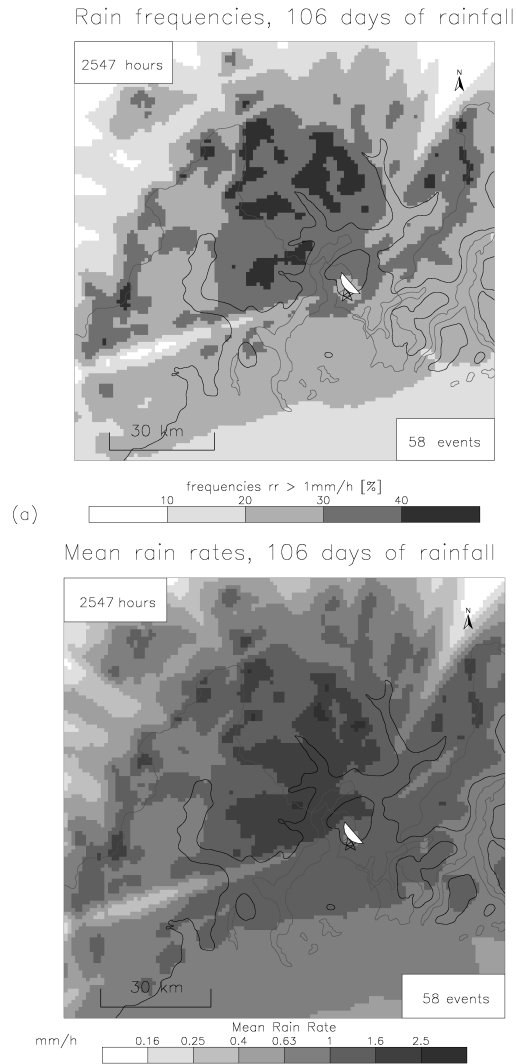
Figure 2.7: *Percentage frequencies of exceeding 1 mm/h of precipitation (a) and mean rain rates (b) at the ground in the Lago Maggiore region for the 58 events of orographic precipitation considered in this study. The location of Monte Lema radar is shown by the radar symbol. The total hours of precipitation and the number of precipitation events are indicated at the top left and at the bottom right corner of each panel respectively. The spatial domain of the boxes is 120x120 km. The black line denotes the 800 m asl terrain contour, while the grey line represent lakes and political borders.*

the component of the velocity vector along a line oriented from south-east to north-west (dotted line in figure 3.4(a)) was taken into account. Moreover, when this component of the wind was negative, denoting a downslope flow, the measurement was not included in the analysis. Rain rates are estimated by radar and averaged in the Lago Maggiore region over the hour following the launch of the sounding. As it is seen in figure 2.8, the values of correlation obtained by taking all the radiosoundings data involved in the precipitation events (thick line) increase in the lowest few hundred meters above the ground. They present a maximum between about 500 and 1500 m asl, after that they gradually decrease with height. Since also the atmospheric stability was proven to be an important factor in regulating rainfall in the mountains, as mentioned in Sect.3.1, radiosoundings data were stratified depending on the value of the mean squared moist Brunt-Väisälä frequency of the layer 350-1000 m. This layer was chosen because, as explained in Sect.2.3.3, its static stability distribution shows a larger dispersion than other layers, thus permitting to have a sufficient number of stable and unstable radiosoundings for a statistical analysis. Figure 2.8 shows that the vertical profile of the correlation

34

coefficients is strongly influenced by the stability of the lower atmosphere: stable conditions lead to values of correlation significantly smaller than in the other cases. Neutral and unstable soundings, on the other hand, exhibit large correlation coefficients with a maximum extending from about 1 to 1.5 km.

In order to investigate the relation between rain rates and the airflow measured at different heights over the mountains within the Lago Maggiore area, correlation coefficients analysis was extended considering radar-derived wind estimates above the radar site (see figure 2.9) instead of the wind measured by radiosoundings (presented in figure 2.8). Wind measurements were averaged over the hour following the launch of the radiosondes, thus permitting the comparison of the vertical profiles of figure 2.9 with that of figure 2.8. Also in this case radar-derived wind data were averaged over 500m-deep layers, and only the component of the velocity vector along a line orientated from south-east to north-west was considered. The stratification of the data based on the mean squared moist Brunt-Väisälä frequency of the layer 350-1000 m derived from radiosoundings was also performed. In general, the correlation coefficients between wind and rainfall shown in figure 2.9 are significantly larger than the ones of figure 2.8; however, in this case the maxima are less pronounced. Differences between stable, neutral and unstable radiosoundings appear also in figure 2.9: again, the smallest values of correlation are given by stable profiles, as in figure 2.8, whereas neutral and unstable ones correlate better than average. The vertical profile of correlation coefficients obtained by considering all the wind measurements (thick line in figure 2.9) presents a weak maximum between 2 and 4 km asl. As a last step of this investigation, vertical profile of correlation coefficients between mean rain rates in the Lago Maggiore region and radar-derived vertical velocities above the radar site was computed; also in this case, a maximum around 3 km asl is found (not shown).
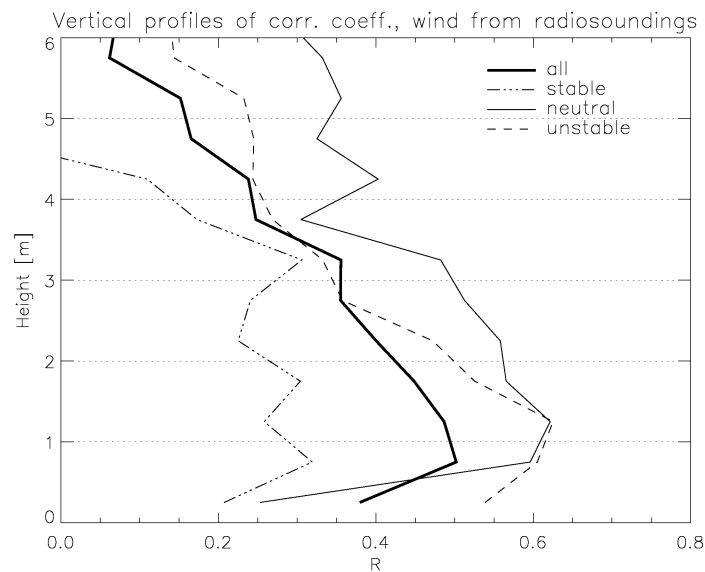
Figure 2.8: *Vertical profile of correlation coefficients between the upslope component of the wind (wind projected along a line orientated from south-east to north-west) measured by Milano radiosoundings and the radar-derived rain rate in the Lago Maggiore area during the selected precipitation events (286 soundings). Only positive upslope components of the wind were included in the analysis, and averaged over 500m-deep layers. The rain rate is averaged during the 60 minutes following the launch of the radiosonde over the whole Lago Maggiore area. Vertical profiles correspondent to all, stable, neutral and unstable soundings are presented. The mean squared moist Brunt-Väisälä frequency (N_m^2) of the layer 350-1000m was used to classify the soundings as stable ($N_m^2 > 0.2 \cdot 10^{-4} s^{-2}$, 101 soundings), neutral ($-0.2 \cdot 10^{-4} s^{-2} < N_m^2 < 0.2 \cdot 10^{-4} s^{-2}$, 79 soundings) and unstable ($N_m^2 < -0.2 \cdot 10^{-4} s^{-2}$, 106 soundings).*

Since rainfall intensity in the mountains is proportional to the moisture flux impinging upon the orographic barrier (e.g. Alpert, 1986), the lifting of the layers which present maxima in the vertical profiles of figure 2.8 and 2.9 can be considered as the most efficient in producing orographic rainfall. This analysis shows that the layers whose mean wind velocity correlates best with rainfall are located at an altitude of about 1 km upstream of the Alps, of about 3 km on the first alpine peaks.

A clear maximum in the correlation coefficients vertical profile was also found by Neiman et al. (2002), who considered winter-season events producing intense precipitation in California's coastal mountains. However, the observing system used for that study was somewhat different from the one of this study. In particular, they analysed data taken by wind profilers located in coastal sites and by rain gauges located in the mountains, the observing couplets being separated by 10-30 km. They found that the height of the maximum correlation is located near the top of the mountain (∼1 km asl). This study proved that far upstream of the Alps the height of the maximum is situated well below the height of the barrier (∼1 km asl), while it is found at an higher elevation above the first alpine peaks, about at the height of the top of the barrier (∼3 km asl). In the latter analysis, an observing methodology similar to that of Neiman et al. (2002) was used, at least the distance between wind and rainfall measurements was similar. Therefore, it appears that in proximity of the barrier the height of the orographic chain is indicative of the layer whose mean wind velocity correlates best with rainfall. Moreover, the differences in vertical profiles between unblocked and blocked flows found by Neiman et al. (2002) are similar to the differences between stable and unstable radiosoundings shown in figure 2.8 and 2.9. In particular, these differences are observed at the lower levels both in Neiman et al. (2002) and in this study, with blocked and stable cases presenting smaller correlation coefficients with respect to unblocked and unstable cases.

2.5   Rationale for the choice of the mesoscale flows

This section gives a motivation for the choice of the mesoscale winds estimated by means of radar Doppler measurements. The selection of mesoscale flows was driven by two main requirements. On the one hand, flows which have an important role in regulating the intensity of the orographic rainfall
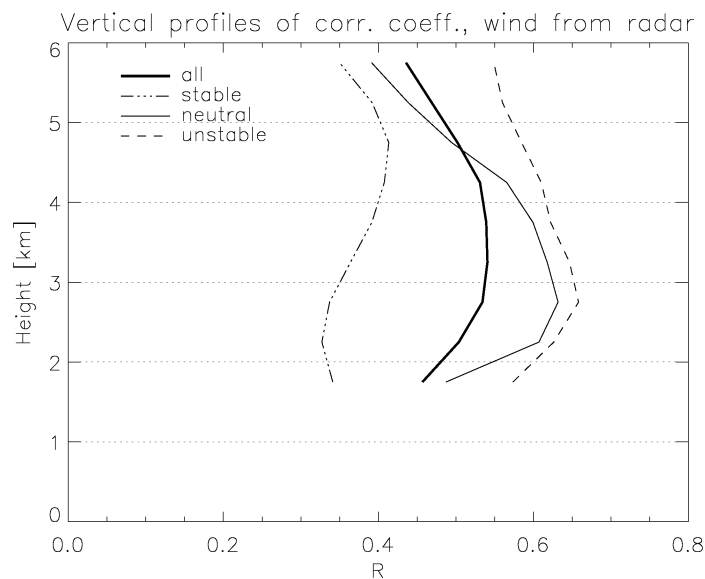
Figure 2.9: *As figure 2.8, but for the correlation coefficients between the upslope component of the wind measured by radar above the radar site and the radar-derived rain rate in the Lago Maggiore region during the selected precipitation events.*

in the Lago Maggiore area have to be estimated; on the other hand, the regions in which these flows are computed have to be visible from the radar and free from residual ground clutter. Thus their choice was made considering the results of Sect.2.3.1 and 2.4, and analyzing the main geographical features of the Lago Maggiore territory in relation to the location of Monte Lema radar and radar visibility. Four different flows are estimated; their vertical and horizontal extension is shown in figure 3.4.

1. Low Level Flow (*LLF*)
   Figure 2.8 clearly shows that the mean wind velocity perpendicular to the Alps of the lower atmospheric layers over the Po Valley is the most significant in regulating rainfall intensity in the Lago Maggiore area; the vertical extension of these layers depends on the thermodynamic conditions of the lower atmosphere. For these reasons the region in which to estimate the mesoscale flow upstream of the Alps was created at the lowest heights visible by the radar. Its shape is determined by radar visibility constraints. The Low Level Flow is thus estimated over the first alpine hills south-east of Maggiore Lake between 1.5 and 2 km asl.

2. Mid Level Flow (*MLF*)
   Figure 2.9 demonstrates that the mean wind velocity perpendicular to the Alps above the radar site between 2 and 4 km is the most significant in regulating rainfall intensity in the Lago Maggiore area. Thus a layer extending from 2.5 to 3.5 km was chosen to estimate the Mid Level Flow, which represents the wind ascending over the terrain above the Lago Maggiore region.

3. Cross Barrier Flow (*CBF*)
   This flow is retrieved south of the Alpine crest between 3 and 4 km asl in the north-westerly Lago Maggiore area. In this region, in fact, changes of wind due to the passage of cold fronts crossing the Alpine ridge are usually observed, indicating the let-up of heavy precipitation.

4. Upper Level Flow (*ULF*)
   Southerly winds are typically observed during heavy rainfall at the upper levels (see figure 2.4). In order to monitor these winds, associated with the upper level trough which provides the large-scale flux of moisture towards the Alps, the Upper Level Flow is estimated between 4 and 5 km in a wide ring around the radar site. Above this height, the radar echoes decrease significantly, thus not permitting to estimate the flow for long periods.

A number of regions similar to those shown in figure 3.4 were tested as possible areas in which to estimate the mesoscale flows. The regions in which the wind estimate was possible and of high quality for the longest time periods during the first 4 years of the data set (Jan. 2004 to Jan. 2008, 88 days of rain) have been chosen. The estimate of the LLF (MLF, CBF, ULF) was possible for 52 (60,50,61)% of the total time of rain (corresponding to 2547 hours).

2.6   Precipitation frequency analysis

This section illustrates the results of the precipitation frequency analysis. Percentage frequencies of rain rate exceeding 1 mm/h corresponding to particular environmental conditions are presented (see Sect.2.2.5). The parameters used to stratify the rain rates are given by the intensity and direction of the mesoscale flows (Sect.2.6.1), the moist static stability calculated by radiosoundings and ground stations data (Sect.2.6.2), both the mesoscale flows and the moist static stability (Sect.2.6.3).

2.6.1 Precipitation frequency analysis based on flows

Figure 2.11 shows the results of the precipitation frequency analysis for different mesoscale flows (see Sect.2.2.5 and figure 2.3). As opposed to figure 2.3, the whole data set of 106 days of rainfall is now used. In figure 2.11 percentage frequencies of rain rate exceeding 1 mm/h at the ground level corresponding to different classes of intensity and direction of LLF, MLF, CBF and ULF are presented. The classes corresponding to directions not represented in figure 2.11 are not populated, except the north-easterly; the latter is not shown because this flow does not present an upslope component in the
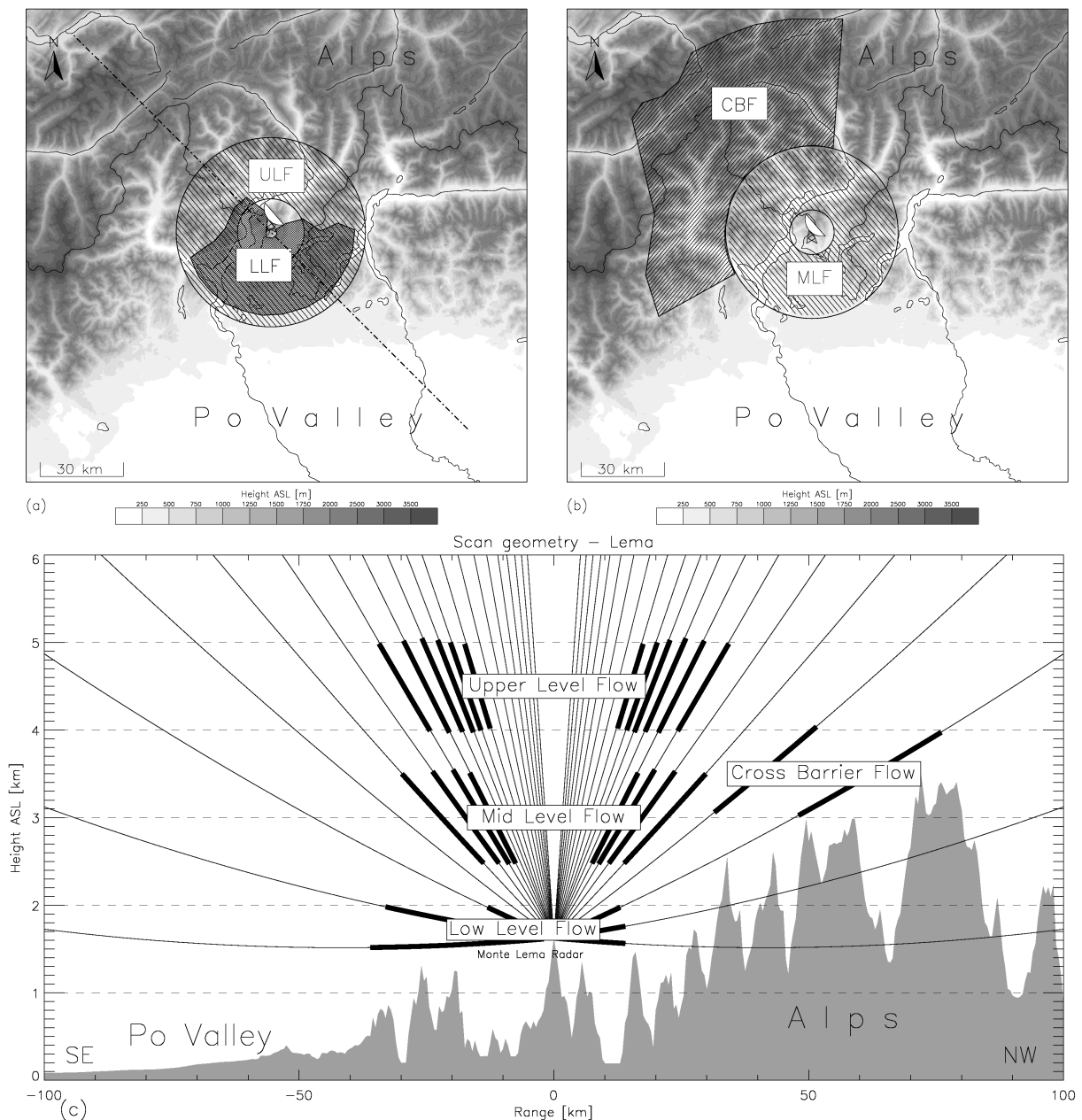
Figure 2.10: *Location of the four regions in which the mesoscale flows are estimated by means of Doppler radar measurements. (a) Horizontal extension of Low Level Flow (LLF) and Upper Level Flow (ULF); (b) Horizontal extension of Mid Level Flow (MLF) and Cross Barrier Flow (CBF); (c) Vertical cross section performed along the dotted line in panel (a) showing the 20 elevation angles of the Monte Lema radar scan strategy (thin lines) and the regions selected for the flow estimates (thick lines).*

Lago Maggiore region, and, as a consequence, the presence of the orographic forcing does not appear in the images. The number of total hours of precipitation, as well as the number of precipitation events involved in each subset, are indicated in the corners of each panel. Consistent with Yuter et al. (2011), figure 2.11 clearly shows that precipitation frequencies increase with increasing intensity of the flows. The direction of the flows, on the other hand, regulates the spatial distribution of the frequencies: the largest frequencies are measured in the regions where the direction of the flows is perpendicular to the main orographic orientation, represented in figure 2.11 by the black line. The largest mean rain rates are also observed in those regions (not shown), indicating that the rain in these areas is not only more frequent, but also more intense. Downstream rain shadows and upstream local enhancement of precipitation are seen in figure 2.11. These features were already observed to cause significant differences in the magnitude of flooding on adjacent mountainous areas, in particular when rainfall is dominated by the orographic forcing (e.g Brady and Waldstreicher (2001); Ralph et al. (2003); Yuter et al. (2011)). The classes corresponding to southerly and south-easterly winds result the most populated (except for the ULF); as a consequence, the spatial distribution of rainfall frequencies in these cases is very similar to that of figure 2.7. In particular, rain frequencies corresponding to low LLF and MLF intensities (less than 5 m/s) are smaller than the frequencies of figure 2.7, whereas with higher velocities (larger than 10 m/s) they are larger; with moderate velocities, the frequencies are very similar. South-westerly flow leads to rainfall more frequent than average only for ULF. Within the LLF classes, strong southerly and south-easterly flows cause the largest mean rain rates and frequencies in the region. In particular, the heaviest rain concentrates in an ellipsis-shaped area north-west of the lake (between Toce and Maggia Valleys), in accordance with Kappenberger and Kerkmann (1997). In this case, both frequencies and mean rain rates tend to decrease moving from that area not only towards the Po Valley and the inner Alps, but also eastwards and south-westwards, along the directions parallel to the orientation of the Alpine ridge.

The qualitative distribution of rainfall in relation to the direction of the impinging flow generally agrees with Houze et al. (2001). However, precipitation radar data used in this study give a more complete description of the real ground level rainfall rate over the whole Lago Maggiore region, as a consequence of the sophisticated data processing (see Sect.3.3.1). Moreover, the frequencies of figure 2.11 are much less influenced by very large values of reflectivity, beam shielding, residual ground clutter and vertical reflectivity profile than the mean reflectivities at constant height computed in previous studies (Houze et al., 2001; James and Houze, 2005).
This stage of the analysis highlights the basic role of the orographic forcing in determining precipitation amounts and distribution in this region. Since the air is assumed to be saturated or almost saturated by the time it produces rainfall over the Alps (see Sec.2.3.2), higher velocities of the impinging flows cause a larger flux of moisture towards the Alps, which is orographically forced to ascent, resulting in larger vertical velocities and thus more precipitation than in the case with low velocities.

2.6.2   Precipitation frequency analysis based on stability

In order to investigate the sensitivity of orographic precipitation mechanisms to variations in the thermodynamic properties of the atmosphere at low levels, precipitation frequencies and mean rain rates based on the values of the moist Brunt-Väisälä frequency were obtained. In the first stage of this analysis, moist static stability was estimated by considering radiosoundings data of Milano. The subsets of radar images were simply given by the rain measured in correspondence with soundings unstable, neutral and stable in the layer 350-1000m (following the same grouping of values proposed in Sect.2.4). In the second step of the analysis, moist static stability was estimated from two pairs of ground stations located within the Lago Maggiore area: Locarno Monti and Cimetta, Stabio and Monte Generoso (see figure 3.1 and Sect.2.2.3). The results of the precipitation *frequency* analysis do not show significant differences between unstable, neutral and stable conditions. However, *mean rain rates* measured in unstable and neutral cases are slightly larger than in stable ones (not shown).

2.6.3 Precipitation frequency analysis based on flows and stability

The sensitivity of orographic precipitation mechanisms to both dynamic and thermodynamic different conditions of the impinging flow is here investigated.
Mean rain rates and precipitation frequencies corresponding to stable, neutral and unstable cases for various classes of intensity of southerly and south-easterly LLF (the directions which present the largest rain frequencies in figure 2.11(a)) were calculated. Brunt Väisälä frequency was obtained from both ground stations and radiosoundings measurements. Figure 2.12 shows percentage frequencies of rain rates exceeding 1 mm/h for three classes of moist static stability derived from Stabio and Monte Generoso stations data, and for three classes of intensity of south-easterly LLF. The most important differences between the panels are given by the velocity of the flow; however, also moist static stability plays an important role in determining the frequency of precipitation. In fact, rainfall frequencies are significantly larger over the mountains with unstable and neutral conditions than with a stable low atmosphere. Mean rain rates were also found to be larger with unstable and neutral conditions than with a stable stratification (not shown).

The behaviour of a flow impinging an obstacle can be described by the Froude number $Fr=U/(NH)$ (or nondimensional mountain height $M=1/Fr$), where U is the upstream flow speed perpendicular to the terrain, N is the Brunt-Väisälä frequency and H is the height of the mountain barrier. Fr indicates whether or not the upstream flow has enough kinetic energy to rise over the barrier (Durran, 1990; Houze, 1993). Flow with an high Fr rises easily over a mountain, resulting in a robust upslope flow which can enhance precipitation over the windward side of the obstacle; flow with low Fr tends to be blocked by the mountain, and lifting and enhancement of rainfall can also occurr upstream of the barrier. As mentioned in Sect.3.1, Houze et al. (2001) and Medina and Houze (2003) found significant differences in precipitation amounts and distribution in the Lago Maggiore region between high and low Fr flow regimes. Stimulated by their results, in the last stage of this study statistical analyses based on Fr were performed. In this analysis southerly and south-easterly LLF was considered as an estimate of the flow impinging perpendicularly to the mountain barrier. The average height of the alpine crest in the region, representative of the mountain height in the calculation of Fr, was assumed to be 3 km. Moist Brunt-Väisälä frequency was used, and it was obtained both by ground stations and radiosoundings data. Figure 2.13 presents the results of the precipitation frequency analysis; the spatial domain is larger than in the previous figures and it includes also a large part of the Po Valley, in order to detect a possible enhancement of precipitation upstream of the Alpine ridge. The first line of figure 2.13 is relative to Fr calculated with the stability derived from Locarno Monti and Cimetta ground stations data. About 62% of the hours of precipitation presents negative values of squared moist static stability, thus not permitting to calculate the Froude number. In this case, precipitation appears to be enhanced on the first Alpine slopes north-west of Lago Maggiore, originating a band of large rain frequencies in that area (not shown). In the remaining time periods, with positive squared moist static stability, a large difference in rain frequencies between cases with Froude number smaller and larger than 1 is seen in figure 2.13: the precipitation is largely enhanced over the mountains and very large rainfall frequencies are measured also in the inner part of the Alps with Froude numbers larger than 1 (7% of total time of precipitation). With Froude numbers between 0 and 1 (about 31% of total time), precipitation frequencies are smaller than in other cases. Mean rain rates analysis also gave similar results, with the most intense precipitation being observed in the high rainfall frequency regions. The results obtained with stability derived from radiosoundings data are slightly different. In fact, rainfall frequencies with Fr larger than 1 are generally smaller in the Lago Maggiore region and in the Po Valley as compared to the previous case. With Fr smaller than 1 rain frequencies over the Po Valley are slightly higher with respect to Fr larger than 1 cases. However, the rainfall pattern with Fr smaller than 1 is rather far from indicating an upstream enhancement of rainfall like that shown by Houze et al. (2001) and observed in IOP 8 MAP case (Medina and Houze, 2003; Bousquet and Smull, 2003). The absence of such upstream enhancement might be due to the fact that only cases of

orographic rainfall occurred within the Lago Maggiore region are examined in this study, while Houze et al. (2001) considered all precipitation events seen by radar during autumn 1998 and 1999, including the ones which produced rainfall mostly in the Po Valley. However, this study shows that cases of orographic precipitation occurring in the Lago Maggiore region characterized by *Fr* smaller than 1 do not typically exhibit an upstream enhancement of precipitation in the plains ahead of the Alpine ridge. Figure 2.13 is a further subdivision of the cases with positive squared moist Brunt-Väisälä frequency; rain frequencies shown in that figure and mean rain rates analysis (not shown) indicate that *Fr* larger than 1 flow regimes cause the most frequent and intense rainfall in the Lago Maggiore region within the whole 106-days data set.

The statistical analyses based on the value of the Froude number were further stratified depending on the velocity of the impinging flow. Figure 2.14 shows that the differences in rain frequencies between *Fr* larger than 1 and *Fr* smaller than 1 flows regimes are similar to those shown in figure 2.13, independently on the upstream wind velocity. However, these differences are quantitatively much smaller than those due to the different flow intensity. Therefore, this last stage of the investigation confirmed that wind intensity is much more important than both air mass stability and Froude number in regulating the magnitude of orographic rainfall, as shown also by figure 2.12 and by the recent results of Yuter et al. (2011) for the Portland region (Oregon).

2.7   Conclusions

This study investigated the relation between airflow, air mass stability and orographic precipitation in the Lago Maggiore area, which is located in the southern part of the European Alps between Italy and Switzerland. The aim of the analyses presented in this paper is to establish the scientific framework on which to base an heuristic system for nowcasting the location and the evolution of orographic rainfall, currently being developed at MeteoSwiss. A general characterization of the kinematic and thermodynamic features of 58 precipitation events, corresponding in total to 106 days of rainfall, was given in the paper. Vertical profiles of correlation coefficients between the upslope component of the upstream wind and radar-derived rain rates permitted to identify the layers whose mean velocity correlates better than others to the mean rainfall measured in the Lago Maggiore region. These layers are located around 1 km asl about 50 km upstream of the barrier, around 3 km asl above the first Alpine peaks. Four mesoscale flows were then estimated from Doppler radar measurements within these layers and in other significant regions.

The role of wind speed, wind direction and air mass stability in determining orographic rain amounts and distribution was investigated by means of precipitation frequency and mean rain rates analyses. Radar maps of percentage frequencies of rain rate exceeding 1 mm/h at the ground corresponding to specific ranges of values of atmospheric dynamic and thermodynamic parameters were presented. A direct relation between the intensity of the flows and rainfall frequencies is clearly shown in the paper. The location of the maxima frequencies, on the other hand, is determined by the direction of the impinging flows. The stability of the low atmosphere was estimated from both Milano radiosoundings and ground stations data. Moist static stability derived from pairs of adjacent ground stations located at different elevations within the Lago Maggiore region was found to be a significant environmental parameter in regulating rainfall intensity in the mountains: potentially unstable lower atmospheric conditions were shown to cause more precipitation over the Alps as compared to stable cases. However, the strength of the impinging flow has a larger impact on the intensity and frequency of precipitation at a given location with respect to variations in moist static stability. Variations in rainfall frequencies as a function of Froude number were also dominated by the impact of wind speed. An enhancement of precipitation upstream of the barrier was not observed with low Froude number flows.

The findings of this study constitute the scientific framework necessary to build an heuristic system for nowcasting orographic precipitation in the Alpine region by exploiting the presence of the orographic forcing. In fact, the precipitation frequency analysis showed that the orographic forcing gives repeatability to the rainfall patterns typically observed in the Lago Maggiore region with certain environmental conditions. These patterns are related not only to the orographic features of the area but also to the dynamic and thermodynamic characteristics of the impinging flow. Therefore, upstream wind intensity, direction and air mass stability can be used as short-term predictors for nowcasting the location, the intensity and the duration of orographic rainfall. Probabilistic predictions for the next few hours of the duration and the intensity of the rain in particular geographical areas will be based on the precipitation field observed at the time of forecast, characteristic features and significant changes in the mesoscale flows, upstream air mass stability, and on other observational evidences. The analysis of the role of water vapour in determining orographic precipitation patterns is one of the next steps, and it could be added as a predictor in the nowcasting system.

Low Level Flow
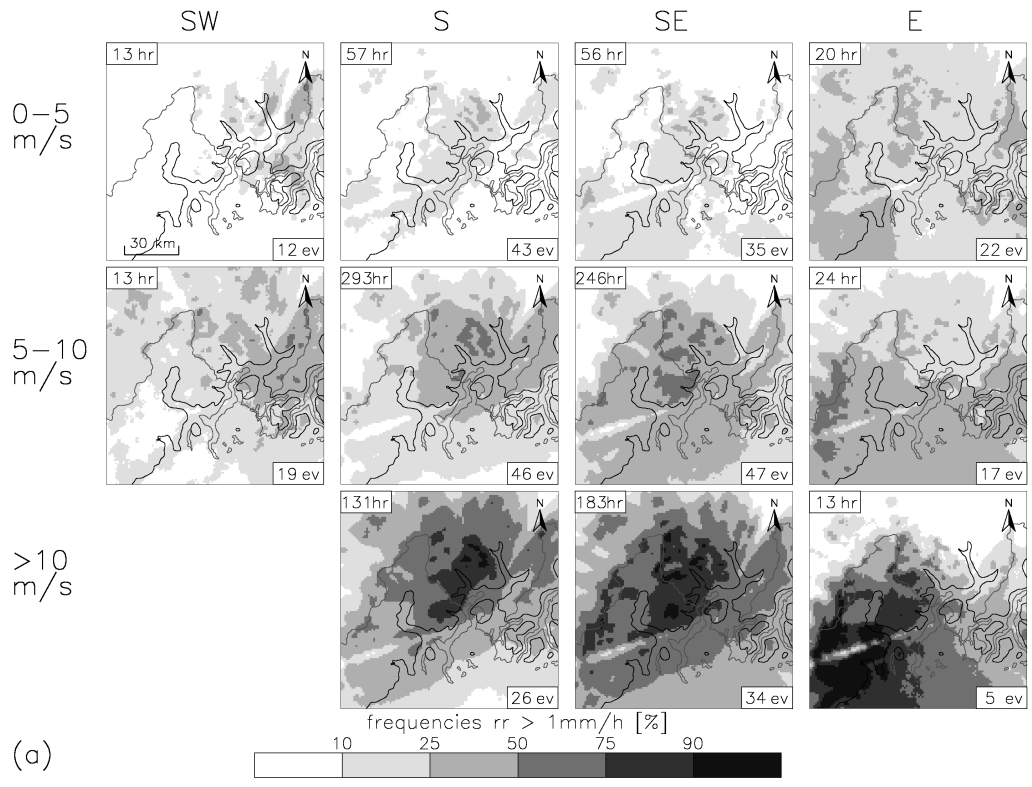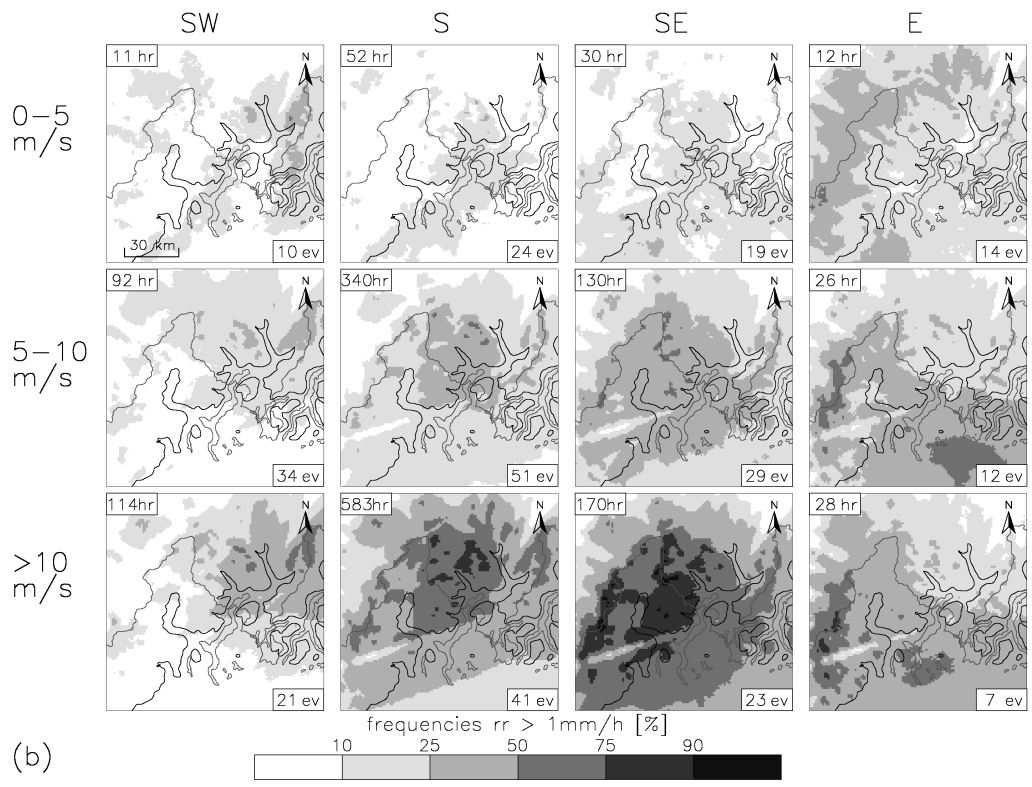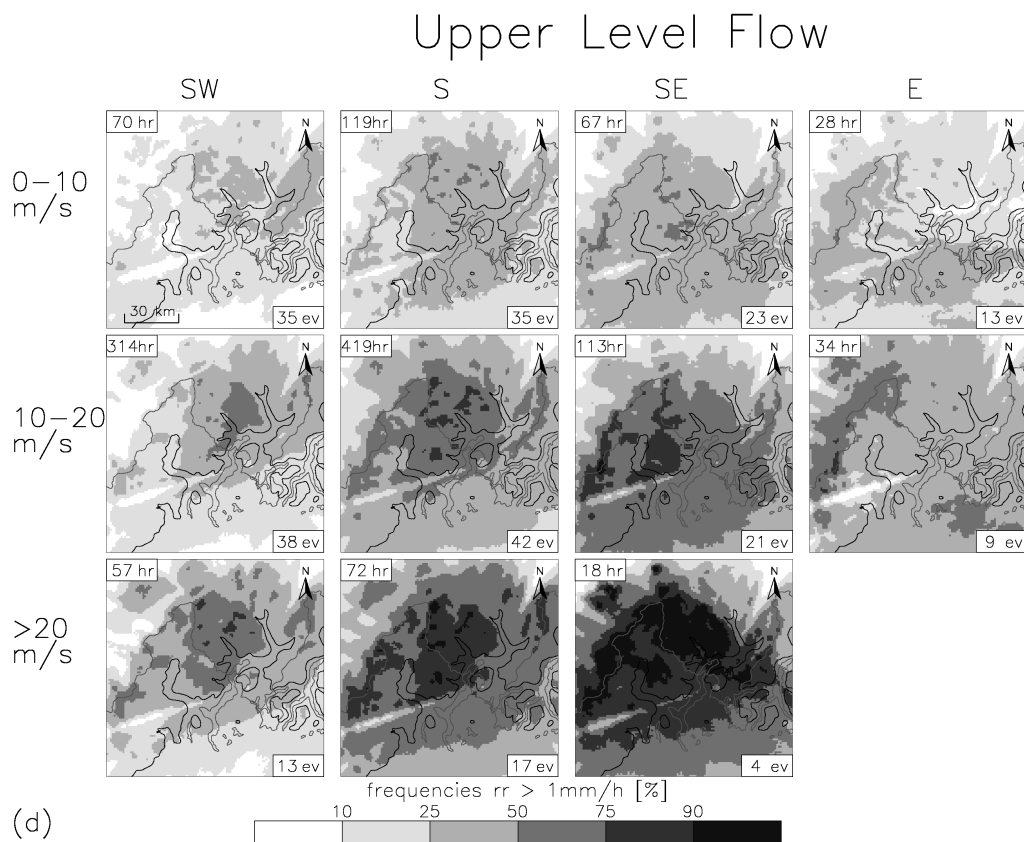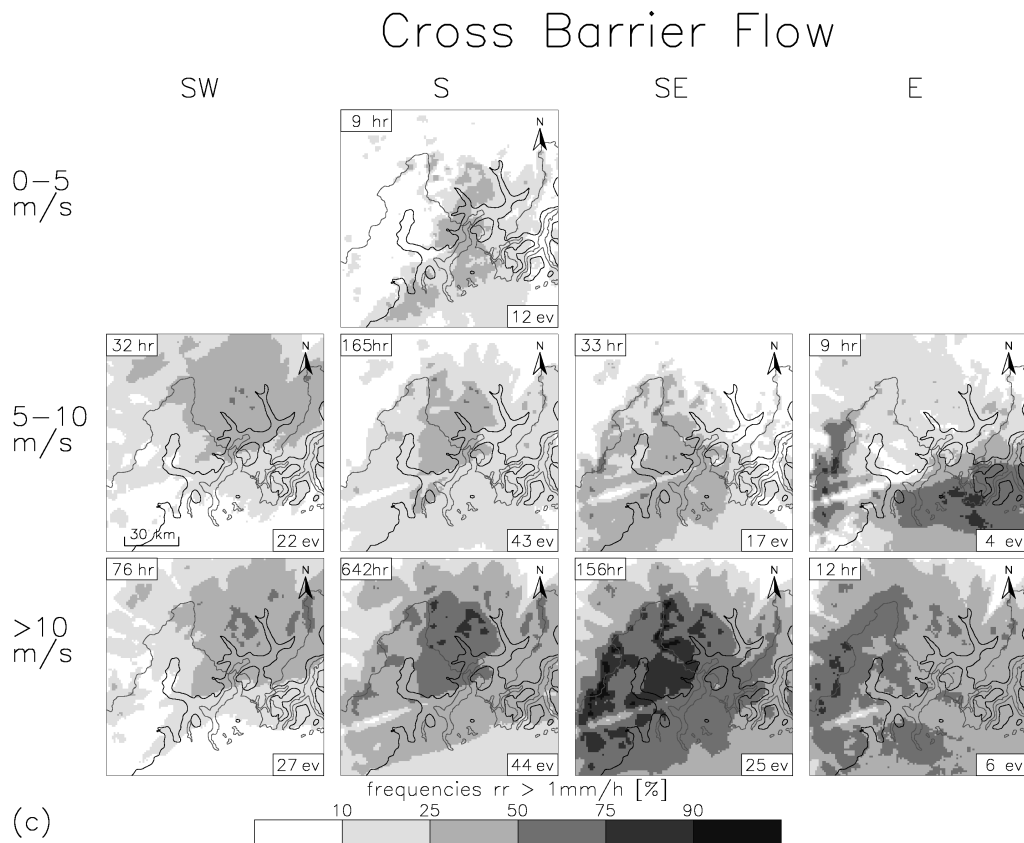
	SW	S	SE	E

frequencies rr > 1mm/h [%]

10 25 50 75 90

(a)

Mid Level Flow

	SW	S	SE	E

frequencies rr > 1mm/h [%]

10 25 50 75 90

(b)

Cross Barrier Flow

SW S SE E

0–5 m/s

5–10 m/s

>10 m/s

frequencies rr > 1mm/h [%]

10   25   50   75   90

(c)

Upper Level Flow

SW S SE E

0–10 m/s

10–20 m/s

>20 m/s

frequencies rr > 1mm/h [%]

10   25   50   75   90

(d)

Figure 2.11: *Percentage frequencies of exceeding 1 mm/h of precipitation in the Lago Maggiore region for different classes of intensities and directions of (a) Low Level Flow (b) Mid Level Flow (c) Cross Barrier Flow and (d) Upper Level Flow . The total hours of precipitation and the number of precipitation events in each class are indicated at the top left and at the bottom right corner of each panel respectively. If the total hours of precipitation in one class are less than 5, frequencies corresponding to that class are not presented.*

44

Figure 2.12: *Percentage frequencies of exceeding 1 mm/h of precipitation in the Lago Maggiore region for unstable, neutral and stable cases and for three classes of intensity of Low Level Flow from South-East. Moist Brunt-Väisälä frequency derived from the couple of stations Stabio (SBO, 353 m) and Monte Generoso (GEN, 1608 m) was used to classify the stratification as unstable, neutral and stable (see figure 3.1).*
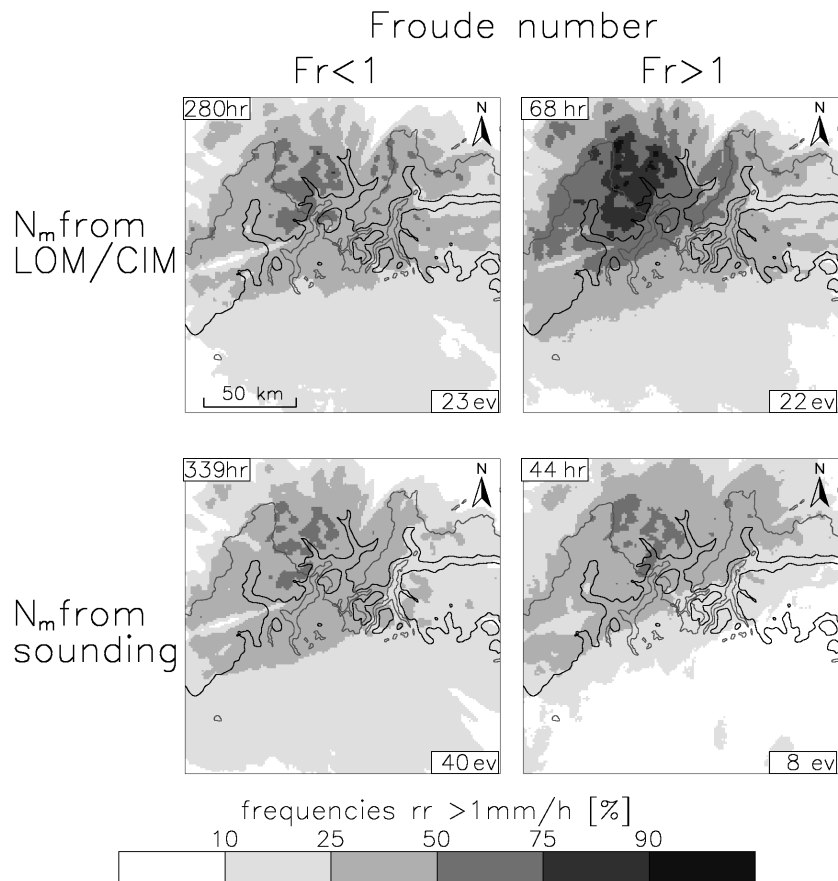
Figure 2.13: *Percentage frequencies of exceeding 1 mm/h of precipitation in the Lago Maggiore region and surrounding areas based on Froude number. In the first row moist static stability is derived from Locarno Monti and Cimetta ground stations (see figure 3.1). In the second row, stability is obtained from Milano radiosoundings data (mean value in the layer 350-1000m). Flow intensity is derived from the LLF estimated by radar, taking into account only southerly and south-easterly directions. The height of the orographic barrier is assumed to be 3000 m. Froude number is not defined if the Brunt-Väisälä frequency is imaginary. The total hours of precipitation and the number of precipitation events populating each class are indicated at the top left and at the bottom right corner of each panel respectively. The spatial domain of the boxes is 170x170 km.*
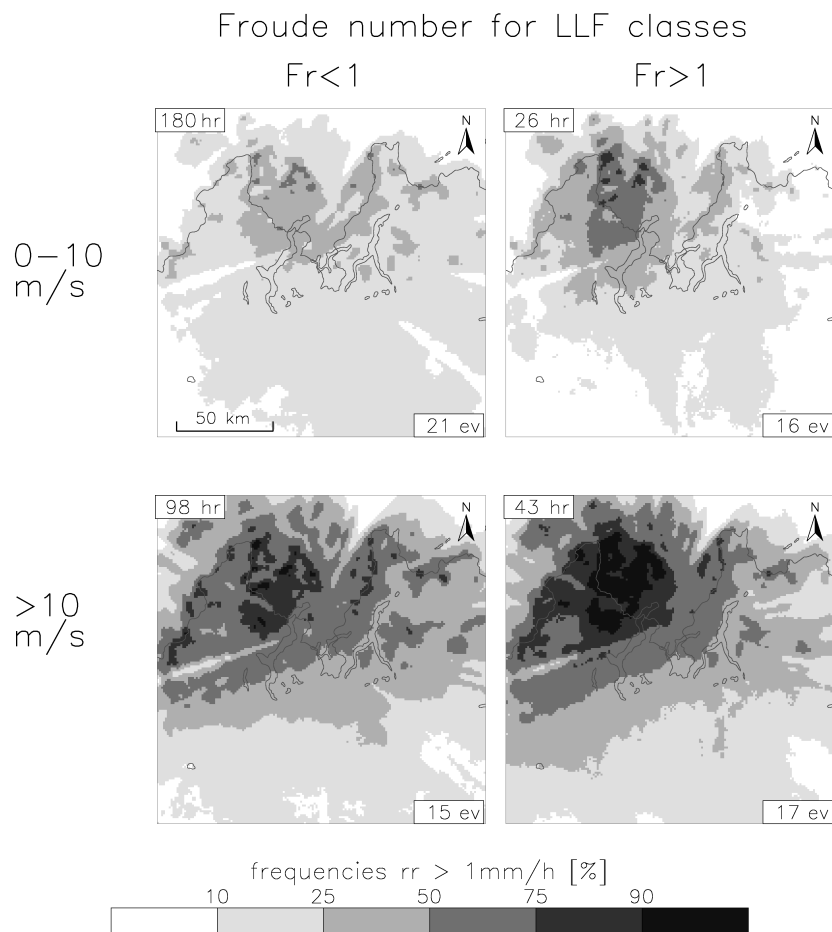
Figure 2.14: *Percentage frequencies of exceeding 1 mm/h of precipitation in the Lago Maggiore region and surrounding areas based on Froude number for two classes of intensity of southerly and south-easterly Low Level Flow. Moist static stability is derived from Locarno Monti and Cimetta ground stations (see figure 3.1). The height of the orographic barrier is assumed to be 3000 m. The total hours of precipitation and the number of precipitation events populating each class are indicated at the top left and at the bottom right corner of each panel respectively. The spatial domain of the boxes is 170x170 km.*

Chapter 3

NORA – Nowcasting of Orographic Rainfall by means of Analogues

Abstract

A novel analogue-based heuristic tool for nowcasting orographic precipitation is presented. The system takes advantage of the orographic forcing, which determines a strong relation between mesoscale flows, air mass stability and rainfall patterns. These quantities are used as predictors of precipitation. In particular, past situations with the predictors most similar to those observed at the current instant are identified by searching in a large historical data set. Deterministic and probabilistic forecasts are then generated every five minutes as new observations are available, based on the rainfall observed by radar after the analogous situations. The analogue method provides a natural way to incorporate evolution of precipitation into the nowcasting system and to express forecast uncertainty by means of ensembles.

A total of 127 days of long-lasting orographic precipitation constitutes the historical data set in which the analogous situations are searched. The system is developed for the Lago Maggiore region in the southern part of the European Alps. Given the availability of radar data and the presence of a strong orographic forcing, it can be extended to other mountainous regions. An evaluation of the skill of the system shows that the heuristic tool performs better than Eulerian persistence for predictions with lead time larger than one hour, and better than the numerical model COSMO2 for forecasts with lead time up to 4 hours.

3.1 Introduction

3.1.1 The challenge of nowcasting orographic precipitation

Orographic rainfall is responsible for most of the floods which affect the Alpine region. During intense precipitation events, meteorological and hydrological services need frequently updated very short-term predictions of the intensity, location and evolution of orographic rainfall. Thus, nowcasting tools, covering the 0-6 hours time frame, assume high importance in the last stage of the weather forecasting process, as recently confirmed by the hydrometeorological forecast demonstration project MAP D-PHASE (Rotach and co authors, 2009) and IMPRINTS (http://imprints-fp7.eu).

A lot of field experiments conducted in the last twenty years were devoted to precipitation over complex terrain: TAMEX (Kuo and Chen, 1990), CALJET (Ralph et al., 1999), IMPROVE (Stoelinga et al., 2003), MAP (Rotunno and Houze, 2007). The main objective of these projects was a better understanding of orographic precipitation mechanisms, without giving a special emphasis to nowcasting issues. Thus, there is a lack of nowcasting systems specifically developed for orographic rainfall.

The inclusion of orographic precipitation producing mechanisms in nowcasting tools is the subject of active research. Recently Roberts et al. (2010) employed high resolution observations collected during TiMREX (Lee et al., 2007) over Taiwan to examine storm formation and evolution, with the aim to develop a tool for nowcasting heavy orographic rainfall.

Nowcasting of precipitation in mountainous regions is a very challenging task, because of the complexity of the meteorological phenomena occurring over the orography and the difficulty to obtain detailed and precise observations of rainfall (Mecklenburg et al., 2000). In fact, the mechanisms that produce orographic precipitation depend on both airflow dynamics and cloud microphysics, thus involving different spatial and temporal scales. The dynamic aspects depend on the upstream characteristics of the flow and on the terrain configuration, which together determine the ways in which the flow interacts with the orography; microphysical aspects determine how much and how quickly cloud water is converted into precipitation and how fast precipitation falls (e.g. Alpert, 1986; Smith et al., 2005). Review summaries of orographic precipitation processes can be found in Smith (1979a), Barros and Lettenmaier (2010), Roe (2005) and Smith (2006). The most evident effect of the interaction between mountains and atmospheric flow is the enhancement of precipitation that occurs on the windward slope of the mountains, determining strong spatial gradients of rainfall in mountainous regions. As reported in Roe (2005), the amplitude of the rain shadow and the relation between orography and precipitation at scales smaller than the mountain chain size are complex, and the subject of active research. For example, Foresti and Pozdnoukhov (2011) demonstrate that the enhancement of rainfall due to orography, which leads to stationary rainfall cells, occurs on the meso-gamma scale; moreover, they show that preferred regions for stationary cells are the upwind slopes and the top of hills, in agreement with Anders et al. (2007). The ways by which the atmospheric flow interacts with the orography can vary greatly not only from one storm to another, but also during a single precipitation event, as environmental conditions change. Orographic rainfall, therefore, is intrinsically a transient phenomenon (Roe, 2005). For this reason several physical models of orographic rainfall developed in the past are not suitable for forecasting rainfall patterns over complex orography on short time scales (e.g. Hill, 1983; Alpert and Shafir, 1989; Smith and Barstad, 2004).

The large spatial and temporal variability of orographic precipitation makes the task of nowcasting very difficult: errors of a few kilometers in the location of the predicted rainfall can have a large impact on rivers runoff of small basins. Moreover, such large variability requires monitoring systems capable to measure rainfall with high spatial and temporal resolution. Rain gauges networks are typically not dense enough to reproduce such high spatial variability: even in the European Alps, one of the regions with the densest rain gauge network, typical spacing between stations is 10 km, whereas the precipitation distribution varies at scales smaller than 10 km (e.g. Frei and Schar, 1998; Smith et al., 2003). Ground-based radars, on the other hand, are designed to monitor precipitation over large areas with high spatial and temporal resolution. Using weather radars for precipitation measurements in mountainous regions, however, is a challenge: ground clutter and beam shielding strongly affect the accuracy of radar estimates, and need to be treated properly if quantitative estimates of precipitation amounts are to be produced in a routine manner (Joss and Waldvogel, 1990).

In the smallest steep Alpine catchments heavy orographic precipitation combined with rapid runoff can lead to flash floods, which are characterized by rapid occurence resulting in a very limited opportunity for warnings to be prepared and issued (Collier, 2007). Catchments of up to 400 km^2 that are capable of generating flood hydrographs with times to peak of up to 6 hours are regarded as potential flash flood catchments (e.g. Georgakakos, 1986; Collier, 2007). For example, in Verzasca Valley, a small and steep catchment (186 km^2) located in the Southern Alps (see figure 3.1), the time between a precipitation impulse and the main runoff response at the outlet is of the order of 1 to 2 hours (Germann et al., 2009). This means that coupling radar observations with a runoff model results in 1-2 hours lead time for predicting a flash flood peak, even if no precipitation forecast is available. For many small mountainous catchments with very short response times, we do not have the luxury to wait until the last moment to issue an alert. Nowcasting of rainfall in small alpine catchments, therefore, is aimed to extend such short lead times. In particular, nowcasting methods should provide

forecasts of precipitation up to 6-8 hours ahead, with an updating frequency not larger than 1 hour and a spatial resolution of a few kilometers.

3.1.2   Rainfall nowcasting methodologies

There are two main approaches to operational very short-term quantitative precipitation forecasting: the first is based on heuristic systems, the second on numerical weather prediction models.

Radar rainfall data are extensively used for the development of heuristic nowcasting techniques, given its high temporal and spatial resolution. The simplest radar-based nowcasting methodology is the Eulerian persistence: the current radar image is taken as forecast (e.g., Germann and Zawadzki, 2002). In order to produce probabilistic forecasts, Germann and Zawadzki (2004) introduced the concept of Local Eulerian persistence. Assuming that the spatial variability of the precipitation field at a fixed time is correlated with the temporal variability at a fixed position, this technique makes a persistence forecast determining the probability distribution in the neighborhood of the point of interest. While the Eulerian persistence approach can be successful for precipitation fields with negligible advection, it can lead to large forecast errors in predicting the position and intensity of moving rainfall patterns. By advecting the precipitation patterns following the field of storm motion, a Lagrangian persistence forecast is produced. This nowcasting method corresponds to the persistence of precipitation in storm coordinates. There are two sources of error in Lagrangian persistence forecasts: growth and dissipation of precipitation and changes in the storm motion field. For these reasons Lagrangian persistence is successful as long as advection explains a significant part of the temporal variation of the rainfall fields. Lagrangian extrapolation techniques make use of different methodologies. For example, Austin and Bellon (1974), Bellon and Austin (1978) and Burlando et al. (1996) determined the displacement vector by maximizing cross correlation between successive radar observations. Information on scales of precipitation was also used in order to optimize the Lagrangian advection scheme (Seed, 2003) and to get probabilistic forecasts (e.g., Germann and Zawadzki, 2004; Cornford, 2004). As extensively reported in Reyniers (2008), however, there are two main families of Lagrangian persistence nowcasting systems: cell tracking and area tracking. The former are object-oriented: they are used to identify thunderstorms and to predict their position in future (e.g., Hering et al., 2004). The latter produce quantitative predictions of precipitation for the whole radar grid (e.g., Turner et al., 2004). Eulerian and Lagrangian persistence are used also to investigate predictability of precipitation at different scales (e.g., Zawadzki et al., 1994; Grecu and Krajewski, 2000; Germann and Zawadzki, 2006, and references therein).

As an alternative to heuristic systems, numerical weather prediction models are also used for very short-term forecasting of precipitation. Even though they include the full set of equations which describe the atmospheric processes, there are some limitations to their usage for operational nowcasting of precipitation. First, current numerical models are not able to fully digest the observations at the scale required by the applications. Second, the assimilation and the initialisation cycles and the time required to obtain the forecast are too long with respect to the demands of the forecasters and end users. Third, the spatial resolution and the updating frequency of the forecasts are too coarse for nowcasting applications. For example, COSMO2 numerical model (http://cosmo-model.org) is updated every 3 hours, the forecasts require about 2 hours to be computed and disseminated, and the spatial resolution of 2.2 km enables to resolve processes occurring on the spatial scales of 8 km or larger. Such values are too coarse for the nowcasting requirements already illustrated.

Since the performance of nowcasting systems decreases fast with lead time, whereas the skill of numerical models is less affected by this fast deterioration, some studies propose a merging of the forecasts obtained with numerical weather prediction models and heuristic systems (e.g., Golding, 1998; Pierce et al., 2000; Bowler et al., 2006; Atencia et al., 2010). Recently Wilson et al. (2010) showed that these techniques did not perform better than nowcasting systems during the Beijing 2008 Forecast Demonstration Project; they state that the blending approach will be successful as long as numerical

models will improve on the nowcasting spatio-temporal scale.

3.1.3   Forecasting using analogues

Forecasting using analogues is one of the oldest methods for weather forecasting; the word *analogues* means two states of the atmosphere which resemble each other rather closely (Lorenz, 1963). The main hypothesis of analogues based forecasting is that similar atmospheric conditions will evolve in similar ways. Thus, once an analogue is found for the current situation, the forecast for a given period of time can be obtained by the evolution of the meteorological conditions observed after that similar past situation (e.g. Duband, 1970; Radinovic, 1975; Bergen and Harnack, 1982). The major limitation of the analogue approach is the size of the archive in which the analogues are searched, which has to be very long for the global scale (e.g Toth, 1991; Van den Dool, 1994). However, it is possible to find good analogues even in short data sets if the search for analogues is performed over a small area, in particular if the flow is persistent (e.g. Van den Dool, 1989; Root et al., 2007). The advantages of analogue forecasting lies in its simplicity: although it does not introduce any simplification in the physics of the atmosphere, it can provide realistic weather forecasts (e.g. Radinovic, 1975; Bergen and Harnack, 1982; Van den Dool, 1989). In fact, the past observed values used to make the forecast contain the orographic, diabatic and other local effects which characterize the area of interest and influence the behavior of the quantities to be predicted (e.g Ruosteenoja, 1988; Obled et al., 2002; Diomede et al., 2008). With the advent of fast computer processors, analogue forecasting is now applied to a large variety of problems (e.g. Fraedrich et al., 2003; Bo et al., 2009). Recently, Obled et al. (2002) and Diomede et al. (2008) applied analogues based techniques for forecasting precipitation in hydrological catchments. Obled et al. (2002) produced probabilistic forecasts of daily rainfall up to 6 days ahead. The analogy was searched in terms of the 1000 and 700 hPa geopotential height over a window covering western Europe. Their method was calibrated over about 50 catchments located in France, Italy and Spain, using a 43-years meteorological and hydrological archive. They showed that the analogue approach performs better than both climatology and persistence. However, a comparison with a state of the art medium-range numerical weather prediction model would be required to better highlight the advantages of the analogue approach. Diomede et al. (2008) searched analogues in the combination of geopotential height at 500 hPa and vertical velocity at 700 hPa over western Europe and east Atlantic in a data set given by the autumn seasons ranging from 1990 to 2000. An ensemble of hourly quantitative precipitation forecasts for the Reno catchment, located in the Italian Appennines, was then generated looking at the rainfall measured by the 45 raingauges spread over the basin in the 3 days following the analogue. Even though their analogue forecast led to discharge flow predictions better than that provided by the LAMBO numerical model, Diomede et al. (2008) state that the analogue method does not appear to be suitable for streamflow forecasting because the large spread among the members of the ensemble makes it difficult to issue real-time flood warnings. The reason for the large spread resides in the limited historical data set. However, the authors highlight that the forecast spread conveyed by the analogue-based ensemble could be joined to the deterministic numerical model forecast and used to quantify the hydrological forecast uncertainty.

3.1.4   This paper

In this paper we present NORA (Nowcasting of Orographic Rainfall by means of Analogues), a novel analogue-based heuristic nowcasting tool for very short term forecasting of precipitation. Since the orographic forcing dominates the patterns of rainfall in the mountains (e.g. Houze et al., 2001; Panziera and Germann, 2010; Yuter et al., 2011), it can be exploited for nowcasting of precipitation. NORA takes benefit not only from the effects of the orographic forcing, but also from the recent improvements of the Swiss weather radar precipitation estimates (Germann et al., 2006).
The concept behind NORA is described in section 3.2. Section 3.3 presents the data and the methods

used by NORA algorithms. A comparison of NORA forecasts with Eulerian persistence and COSMO2 is given in section 3.4, whereas the main findings of the study are reported and discussed in section 3.5.

3.2 The concept of NORA

In Panziera and Germann (2010), from now on PG10, we analysed a large number of long-lasting orographic precipitation events occurred over the Lago Maggiore region, which is located in the southern part of the European Alps between Italy and Switzerland (see figure 3.1). In PG10 we demonstrated that the orographic forcing gives repeatability to the rainfall patterns observed in the mountains with certain environmental conditions. In particular, we found a strong relation between precipitation patterns and wind intensity, direction and air mass stability. This paper describes how these meteorological quantities are used as *predictors* for nowcasting the location, intensity and evolution of orographic rainfall.

The basic idea of NORA is to search in the past for *analogues*, i.e. the situations with predictors
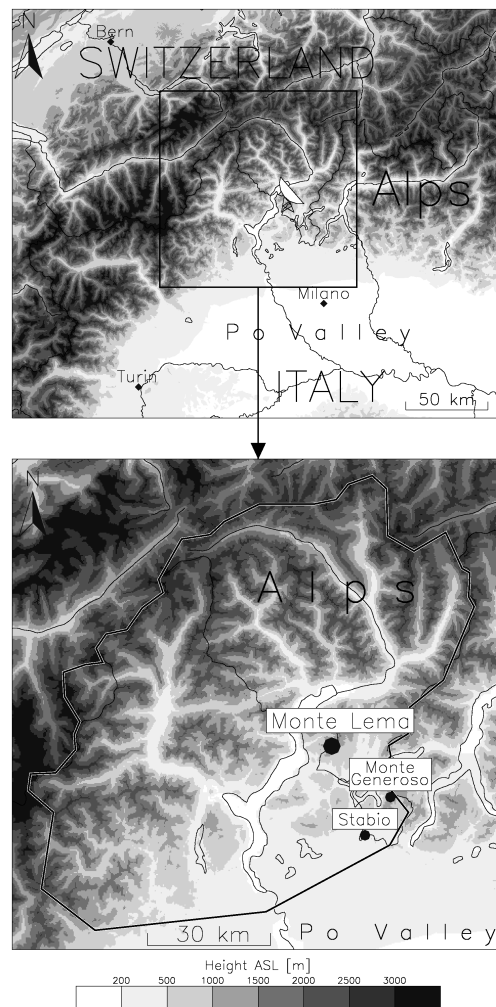
Figure 3.1: *Top: Orographic map of the Central Alps between Italy and Switzerland. The location of MeteoSwiss Monte Lema radar (1625 m above sea level) is indicated by the radar symbol. Bottom: Zoom into the Lago Maggiore region, with the location of the radar and of the ground stations considered in this study: Stabio (SBO, 353 m) and Monte Generoso (GEN, 1608 m). The black lines denote the Maggiore Lake catchment (7830 km^2) and Verzasca Valley (186 km^2).*

and rainfall patterns most similar to those observed at the current instant. Quantitative precipitation forecasts are then based on the rainfall accumulated in the hours following the analogues. The originality of this approach, with respect to previously developed analogue methods, lies in the following aspects. First, the analogues are found by means of specific predictors observed to have a strong relation with orographic precipitation at the mesoscale (four winds and air mass stability) and by means of properties derived by the radar image. Second, the analogue forecast has been designed and optimized for the nowcasting time frame. Third, the predictand and the predictors, as well as the data set in which analogues are searched, come from high spatial and temporal resolution radar measurements.

The main strengths of NORA are the following:

1. The algorithm produces every 5 minutes precipitation forecasts up to several hours ahead in a short time (typically 2 minutes processing time).

2. Predicted rainfall fields have realistic statistical properties, since they result from precipitation fields observed in the past.

3. The system can be targeted for specific user requirements.

4. The system makes full use of high spatio-temporal resolution radar rainfall and Doppler velocity data.

Since the forecast is built on past fields of accumulated precipitation, growth and decay of rainfall, which are not accounted for by persistence methods, are automatically taken into account by NORA. The current radar image is also taken as one of the final analogues, so that NORA forecasts include also the information given by the Eulerian persistence approach.

Even though the analogue approach is not able to predict rainfall fields not observed in the past, the sum of the precipitation already accumulated and the rainfall predicted by NORA can result in an event not previously observed. In operational nowcasting this sum of accumulated and predicted rainfall is of fundamental importance, since it is the quantity which actually drives the emergency decisions taken during a precipitation event. In other words, the event-scale accumulation from NORA can be different from the accumulated rainfall fields that are in the historical archive.

The system is developed for the Lago Maggiore region; however, it can also be extended to other mountainous regions, given the availability of local radar data, nearby ground stations at different altitudes and the presence of a strong orographic forcing. Some examples of NORA forecasts are given in figure 3.2, where also Eulerian persistence forecast and observation are represented. Figure 3.2 shows that it is possible to make a forecast better than Eulerian persistence by considering the rainfall observed in the past with similar environmental conditions.

3.3 Data and methods

This section constitutes the detailed technical description of NORA: the data and the methodologies used by the tool to produce rainfall forecasts are presented.

3.3.1 Radar data

The MeteoSwiss weather radar located on the top of Monte Lema (1625 m above sea level, see figure 3.1), one of the southern-most mountains of the Alpine ridge in the Lago Maggiore region, is used to estimate rainfall at the ground and mesoscale winds. Information on rainfall is obtained by the operational MeteoSwiss radar product for quantitative precipitation estimation (Joss and Lee, 1995). Such product represents the best estimate of precipitation at the ground, and it is retrieved
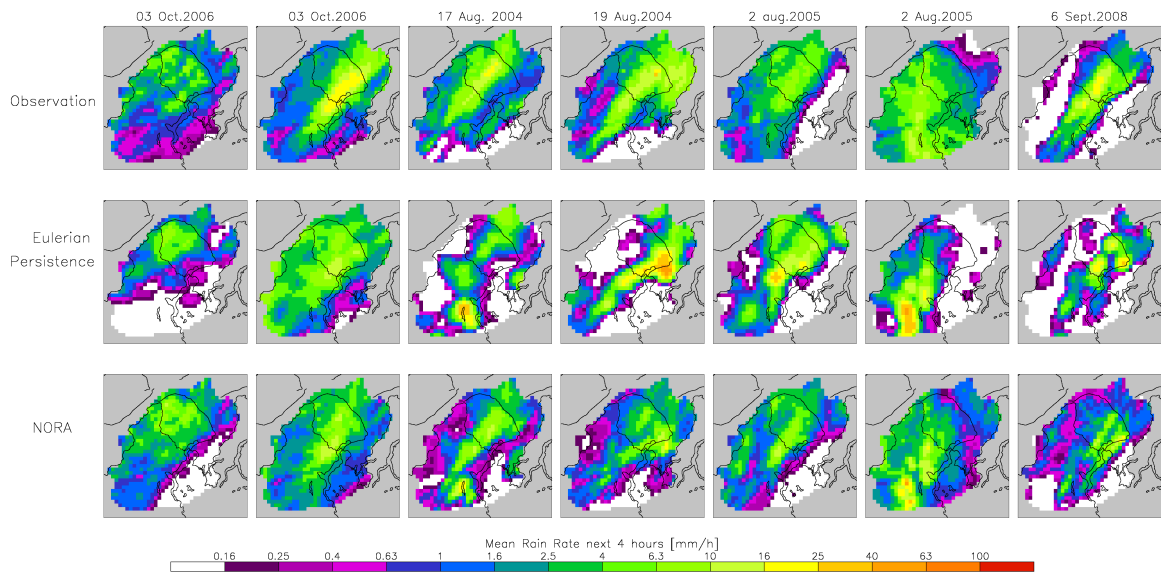
Figure 3.2: *Examples of NORA and Eulerian persistence 0-4 hours forecasts of accumulated precipitation and corresponding radar observations over the Lago Maggiore region. The spatial domain of the panels is the same as for the bottom panel of figure 3.1. The seven past instances at which forecasts were issued were selected from five precipitation events of our historical data set, and are indicated above each column (see section 3.3.3). In order to focus the attention on the rainfall patterns within the Maggiore Lake catchment, pixels external to it were shaded in grey.*

through a weighted mean of all the radar observations aloft. The horizontal spatial resolution of the precipitation map is 1 km x 1 km, the temporal resolution is 5 minutes. For an evaluation of the radar performances in the Lago Maggiore region, see section 2.1 of PG10 and Germann et al. (2006). The mesoscale wind is estimated by Doppler velocity measurements, which have a spatial resolution of 1 degree in azimuth and 1 km in range and are also updated every 5 minutes (Joss et al., 1998).

3.3.2 Ground stations data

A pair of adjacent automated meteorological stations are used by NORA to estimate the stability of the lower atmosphere: Stabio (353 m) and Monte Generoso (1608 m). These stations, which measure the main meteorological parameters every 10 minutes, are located on the first slopes of the Alps very close to the Po Valley (see figure 3.1) at different altitudes, thus permitting to have an estimate of the mean stability of the atmospheric layer comprised between the two stations.

3.3.3 Selection of historical cases

The historical archive in which NORA searches for the analogues results from a trade-off between the following three requirements. First, the data set in which the analogues are searched should be sufficiently large to cover the whole range of phenomena of interest. Second, the archive has to be homogeneous to avoid artefacts due to instrumental changes and different data processing techniques. Third, since NORA is developed for nowcasting precipitation events in which the orographic forcing plays an important role, long-lasting and widespread events typically caused by a large-scale supply of moisture towards the Alps should be selected. Isolated convection and air mass thunderstorms were excluded from the historical data set, as these are less extended in space and time and thus rarely result in critical amounts of rainfall. This third requirement was also dictated by computational reasons: searching for analogues in the whole radar archive of the last years would take too much time

and would not make sense, as most of the days do not have precipitation. Seventy-one precipitation events observed in the Lago Maggiore region from January 2004 to December 2009, corresponding in total to 127 days of precipitation (3050 hours), are thus considered. Details about the choice of the rainfall events are given in section 2.2 of PG10.

For illustration figure 3.3 represents a sequence of radar images extracted from two precipitation events which can be considered typical of those constituting the historical data set. The event of October (panel a) shows stronger precipitation gradients with respect to the December case (panel b); the maximum accumulations were measured for both the events in an ellipsis-shaped area (between Toce and Maggia Valleys) North-West of Maggiore Lake. This geographical region is prone to large accumualations of rainfall, as already noted by Kappenberger and Kerkmann (1997).

3.3.4 Terminology

To specify the temporal period for which the forecast is produced, we make use of the following terminology. A t-hour forecast means a prediction of the rainfall accumulated in the temporal period of t hours. Following the American Meteorological Society glossary, lead time is defined as the length of time between the issuance of the forecast and the occurrence of the phenomena that were predicted. Thus, 1-hour forecast with zero lead time means the prediction of rainfall from 0 to 1 hour ahead, 1-hour forecast with three hours lead time means the prediction from 3 to 4 hours ahead, and so on.

3.3.5 Predictors

The predictors estimated in real-time and used by NORA to find the analogues in the historical archive are mesoscale flows, air mass stability, wet area ratio and image mean flux.

Mesoscale flows

Four mesoscale flows are used as predictors by NORA (see figure 3.4):

1. Low Level Flow (LLF)
   This flow is estimated upstream of the Alps south-east of Maggiore Lake between 1.5 and 2 km above sea level. It monitors the low level wind which is forced to ascend over the mountains. During orographic rainfall, LLF blows typically from South to South-East.

2. Mid Level Flow (MLF)
   A layer extending from 2.5 to 3.5 km was chosen to estimate the Mid Level Flow, which represents the wind ascending over the terrain above the Lago Maggiore region. Also MLF is typically southerly when precipitation is observed in the Lago Maggiore area.

3. Cross Barrier Flow (CBF)
   This flow is retrieved south of the Alpine crest between 3 and 4 km above sea level in the north-westerly Lago Maggiore area, in a region where the wind is typically observed to change direction (from southerly to northerly) in correspondence with frontal passages.

4. Upper Level Flow (ULF)
   This flow is estimated between 4 and 5 km in a wide ring around the radar site and it represents the upper level synoptic flow. During orographic precipitation the wind in this region blows usually from South to South-West.
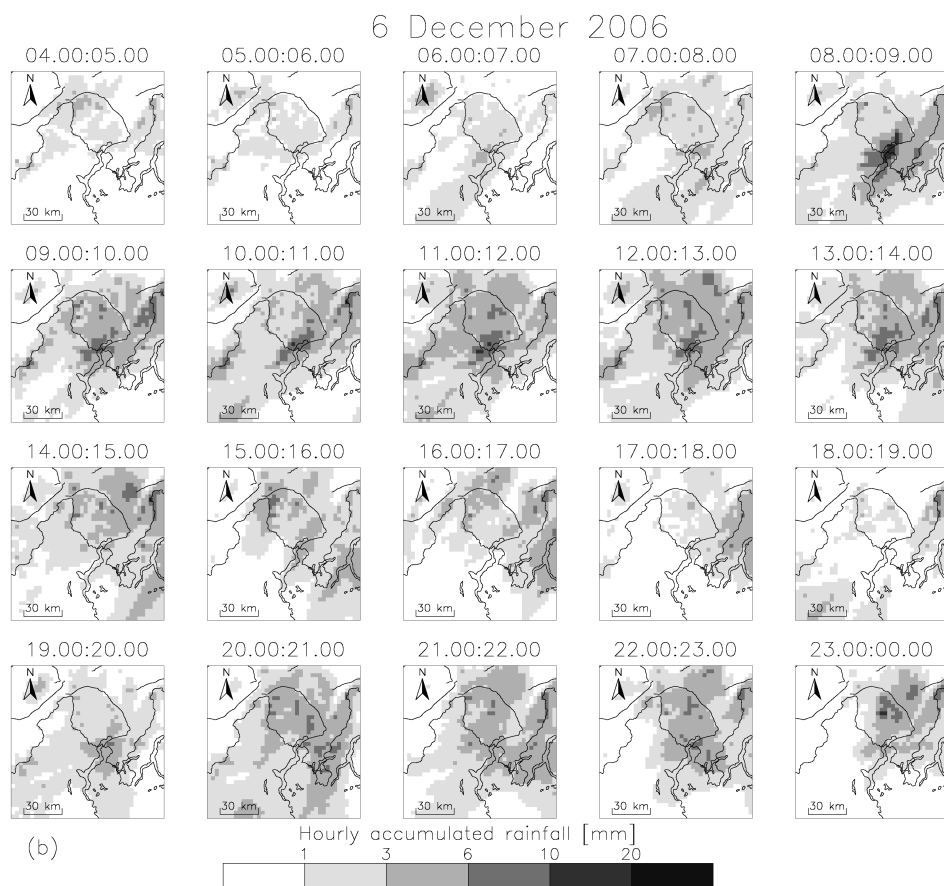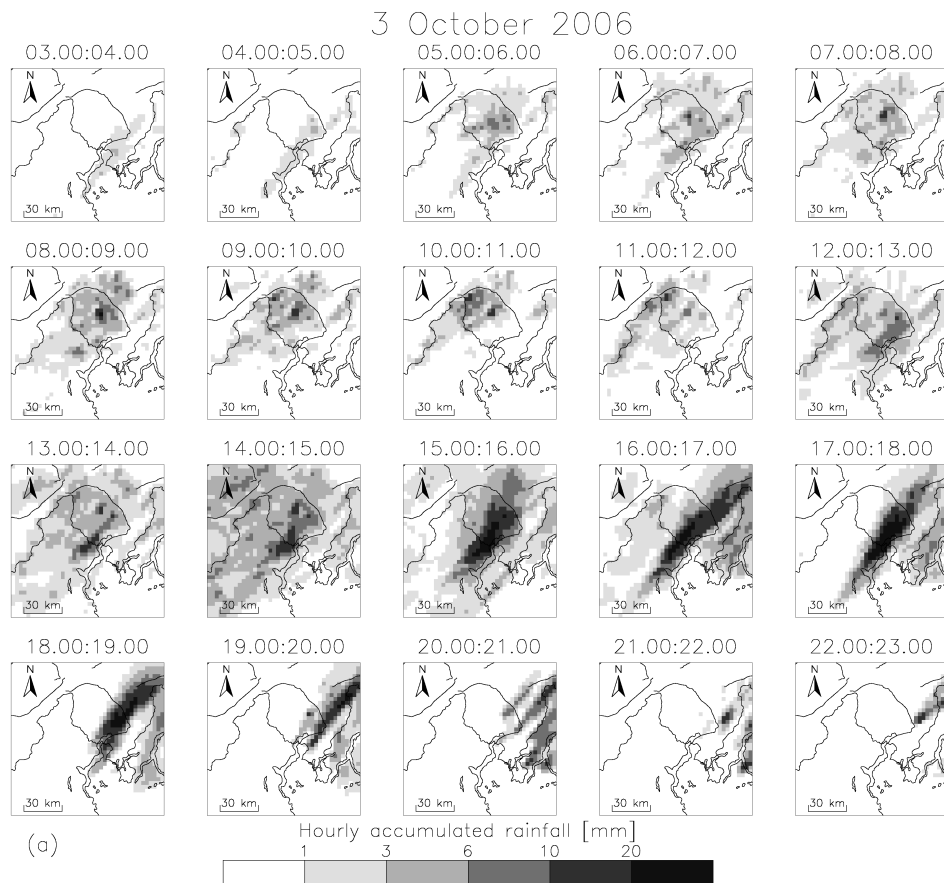
Figure 3.3: *Sequence of radar images representing hourly accumulated rainfall for two precipitation events. The spatial domain is the same as for the bottom panel of figure 3.1. Panel (a): 3 October 2006 from 03 to 23 UTC. Panel (b): 6 December 2006 from 04 to 24 UTC.*
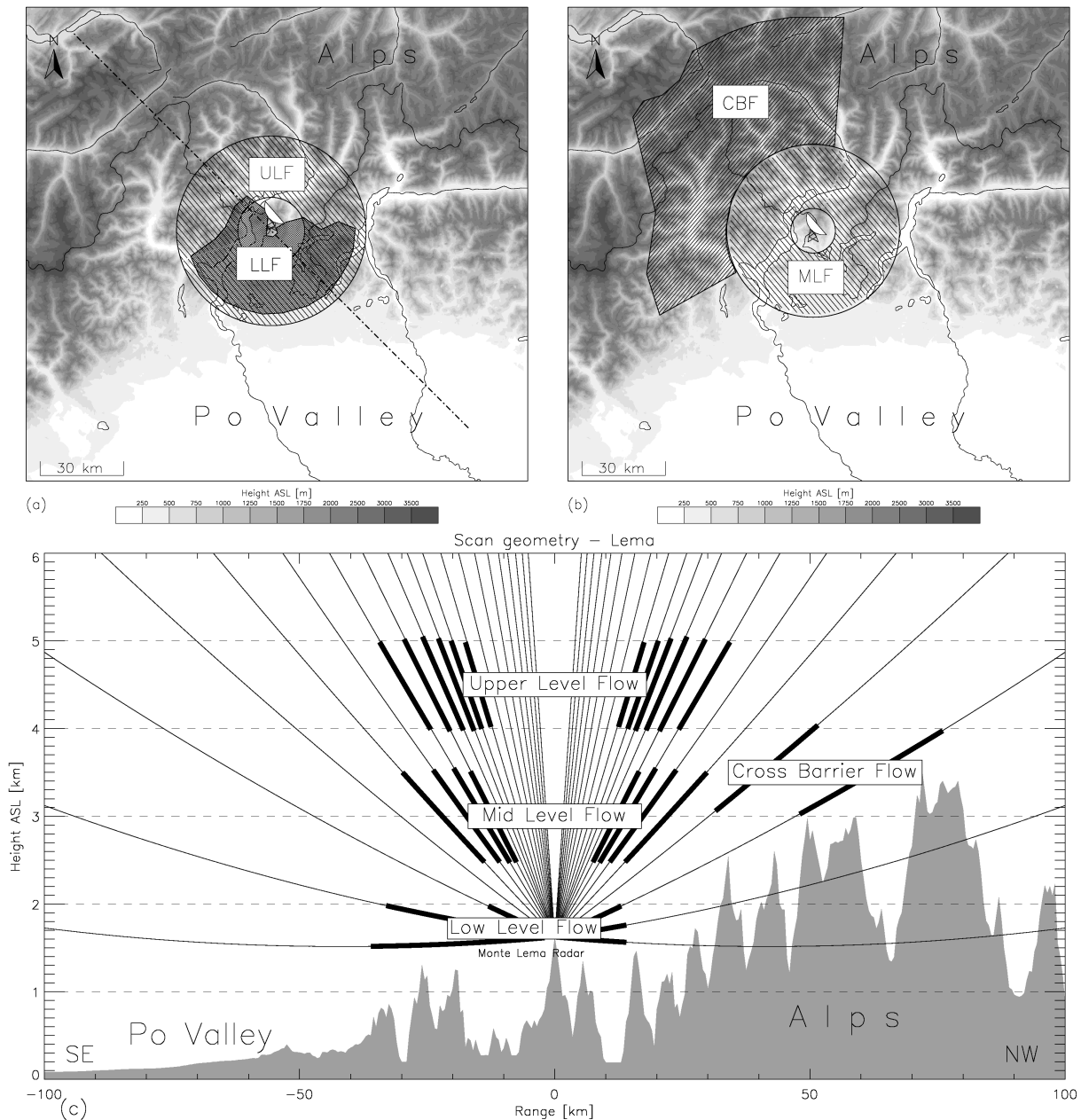
Figure 3.4: *Location of the four regions in which the mesoscale flows are estimated by means of Doppler velocity radar measurements. (a) Horizontal extension of Low Level Flow (LLF) and Upper Level Flow (ULF); (b) Horizontal extension of Mid Level Flow (MLF) and Cross Barrier Flow (CBF); (c) Vertical cross section performed along the dotted line in panel (a) showing the 20 elevation angles of the Monte Lema radar scan strategy (thin lines) and the regions selected for the flow estimates (thick lines).*

A rationale for the choice of the regions in which these flows are estimated is given in section 5 of PG10, while in section 2.4 of the same paper the methodology by which these winds are estimated from radar Doppler measurements is described.

58

Air mass stability

The moist Brunt-Väisälä frequency derived from Stabio and Monte Generoso ground stations is also taken as a predictor of orographic rainfall by NORA. Section 3.2 of PG10 gives a motivation for the choice of this quantity, which is calculated following equation (36) of Durran and Klemp (1982).

WAR and IMF

Wet Area Ratio (WAR) and Image Mean Flux (IMF) are also used as predictors by NORA. WAR is defined as the fraction of wet area in the radar image, whereas IMF is the average rainfall of the image (e.g., Pegram and Clothier, 2001). Both these quantities are estimated only within the Lago Maggiore catchment (see bottom panel of figure 3.1). The threshold used for the calculation of WAR is 0.16 mm/h. The aim of using also WAR and IMF as predictors of orographic rainfall is the identification in the past of situations similar also in extension (WAR) and amount (IMF) of precipitation. In addition to WAR and IMF at the time of the forecast, their variation in the preceeding two hours is also taken as predictor. To a certain extent, WAR and IMF take into account the moisture content of the atmosphere within the radar domain.

3.3.6 Analogues

The historical situations most similar to the current one, i.e. the analogues, are identified through a two-step process. First, 120 analogues from the predictors which describe the orographic forcing are obtained (*forcing analogues*); second, 12 analogues are selected from the first ones by considering radar rainfall features (*final analogues*). As reported by Obled et al. (2002), the number of analogues taken into account results from a trade-off: the more analogues we select, the better the sampling, but the less the subset is conditioned by the current situation, because of the decreasing analogy. The optimal numbers 120 and 12 were obtained by evaluating the performance of the NORA algorithm achieved with different combinations of the number of forcing and final analogs in terms of bias, scatter, and mean absolute error (these scores will be introduced in section 3.4.1). The numbers proposed gave the best results with the current historical archive, but they might change when working with other data sets. For example, looking for analogues in a database much larger than the one we use, 12 members may not be enough to represent the uncertainty of the forecast. Moreover, end users can ask for forecasts with particular properties, such as high probabilities of detection rather than low false alarm rates. The number of the analogues, thus, depends also on the application for which the forecasts are made.

Forcing analogues

In the first step mesoscale flows and air mass stability are used to determine the analogues in the historical archive. The analogue model employed by NORA makes use of the euclidean distance computed in a multi-dimensional space (e.g., Benestad et al., 2008). Zonal and meridional components of the mesoscale flows, together with air mass stability, are the coordinates of this space. The euclidean distance between the current situation and each sample of the historical archive is calculated, assuming that the past conditions with the smallest distances are the most similar to the current situation. Since the performance of the wind estimation algorithm depends on the features of the wind field itself (see section 2.4 of PG10), it is not always possible to estimate all four mesoscale winds every 5 minutes. Therefore, the number of dimensions of the space in which the analogues are searched may change, depending on the number of the available mesoscale flows. If the estimate of all the four mesoscale winds fails, the NORA forecast is not produced. If only one wind can be calculated, the predictors used to find the forcing analogues are three: moist static stability, zonal and meridional component of the

flow. In the best case, the zonal and meridional components of the four flows, together with air mass stability, lead to a 9-dimensional phase space in which analogues are searched. We made experiments replacing the euclidean by the Mahalanobis distance (e.g., Webster and Oliver, 1990), which takes into account the correlation between the predictors. As the results were not significantly different, we opted for the simpler euclidean solution. We also evaluated the skill of NORA by taking different combinations of mesoscale winds, following the methodology proposed by Obled et al. (2002). Again, the performance of the system did not significantly change. It could thus be argued that it is not necessary to estimate four mesoscale flows, since they are correlated. However, the number of samples is substantially reduced if we do not take all the available wind estimates, which is a serious problem in an operational context. Searching for analogues without considering air mass stability, on the other hand, resulted in a great worsening of the skill of NORA.

In the calculation of the euclidean distance, the scales of measurement are standardized in order to give equal weight to all predictors: the values of each predictor are divided by the standard deviation of that predictor in the whole historical archive.

In this first step the 120 samples (corresponding to 10 hours of rainfall) most similar to the current situation by the point of view of the orographic forcing are extracted from the historical archive.

Final analogues

The second step of the process by which NORA searches for the analogues is aimed to identify the forcing analogues with the rainfall patterns most similar to the current one. In fact, situations characterised by similar mesoscale flows and air mass stability, may still be different in terms of extension and amount of rainfall over the territory. In this step, therefore, WAR, IMF and their variation in the previous two hours are the coordinates of the space in which the euclidean distance between the current radar image and each one of the 120 meteorological analogues is calculated. The 12 samples which have the smallest euclidean distances are assumed to be the situations most similar in rainfall pattern, and are the final analogues taken into account by NORA.

3.3.7   The method of forecast

The process by which NORA forecasts are produced is schematically represented in figure 3.5, where 1-hour forecasts with 2 hours lead time are generated. The current radar image is represented at the top of figure 3.5, the 120 forcing analogues are below it. Final analogues are marked in the forcing analogues by the thick black contours and reported in the left column. As it is seen in the figure, final analogues only indicate the past instances which are most similar to the current one, and they are not directly used to make the quantitative precipitation forecast. In fact, the past rainfall fields observed every 5 minutes after the analogues, according to the required lead time and temporal period, are the ones used to produce the forecast. By averaging these fields, 12 ensemble members, one for each analogue, are obtained. In the example given by figure 3.5, the rainfall fields observed in the past every 5 minutes from 2 to 3 hours after the analogues are used to produce the final forecast. If the rainfall fields observed after the analogue and necessary to produce the forecasts are not available because the analogue is too close to the current instant, the average of the rainfall measured from the analogue to the current instant is taken as the corresponding ensemble member. Since the current radar image is one of the final analogues by construction, it is always one of the 12 ensemble members, independently on the lead time of the forecast.

NORA is capable of producing both deterministic and probabilistic forecasts. Deterministic predictions are obtained simply by averaging the ensemble members. Probabilities of exceeding particular rain rate thresholds are based on the probability density function derived from the 12 ensemble members.
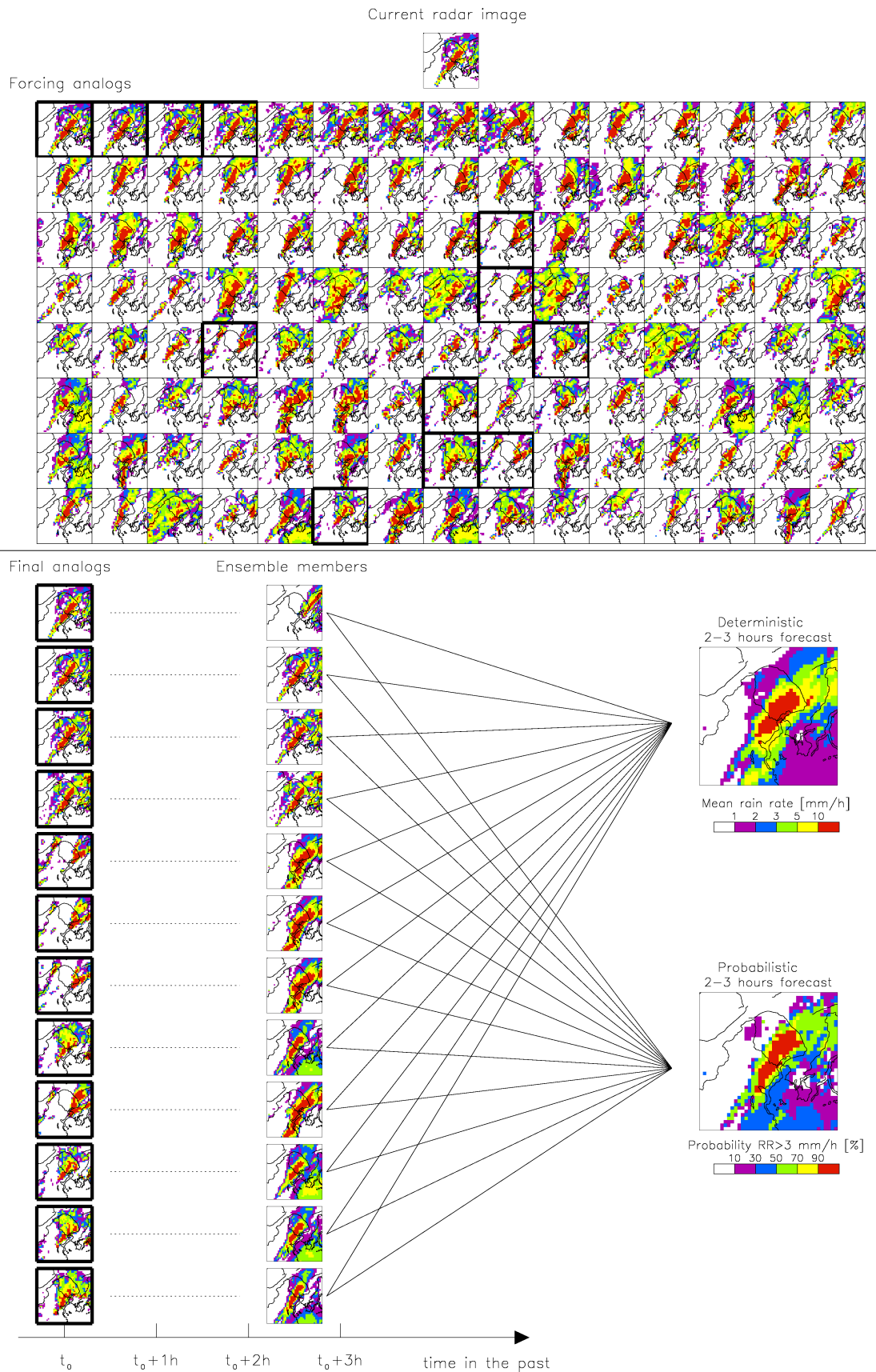
Figure 3.5: *The analogue process by which NORA forecasts are created. The time at which the forecast was issued is 16:55 UTC of 3 October 2006. See text for explanation.*

3.4 NORA forecast verification

In this section NORA forecasts are compared with radar observations, Eulerian persistence and COSMO2 predictions. In particular, we want to answer the following questions:

1. What is the skill of NORA in forecasting orographic precipitation, compared to that of Eulerian persistence?

2. What is the skill of NORA in forecasting orographic precipitation, compared to that of a state of the art limited area numerical model?

3. What is the skill of NORA in producing both deterministic and probabilistic forecasts?

4. What is the overall bias of NORA forecasts with respect to observations?

5. How much does the agreement between NORA forecasts and observations vary within the verification sample?

6. How good is the NORA prediction of both wet and dry areas and of the precipitation amounts in wet areas?

The precipitation derived by the radar is assumed to be the ground truth in the evaluation of NORA, Eulerian persistence and COSMO2 forecasts. We realize that radar estimates are corrupted with errors from various sources (e.g., Germann et al., 2006). Including the effects of quantitative precipitation estimation errors into NORA is not within the scope of this paper.

As already mentioned in section 3.3.6, only if at least one mesoscale flow estimate is available, the NORA forecast is made; this occurred for 88% of the total time of the historical archive, which corresponds to a total of 32126 5-minute samples (2677 hours, 111.5 days). NORA forecasts were thus produced for each of these past samples, and compared with the observed rainfall field and with the Eulerian persistence forecast. The comparison with COSMO2 was performed for a subset of the archive, as reported in section 3.4.6. In order to evaluate the skill of NORA in real-time mode, the 24 hours following the sample for which the forecast was made were excluded from the historical archive in which the analogues are searched. The results of the verification of a subset of the archive performed in this way and looking for the analogues only in the past were not significantly different. For computational reasons the original spatial resolution of the precipitation field was reduced to 9 square km by aggregating 9 pixels of 1 square km. Thus both NORA and Eulerian persistence forecasts, as well as observations, were treated with this spatial resolution. NORA forecasts were verified within the Lago Maggiore catchment, which is 7830 square kilometers large (see figure 3.1). The temporal resolution of the verification data set is 5 minutes, for a total of 32126 samples.

Section 3.4.1 defines the quality parameters which are used to evaluate the forecasts. Section 3.4.2 gives details about the Eulerian persistence, which is taken as a reference forecasting method. Section 3.4.3 and 3.4.4 presents the results of the verification of non-probabilistic and probabilistic forecasts respectively. Section 3.4.5 evaluates the performance of NORA and Eulerian persistence for each event individually. Section 3.4.6 compares the performance of NORA with that of COSMO2 numerical model.

3.4.1 Definition of quality parameters

To assess the quality of both NORA and Eulerian persistence forecasts, and to answer the above questions, the following quality parameters are used.

1. Bias. It is defined as the total of the predicted precipitation amounts divided by the total of precipitation amounts observed by radar. Since it is given in dB, a bias larger than 0 indicates that the forecast overestimates the observations, while a bias smaller than 0 denotes underestimation.

2. Mean Absolute Error (MAE). It is the mean of the absolute values of the individual forecast errors, given in mm/h.

3. Scatter. It is defined as half the distance between the 16th and 84th percentiles of the error distribution, which is the cumulative contribution to the total rainfall as a function of the prediction-observation ratio. It is given in dB. For details see Germann et al. (2006).

4. Probability of detection (POD). It describes the ability of the forecasting system to predict precipitation larger than a given threshold. If the occurrence is always (never) forecast POD is equal to 1 (0).

5. False alarm ratio (FAR). It indicates the proportion of forecasts of rainfall larger than a given threshold that actually did not occurr. FAR of 0 (1) indicates that forecasts were always (never) followed by occurrence.

6. Critical success index (CSI). It describes the ability of the forecasting system to have high POD and, at the same time, low FAR. Perfect skill gives a CSI with the maximum value of 1, while CSI of 0 results if there are no hits.

7. Equitable threat score (ETS). It describes the skill of the forecasting system to have high POD and low FAR over a random or constant predictor. Perfect forecasts have ETS equal to 1, random or constant forecasts equal to 0.

8. Brier Score (BS). It describes the skill of the forecasting system to predict probabilities of exceeding rain rate thresholds. A minimum Brier score of 0 is obtained for a perfect system which issues probability forecasts of 1 (0) every time before the event is (not) observed to occurr. A Brier score of 1 means systematically erroneous forecasts. To compare the skill of two different forecasting systems, whose one is taken as the reference, the Brier Skill Score (BSS) is used. Positive (negative) values of BSS indicate that the forecasting system is better (worse) than the reference forecasting method.

For a definition of Bias, MAE, POD, FAR, CSI, ETS and BSS see Joliffe and Stephenson (2003) and Wilks (1995). These verification scores are averaged over the space-time window of the entire verification data set, which consists of $2.5 \cdot 10^7$ samples (870 pixels for 32126 times). The POD, FAR, CSI, ETS and BSS are calculated for two thresholds: 0.5 mm/h and 3 mm/h. They were chosen in order to describe the ability of the forecasting system to predict the occurrence of rainfall (rain rate larger than 0.5 mm/h) and of moderate to strong rainfall (rain rate larger than 3 mm/h). Bias, MAE and scatter, on the other hand, describe the ability of the forecasting system to predict the correct amount of precipitation. While bias quantifies the overall agreement between forecasts and observations averaged over the whole space-time sample, scatter describes the variability of the agreement within the sample. In particular, scatter is derived from the samples characterized by both predicted and observed precipitation larger than 0.5 mm/h, thus evaluating the prediction of precipitation amounts only among the hits in wet areas; it is not affected by false alarms, missed events and correct negatives. Since most of the sources of error in radar precipitation estimates are of the multiplicative type, bias and scatter are expressed in dB. For a more detailed discussion of scatter, see section 4 of Germann et al. (2006). Brier Skill Score, which is also calculated for the two rain rate thresholds of 0.5 and 3 mm/h, describes the ability of the forecasting system to produce percentage probabilities of exceeding such thresholds.

3.4.2 The reference forecasting method

Eulerian persistence is taken as the reference forecasting method in the evaluation of NORA forecasts. As described in section 3.1.2, this method simply consists in taking the last radar image as forecast. In particular, we followed the approach denoted by Germann and Zawadzki (2004) as Local Eulerian persistence: the forecast for a specific pixel results from the rainfall measured in that pixel and in the surrounding pixels. The average of the rainfall values measured in these pixels is computed to get deterministic forecasts, whereas their probability density function leads to probabilistic predictions. The forecast is assigned only to the central pixel, thus preserving the original spatial resolution of the precipitation field. The number of surrounding pixels considered by the Local Eulerian approach determines the grade of spatial smoothing of the original rainfall field. By aggregating a number of past radar images, a further smoothing of the last rainfall field can be obtained.
We computed Local Eulerian persistence forecasts for different spatial and temporal aggregations of pixels, thus producing a large number of Eulerian persistence forecasts. In this paper NORA forecasts are compared with the Local eulerian persistence forecasts obtained by aggregating in space over a 9 x 9 square kilometers moving mask, without aggregation in time. In fact, this spatio-temporal scale provides overall best performances.

3.4.3 Non-probabilistic forecasts

In this section non-probabilistic forecasts are evaluated; in the first part we present the joint and marginal distributions of forecasts and observations. Then, the performance of the two forecasting systems is evaluated by presenting a number of skill scores.

Basic distributions and summary measures

Table 3.1 represents the joint distibution of 1-hour NORA forecasts with zero lead time and corresponding radar observations. The aim of such matrix is to provide an overall view into the relation between forecasts and observations. In table 3.1 it is seen that at low and moderate rain rates the largest joint relative frequencies are observed when forecasts and observations belong to the same category. Furthermore, the joint distribution appears to be generally symmetric about the diagonal. However, the overall accuracy of NORA, as derived from the diagonal elements of table 3.1, is only of 53%. This is due to the presence of non-zero elements out of the diagonal.
Marginal distribution of observation (forecast) is reported in the next to last row (column) of table 3.1. Normalizing the off-diagonal elements of the matrix with the sum of the elements of each class, exclusion and inclusion errors are obtained (last row and column of the matrix). Exclusion errors express the probability of forecasting rainfall in the wrong category given the rain rate category which has been actually observed. Inclusion errors express the probability of making a mistake when forecasting a given category. From table 3.1 it can be argued that the forecast of large rain rates are particularly critical for NORA in terms of both exclusion and inclusion errors. For high rain rate inclusion errors are large; exclusion errors are even larger. The difficulties of predicting large rain rates come from the analogue approach of NORA. Since such rain rates are observed in the case of heavy rainfall events with large return periods, in a 6-year data set it is unlikely to find these events (e.g. Obled et al., 2002).
Marginal distributions of forecast and observation relative to lead times ranging from 0 to 7 hours are characterized in terms of mean and standard deviation in table 3.2. Mean values of both NORA and Eulerian persistence are larger than the observed ones for lead times larger than 2 hours. Moreover, mean and standard deviation decrease with increasing lead time. This is due to the fact that by increasing lead time of the forecasts and corresponding radar observations, the sample includes more and more zeros or small rainfall values, as we are moving out of the precipitation events. Standard deviation of NORA is smaller than observation and persistence for all lead times, since it comes from

the average of the 12 ensemble members.

Performance measures

The performances of both NORA and local Eulerian persistence are described by figure 3.6. Again, both NORA and Eulerian persistence forecasts are compared with radar observations. 1-hour NORA forecasts were produced for different lead times, ranging from 0 to 7 hours. Persistence forecasts, on the other hand, do not vary with the lead time, since this technique assumes the current radar image as forecast.
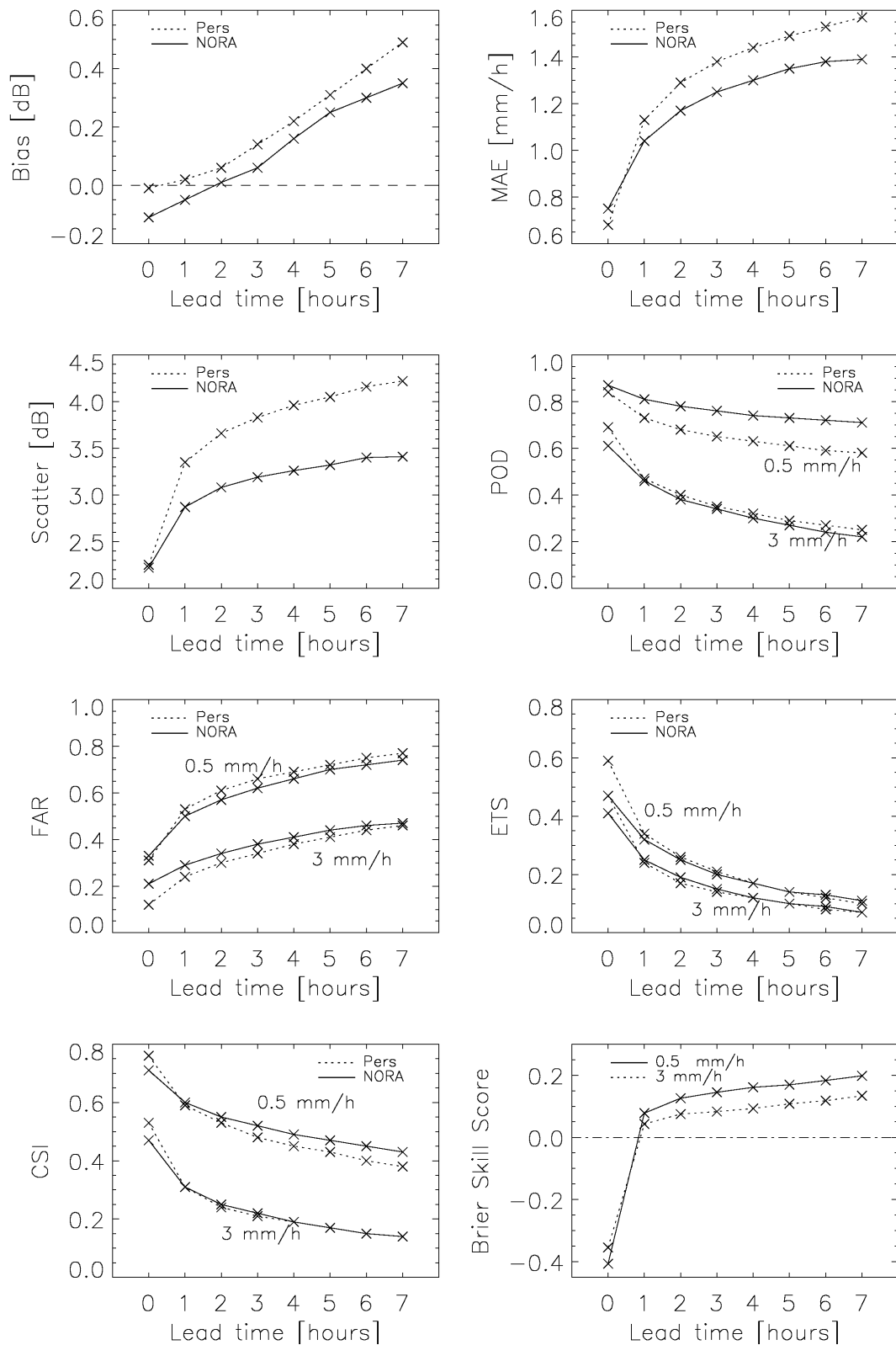
As seen in figure 3.6, Eulerian persistence forecasts skill is similar to that of NORA for forecasts with zero lead time. For larger lead times, however, NORA generally outperforms Eulerian persistence, even if the accuracy of the forecasts decreases with increasing lead time. As seen in panel (a), NORA tends to underestimate rainfall amounts for zero and one hour lead time forecasts, whereas for larger lead times it leads to an overestimation, which is however smaller than that produced by Eulerian persistence. The reason for which the bias of NORA grows with increasing lead time is probably the same of the decrease of mean and standard deviation of NORA observed in table 3.2: as the lead time increases, the observation sample includes more and more zeros or small rainfall value as we are moving out of the precipitation events. The average of the absolute differences between forecasts and observations (MAE, panel (b)), as well as the variability of the forecast-observation ratios (scatter, panel (c)), are significantly smaller for NORA than for Eulerian persistence for lead times larger than 1 hour. Panels (d), (e), (f) and (g) of figure 3.6 show the results of the verification of binary forecasts, namely the occurrence of rainfall (rain rate larger than 0.5 mm/h) and of moderate to strong rainfall (rain rate larger than 3 mm/h). For zero lead time Eulerian persistence performs better than NORA, whereas for larger lead times NORA generally outperforms Eulerian persistence for the 0.5 mm/h threshold. Binary NORA forecasts of exceeding 3 mm/h, however, do not constitute an improvement with respect to persistence predictions. This difficulty of NORA in correctly forecasting high rainfall intensities was observed also in table 3.1.

Forecast verification was also performed for predictions of rainfall accumulated in temporal periods ranging from 1 to 8 hours with lead time constant at zero. Also in this case NORA generally beats Eulerian persistence forecasts after the first hour.

3.4.4   Probabilistic forecasts

In this section NORA probabilistic forecasts are compared with Eulerian persistence probabilistic forecasts. The latter were obtained by calculating the probability of rainfall exceeding a particular threshold in a square area centred on the considered pixel, as reported in section 3.4.2. The skill of NORA and Eulerian persistence probabilistic forecasts is characterized in terms of Brier Skill Score for 1-hour forecasts with lead time ranging from 0 to 7 hours in panel h) of figure 3.6. In the computation of the Brier Skill Score, Eulerian persistence is taken as the reference forecasting method. Also in this case the rain rate thresholds are 0.5 and 3 mm/h. Panel h) of figure 3.6 shows that probabilistic NORA forecasts constitute an improvement with respect to Eulerian persistence forecasts for lead times larger than zero (positive values of the Brier Skill score). Moreover, the skill of NORA, compared to that of Eulerian persistence, gets larger with increasing lead time.

The Brier Score can be decomposed into three terms: reliability, resolution and uncertainty (Wilks, 1995). The reliability term describes the ability of the system to forecast correct probabilities compared to observed frequencies. It is negatively oriented, being zero for perfectly calibrated forecasts. The resolution term (positively oriented) is a measure for the ability of forecasts to separate the according observations in categories of different relative frequencies. The uncertainty term does not depend on the forecasting system and describes the variance of the observations. Table 3.3 presents the values of the Brier Score and its reliability and resolution components for 1 hour forecasts with 0, 3 and 7

Figure 3.6: *Skill scores for 1-hour forecasts with lead times ranging from 0 to 7 hours for both NORA and Eulerian persistence forecasts. All scores describe the evaluation of deterministic forecast, except Brier Skill Score (panel h). The latter is relative to the verification of probabilistic forecasts, and the reference forecasting method considered in its computation is Eulerian persistence.*

hours lead times. The reference probability of precipitation is given by the verification data set, which is thus considered as the climatology. For both rain rate threshold of 0.5 and 3 mm/h, it can be seen in table 3.3 that NORA forecasts are both more reliable and resoluted than persistence forecasts for lead times larger than zero. For forecasts of rainfall with zero lead time, however, persistence performs better than NORA, even though NORA is more reliable than persistence for forecasts of exceeding 0.5 mm/h.

Table 3.1: *Contingency table (percentage frequencies) of the joint distribution of 1-hour NORA forecasts with zero lead time and corresponding radar observations. The next to last row (column) of the table represents the marginal distribution of forecasts (observations); the last row (column) the exclusion (inclusion) errors for each class, also given as percentages.*

	mm/h	0.1	1	2.5	4	6.3	10	25		inc.err.
F	0.1	**19.920**	3.652	0.423	0.079	0.037	0.019	0.012	0.001	24.143	17
o	1	12.631	**16.962**	5.141	0.817	0.284	0.107	0.059	0.004	36.006	53
r	2.5	1.815	6.150	**10.438**	3.254	1.015	0.258	0.099	0.006	23.035	55
e	4	0.291	0.830	2.880	**3.287**	1.776	0.405	0.105	0.006	9.580	66
c	6.3	0.097	0.219	0.673	1.294	**1.844**	0.774	0.168	0.008	5.076	64
a	10	0.024	0.048	0.118	0.201	0.470	**0.573**	0.225	0.010	1.669	66
s	25	0.006	0.011	0.022	0.032	0.067	0.126	**0.180**	0.024	0.468	61
t		0.000	0.000	0.000	0.001	0.001	0.002	0.010	**0.007**	0.023	68
		34.784	27.873	19.697	8.964	5.494	2.263	0.859	0.066	100	
	exc.err.	43	39	47	63	66	75	79	89		

The column header "O b s e r v a t i o n" spans the observation columns.
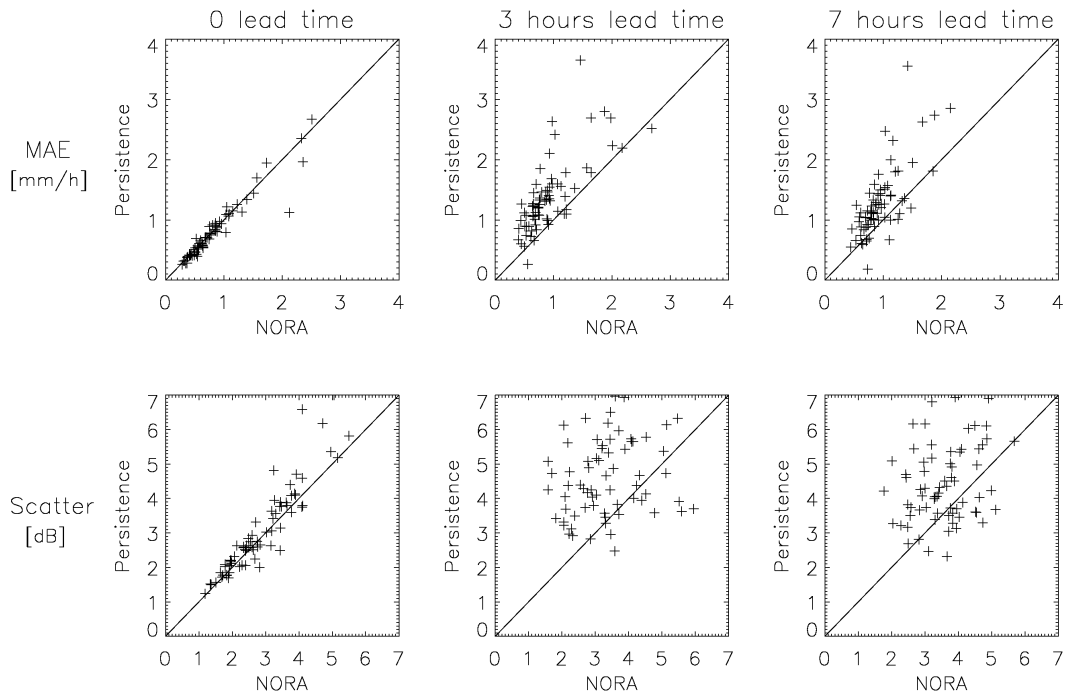
Figure 3.7: *Mean Absolute Error and Scatter of forecasts with different lead times for the 71 precipitation events of the historical archive.*

Table 3.2: *Mean and standard deviation of NORA, Eulerian Persistence and observation marginal distributions.*

	Mean [mm/h]	Std.Dev. [mm/h]
0-1 h		
Obs.	1.33	2.24
NORA	1.31	1.84
1-2 h		
Obs.	1.32	2.24
NORA	1.32	1.82
2-3 h		
Obs.	1.30	2.23
NORA	1.32	1.79
3-4 h		
Obs.	1.28	2.20
NORA	1.31	1.75
4-5 h		
Obs.	1.26	2.18
NORA	1.31	1.73
5-6 h		
Obs.	1.23	2.15
NORA	1.31	1.71
6-7 h		
Obs.	1.21	2.13
NORA	1.30	1.68
7-8 h		
Obs.	1.18	2.11
NORA	1.29	1.67
Eul.Pers.	1.32	2.44

Table 3.3: *Brier Score (BS) and its reliability and resolution components for NORA and Eulerian Persistence forecasts.*

	0.5 mm/h			3 mm/h		
	BS	Rel.	Res.	BS	Rel.	Res.
0-1 h						
NORA	0.142	0.001	0.113	0.088	0.006	0.034
Pers	0.101	0.007	0.153	0.065	0.003	0.057
3-4 h						
NORA	0.242	0.042	0.038	0.132	0.024	0.008
Pers	0.283	0.073	0.035	0.144	0.040	0.009
7-8 h						
NORA	0.283	0.068	0.015	0.142	0.035	0.002
Pers	0.353	0.123	0.010	0.164	0.060	0.002

3.4.5 Single events verification

In this section the skill of NORA and Eulerian persistence is evaluated for the precipitation events of the historical archive individually. Figure 3.7 presents the values of MAE and scatter of 1-hour forecasts with 0, 3 and 7 hours lead time for each precipitation event: the points lying above the

diagonal represent events for which NORA is better than persistence. As it can be seen in the figure, NORA tends to be better than persistence for the majority of the events. Only for forecasts with zero lead time it is difficult to state which method is better, as confirmed also by the skill scores of figure 3.6. It is not surprising to note that the skill of NORA can vary a lot from one event to another, as the overall performance of NORA depends on many factors. The quality of flow estimation from Doppler velocity data depends on the extension of precipitation in the pre-defined area (see section 2.4 of PG10). The occurrence in the past of events similar to the one to be forecast can also influence the skill of NORA; the similarity has to be interpreted not only in terms of wind field and air mass stability, but also in terms of rainfall patterns.

We now proceed to characterize the rainfall spatial pattern of each event in terms of correlation distance, which is defined as the distance at which the correlation between pixels drops to $1/e$. Correlation distance is one way to characterize the spatial structure of the precipitation field. The theory behind this approach (second-order stationarity and isotropy) is not strictly valid for the rainfall fields over our region of study. However, this analysis is performed only to provide first indication of the predictability of NORA with respect to the spatial pattern of each event.

The estimation of the spatial correlation has been performed with the widely used Pearson's product-moment estimator (e.g. Pearson, 1920; Rodgers and Nicewander, 1988; Hutchinson, 1997). Figure 3.8 shows the values of the correlation distance of each precipitation event in relation to MAE, bias and scatter of NORA forecasts of hourly accumulated rainfall with 3 hours lead time. The events for which NORA performs better than Eulerian persistence are also indicated (crosses). It can be seen from figure 3.8 that NORA forecasts tend to be better for precipitation events characterized by large correlation distances. Moreover, the few events for which persistence performs better than NORA have small correlation distances. One of the reasons for the better performance of NORA for large correlation distance rainfall fields is that the orographic forcing, which is the core of NORA, is expected to be more efficient with more organized and spatially extended precipitation patterns. In addition, the mesoscale flow estimation algorithm works better in such scenario.

3.4.6 Comparison with COSMO2

In this section the skill of NORA is compared with that of the limited area numerical model COSMO2, which is used operationally at MeteoSwiss and in other four european national weather services (e.g. Steppeler et al., 2003). Assimilation into the model of radar rainfall observations is performed with a latent heat nudging scheme: at each time step the latent heating of the model is corrected by a factor derived from the ratio of observed and model-estimated surface precipitation. The introduced change in buoyancy causes an enhancement or dampening of the vertical velocity and the associated cloud and precipitation processes (e.g. Leuenberger and Rossa, 2007). The comparison between NORA and COSMO2 was performed for a subset of our archive, given by the precipitation events occurred after 25 May 2007. Within this subset, the 5-minutes samples which have a NORA forecast, and which are therefore here evaluated, are 14535, corresponding in total to about 50 days of precipitation. The 2.2 km original spatial resolution of the model was reduced to 3 km. The COSMO2 forecasts considered at each time step are the latest that would have been available in real-time, considering that the data are delivered to the users after 2 hours (because of assimilation, computation and dissemination time). As in the verification already presented, hourly rainfall accumulations with different lead times are evaluated for the Lago Maggiore region, taking the radar observations as the truth. Figure 3.9(a) shows that COSMO2 suffers from a negative bias, whereas NORA has a slight negative bias in the first hours of forecast which tends to increase with increasing lead time. In terms of mean absolute error, as it appears from panel (b), NORA performs better than COSMO2 for forecasts with lead times up to 4 hours. In terms of scatter the numerical model is worse than NORA for all the considered lead times (panel (c)). The results of binary verification (panels (d), (e) and (f)), strongly depend on the considered threshold. For light rainfall (rain rate larger than 0.5 mm/h) NORA performs better than COSMO2 only for forecasts with 1-2 hours lead times, whereas for moderate rainfall (rain rate
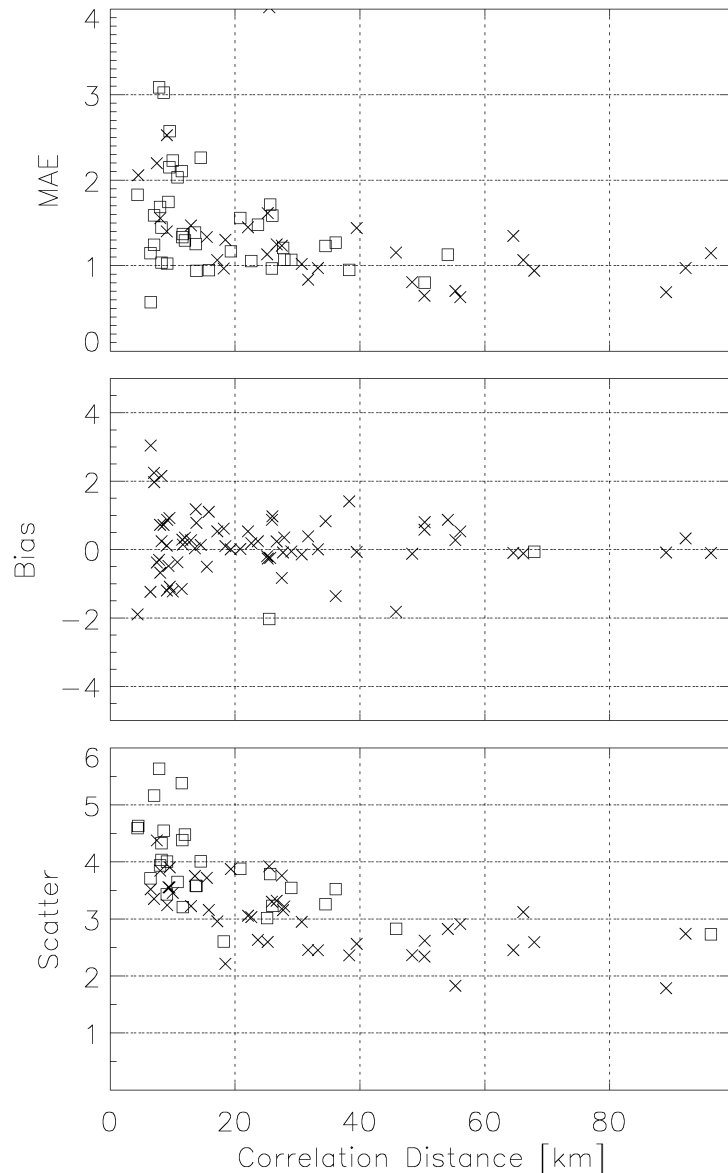
Figure 3.8: *Performance measures of 1-hour NORA forecasts with 3 hours lead time as a function of the correlation distance of the 71 precipitation events. Crosses denotes the events for which NORA perform better than Eulerian persistence, squares the events for which the skill of Eulerian persistence is higher than that of NORA.*

larger than 3 mm/h) NORA is better than COSMO2 for forecasts with lead time up to 3-4 hours lead time. It could be argued that the better performance of NORA with respect to COSMO2 is due to the fact that NORA forecasts are derived from radar archive, whereas the numerical model output gives only a little weight to the radar image through the latent heat nudging. However, the results shown in figure 3.9 denote a discrepancy between COSMO2 and NORA forecasts which is unlikely to be caused only by the dependence of NORA forecasts on the radar archive. This is further confirmed by the visual comparison between COSMO2, NORA forecasts and radar observations fields: the low performance of the numerical model is due to problems in forecasting the location and the amplitude of the rainfall.
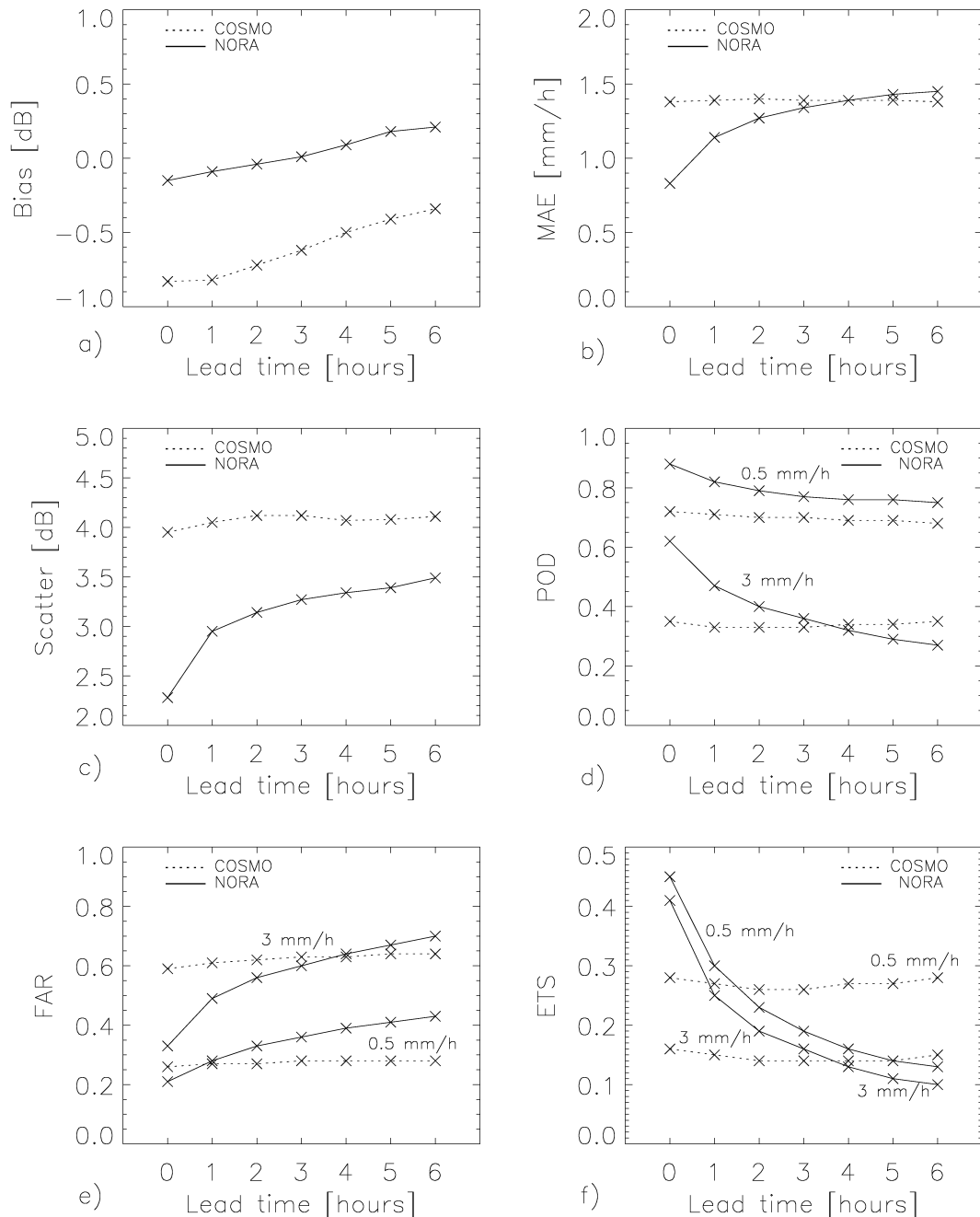
Figure 3.9: *Skill scores for 1-hour forecasts with lead times ranging from 0 to 6 hours for both NORA and COSMO2 forecasts. The verification is done for 50 days of rainfall, a data set shorter with respect to figure 3.6 (see text for details).*

3.5 Conclusions

A novel heuristic analogue-based nowcasting tool for very short-term forecasting of orographic precipitation (NORA) was presented in this article. The system was developed for the Lago Maggiore region, which is located in the southern part of the European Alps between Italy and Switzerland. The originality of the tool is that it takes large benefit from the strong orographic forcing which is observed in the area to produce very short-term precipitation forecasts. Data needed to run the tool are precipitation and Doppler velocity measured by radar, together with temperature, humidity and pressure from a pair of ground stations located at different altitudes. Radar data are used to estimate

precipitation and mesoscale flows, ground stations data serve to estimate air mass stability. Mesoscale flows, air mass stability and rainfall field features are used as predictors of orographic precipitation: they are employed to search in the past for analogues, which are the situations with the predictors most similar to the ones observed at the current time. NORA produces both deterministic and probabilistic forecasts of precipitation which are based on the rainfall fields observed in the past after the analogues. However, the sum of the rainfall already accumulated during a precipitation event and the rainfall predicted by NORA can result in an accumulation not previously observed. The historical archive in which NORA searches for the analogues is given by 127 days of significant rainfall observed in the Lago Maggiore region between 2004 and 2009. The same data set was used to evaluate the skill of the system. For this reason in the verification process the 24 hours following the time at which the forecasts were issued were removed from the archive in which the analogues were searched. The skill scores presented in the paper show that for forecasts with lead time equal or larger than 1 hour, both probabilistic and deterministic NORA forecasts are better than Eulerian persistence. This means that by looking into the past for situations with similar predictors, forecasts better than persistence can be obtained. The value of these findings is high, since the events we analyzed are widespread and long-lasting, and therefore tend to be persistent. The skill of NORA is also larger than that of the numerical model COSMO2 for the first hours of forecast. The lead time at which the two methods have the same skill is around 4 hours. The results of this paper also highlight that the analogue approach can be successful, as long as the analogies are searched at the mesoscale by making use of physical predictors that strongly relate to precipitation.

The analogue model used by NORA to produce rainfall forecasts leads to a natural methodology to create an ensemble of precipitation fields. In fact, by taking the past situations most similar to the observed one, an ensemble of forecast precipitation fields is naturally found. Since they result from precipitation observed in the past, these fields have by construction realistic statistical space-time properties, such as marginal distribution, power spectrum, intermittency, anisotropy. Moreover, they also take into account local characteristics of precipitation, such as preferred location of initiation and paths of intense rainfall cells.

The system can be developed and improved by adding new historical cases and predictors. The presence of new precipitation events, in fact, brings benefit as a larger data set in which analogues are searched means an higher probability that an event similar to that to be forecast had already been observed in the past. Adding meaningful predictors, on the other hand, should help to identify the analogues, given that the predictors have a strong relation with the orographic precipitation. Possible predictors to be added to NORA are the presence of a Low Level Jet over the Po Valley, the strength of the vertical wind shear in the low layers, the altitude of the freezing level, the moisture content of the lower troposphere derived, for example, from GPS.

The development of NORA in mountainous regions other than the Lago Maggiore area is possible, given the availability of good quality radar and ground stations data, and the presence of a strong orographic forcing. However, the skill of NORA in other regions can vary depending on the efficiency of the orographic forcing itself, which ultimately depends on the shape of the orography and on the repeatability of the mesoscale flows leading to precipitation. For this reason the implementation of NORA in new regions requires a previous study of the orographic forcing and of the main mesoscale features occurring during orographic precipitation. Only this kind of investigation can give an indication about the skill of NORA in new regions.

Finally, the analogue method presented in this paper for nowcasting rainfall could be employed also for the prediction of quantities other than orographic precipitation. In fact, the way by which the presence of the orographic forcing is exploited for nowcasting by NORA could also be applied to other types of forcing, such as land-sea interaction or diurnal forcing. The only assertion which needs to be demonstrated is that the forcing gives repeatability to the meteorological quantities to be predicted. The analogue forecasting method, in fact, shows that repeatability can be exploited to obtain predictability.

Chapter 4

Conclusions and Outlook

4.1 Main findings of the thesis

The two papers presented in the thesis constitute an original contribution in the field of orographic precipitation, from the point of view of both science and nowcasting.
The main findings related to orographic precipitation science are the following:

1. The layers with a mean wind velocity that correlates better than others with the mean rainfall measured in the Lago Maggiore region are located around 1 km asl about 50 km upstream of the Alpine crest, and around 3 km asl above the first alpine peaks.

2. During orographic rainfall, wind intensity is the main responsible for rainfall amounts, whereas wind direction tends to regulate the spatial distibution of precipitation over the mountains.

3. Potentially unstable lower atmospheric conditions cause more precipitation over the Alps as compared to stable cases, even during long lasting and widespread precipitation events.

4. Wind speed has the largest impact in regulating precipitation intensity over the Alps as compared to Froude number, air mass stability and wind direction.

5. The orographic forcing causes a certain repeatability in the rainfall patterns observed in the mountains given certain environmental conditions

Another original element of this thesis is the method developed to estimate mesoscale flows from radar Doppler measurements (see section 1.7.2): the wind can be estimated at different heights and in each part of the volume scanned by the radar. The resulting vector represents the wind over the region in which Doppler measurements are taken.

In the field of nowcasting orographic precipitation, this thesis shows that:

1. The repeatability of the rainfall patterns can be exploited to obtain predictability through the presence of the orographic forcing.

2. The meteorological past situations most similar to the current one can be identified through the use of significant predictors.

3. The rainfall observed in the past after the most similar situations can be used to obtain forecasts of orographic precipitation. Such forecasts are better than those given by Eulerian persistence for lead time larger than one hour, and better than those of COSMO2 for lead times smaller than 5 hours.

4. The analog method provides a natural way to incorporate into the forecast evolution of precipitation, which is not accounted for by simple Eulerian and Lagrangian persistence.

5. The uncertainty of the forecast can be easily taken into account by creating an ensemble of possible realizations, deriving simply from the natural variability of the precipitation patterns observed with similar predictors.

A radar-based heuristic tool for nowcasting orographic precipitation (NORA - Nowcasting of Orographic Rainfall by means of Analogs) was developed. The system is based on the findings illustrated in the previous sections. A prototype version has been implemented in the Swiss data processing chain and is generating in real-time nowcasting of rainfall over the Lago Maggiore area. In the context of the project IMPRINTS (*www.imprints-fp7.eu*), the forecasts of NORA for some specific alpine catchments are given as input to hydrological models for experimental runoff modeling, in collaboration with WSL (Swiss Federal Institute for Forest, Snow and Landscape Research).

4.2 Outlook

A significant step forward in nowcasting orographic precipitation is expected by combining the knowledge of the orographic forcing with Lagrangian persistence forecasts. The latter is a nowcasting technique consisting in moving rainfall patterns according to the echo motion field retrieved from successive radar images. The McGill algorithm MAPLE (Turner et al., 2004) was applied and evaluated over Switzerland by Mandapaka et al. (2011); such paper is reported in the appendix. The main results suggest that the skill of MAPLE is lower over mountains than in flat regions. This is probably due to the enhancement and dissipation of rainfall which occur in proximity of orographic barriers, and which are not taken into account by Lagrangian extrapolation. The analog approach of NORA, on the other hand, is able to predict also the evolution of rainfall, and for this reason it is in our plans to combine it with MAPLE.
The approach of NORA will be applied to precipitation forecasting in Taiwan in collaboration with NCAR scientists (Roberts et al., 2010), in order to test if also in that region the analogue method is able to significantly improve nowcasting of precipitation.
Subject of our future research will be also the identification and characterization of intense stationary cells which develop over the orography leading to flash floods. The behavior of the predictors measured by NORA in correspondence with these cells will be analysed, in order to look for mesoscale signatures that can be exploited by nowcasting applications.

Appendix A

Can Lagrangian Extrapolation of Radar Fields be used for Precipitation Nowcasting over Complex Alpine Orography?

A.1 Abstract

In this study, we tested if a Lagrangian radar echo extrapolation scheme (MAPLE) can be employed for very short-term forecasting (or nowcasting) of precipitation over complex orographic region. The high resolution forecasts from MAPLE for lead times of 5 min to 5 h are evaluated against the radar observations for 20 summer rainfall events by employing a series of categorical, continuous, and neighborhood evaluation techniques. The verification results are then compared with those from Eulerian persistence forecasts and high resolution numerical weather prediction model (COSMO2) forecasts. The forecasts from MAPLE model clearly outperformed Eulerian persistence forecasts for all the lead times, and had better skill compared to COSMO2 up to lead time of 3 h on average. The results also showed that the predictability achieved from MAPLE model depends on the spatial structure of the precipitation patterns. This study is a first implementation of MAPLE model over complex Alpine region. In addition to comprehensive evaluation of MAPLE, Eulerian and COSMO2 rainfall products, we discuss some open questions related to the nowcasting of rainfall over a complex terrain.

A.2 Introduction

Hydrologic response of a basin to a rainfall event is a result of complex nonlinear interactions between rainfall, hillslope processes, and the river network. For example aggregation and attenuation of flows within the river network plays a key role in determining the shape of the streamflow hydrographs (e.g., Menabde et al., 2001; Mantilla et al., 2006). For smaller mountainous basins such as those in the Alps, the location and timing of the rainfall pattern with respect to the hillslopes and river network are very critical. The response times of such basins are often very short, ranging from sub-hourly to 12 h (e.g., Ahrens et al., 2003; Zillgens et al., 2005). Therefore, flash flood and debris flow forecasting in complex orographic regions requires reliable quantitative precipitation forecasts (QPF) at high space-time resolutions and with very short lead times (up to 5h).

Since weather radars provide good areal coverage with high resolution, many radar based very short-term QPF (also referred to as nowcasting) techniques were developed over the years (e.g., Austin

and Bellon, 1974; Seo and Smith, 1992; Andrieu et al., 1996; Dolciné et al., 1997; Mecklenburg et al., 2000; Pierce et al., 2000; Germann and Zawadzki, 2002; Mueller et al., 2003; Seed, 2003; Bowler et al., 2004, 2006). The radar echo extrapolation is one of the earlier and most widely used very short-term QPF techniques. The forecasts from the extrapolation based models meet aforementioned stringent requirements such as high space-time resolution and short lead times. In addition, due to the the relative simplicity of extrapolation techniques, the corresponding forecasts can be generated with high frequency and in near real-time to provide emergency management authorities sufficient time to issue an alert.

The extrapolation model can be expressed in mathematical form as

$$\hat{\boldsymbol{\Psi}}(t_0 + \tau, \mathbf{x}) = \boldsymbol{\Psi}(t_0, \mathbf{x} - \alpha) \tag{A.1}$$

where $\boldsymbol{\Psi}(t_0, \mathbf{x} - \alpha)$ is the observed precipitation field for time t_0 at location $\mathbf{x} - \alpha$, and $\hat{\boldsymbol{\Psi}}(t_0 + \tau, \mathbf{x})$ is the forecast precipitation field for time lag τ at location $\mathbf{x}$. The estimation of the displacement vector α is an important part of any extrapolation scheme. Techniques such as cell tracking, and variational echo tracking have been employed in various radar echo extrapolation models. The technical details of the tracking algorithms, and the skill of the corresponding forecasts have been reported in the literature for the scales ranging from single radar domain to continental scales (e.g., Bellon and Austin, 1978; Tsonis and Austin, 1981; Bellon and Austin, 1984; Germann and Zawadzki, 2002; Hering et al., 2004; Berenguer et al., 2005; Reyniers, 2008; Sokol et al., 2009; Novák et al., 2009).

Although extrapolation based forecasts were shown to have good skill up to lead times of 1 - 2 h, their skill decreases rapidly with lead time because they do not account for initiation, growth and dissipation of precipitation patterns (e.g., Browning and Collier, 1989; Wilson, 2004). On the other hand, numerical weather prediction (NWP) models have lower skill at short lead times but expected to have better skill than the extrapolation forecasts at longer lead times due to better representation of atmospheric physics. The crossover lead time beyond which NWP model forecasts have better skill than the extrapolation forecasts was estimated to be in the range of 3 - 8 h (e.g., Lin et al., 2005; Vasic et al., 2007). In a recent study (NORA - Nowcasting of rainfall by means of analogues by Panziera L., U. Germann, M. Gabella, and P. V. Mandapaka submitted to Quarterly Journal of Royal Meteorological Society), the authors compared skill of analogue-based nowcasting technique, Eulerian persistence and a numerical weather prediction model (COSMO2) over 8100 km^2 Lago Maggiore region in the South of Alps. They reported better skill of analog-based approach as well as Eulerian persistence over the COSMO2 model up to lead times of 4 h.

The continuous improvement in the ability of the numerical weather prediction (NWP) models to resolve the small scale atmospheric processes prompted researchers to integrate radar data with NWP models to better forecast storm dynamics at short lead times. One approach was to assimilate information from the radar and satellite observations (e.g., boundary layer convergence, radar echo advection) into the NWP models (e.g., Pierce et al., 2000; Mueller et al., 2003; Bowler et al., 2004; Leuenberger, 2005; Bowler et al., 2006; Liang et al., 2010). Another approach was to blend the output from NWP models and radar based QPF systems to improve the accuracy at short space-time scales (e.g., Golding, 1998; Atencia et al., 2010). In a recent study (Blending a probabilistic nowcasting method with a high resolution numerical weather prediction ensemble for convective precipitation forecasts by K. Kober, G. C. Craig, C. Keil, and A. Dornbrack submitted to Quarterly Journal of Royal Meteorological Society), a probabilistic nowcasting method was blended with the high resolution NWP model forecasts and the resulting forecast products were evaluated over a large domain covering Germany.

Despite significant advances in the aforementioned approaches of merging radar based observations and forecasts into NWP models, the resulting forecasts are not up to the desired level of accuracy for scales of thunderstorms and flash floods (e.g., Wilson, 2004; Pierce et al., 2004; Lin et al., 2005; Wilson et al., 2010). For example, Wilson et al. (2010) compared QPFs from various sources for the

Beijing Olympics project and reported that the radar based extrapolation forecasts have much better skill than those from the blended NWP based models.

A.2.1 Objectives

At MeteoSwiss, our aim is to develop an operational heuristic tool for nowcasting of storm advection, growth, and dissipation. Advection is an important component of overall storm evolution and therefore, we intend to use Lagrangian extrapolation of radar fields as a primary component in the above heuristic tool. The next step would be to introduce storm growth and dissipation in a statistical manner. The objectives of this study are twofold.

(1) To quantify the skill achieved by Lagrangian extrapolation of radar fields over the complex region covered by the Swiss radar composite (Visible area = 280,000 km^2).

(2) To compare the skill of extrapolation forecasts with corresponding Eulerian persistence forecasts (baseline scenario), high resolution NWP model forecasts (complex scenario), and estimate the crossover lead time.

The extrapolation scheme selected for the analysis is MAPLE (McGill Algorithm for Precipitation nowcasting using Lagrangian Extrapolation) developed by Germann and Zawadzki (2002). The NWP model selected for the analysis is COSMO2 run by MeteoSwiss as part of COnsortium for Small-scale MOdelling (COSMO) (e.g., Steppeler et al., 2003; Leuenberger and Rossa, 2003). Germann and Zawadzki (2006) evaluated MAPLE using 2720 × 2720 km^2, 4 km resolution radar-reflectivity composites in United States. This study continues in the same vein but performs rigorous evaluation of extrapolation and NWP forecasts for a large domain broadly centered on Switzerland. To the best of our knowledge no such comparison of extrapolation and NWP model forecasts was carried out over complex Alpine terrain.

A.2.2 Radar-rainfall Uncertainties

Before proceeding further a note of caution regarding the radar-rainfall estimation errors: it is well known that radar-rainfall estimates are affected by uncertainties from various sources (e.g., Austin, 1987a; Krajewski and Smith, 2002; Germann et al., 2006; Mandapaka et al., 2009, 2010; Villarini and Krajewski, 2010). Germann et al. (2006) discussed in detail various challenges associated with the radar-rainfall estimation in the mountainous region. Villarini and Krajewski (2010) provided an exhaustive review of various sources of uncertainties in the radar-rainfall estimates. Over the years, several studies evaluated radar-rainfall products, proposed models for residual errors, and employed them to represent radar-rainfall observational uncertainties in the form of ensembles (See Mandapaka and Germann, 2010, for a review).

Likewise, the ensemble framework is also widely used to characterize the uncertainties in the QPF model (for example, errors in the initial conditions, model structure). Germann and Zawadzki (2004) proposed a "local Lagrangian" approach to obtain probabilistic forecasts. In a recent study (SBMcast - An ensemble nowcasting technique to assess the uncertainty in rainfall forecasts by Lagrangian extrapolation by Berenguer M., D. Semperre-Torres, G. Pegram submitted to Journal of Hydrology), a probabilistic Lagrangian extrapolation forecast technique was proposed to account for the temporal evolution of rainfall patterns. However, much work needs to be carried out regarding the superposition of the radar-rainfall estimation errors and the errors that are inherent in the QPF models. In this study we focused on deterministic forecasts from MAPLE and COSMO2 and considered radar-rainfall observations to be the reference rainfall fields. Propagation of rainfall measurement uncertainties through the forecast chain and quantifying the overall errors in the QPF model output is beyond the scope of this study.

A.2.3 Outline

The forecast set-up consisting of MAPLE, Eulerian persistence and COSMO2 models is briefly described in Section 2. The radar-rainfall events are introduced in Section 3 and their space-time characteristics are presented in Section 4. The forecast verification methodology and the corresponding skill scores are described in Section 5. The MAPLE, COSMO2 and Eulerian forecasts are evaluated against the radar observations using a variety of verification approaches in Section 6. A discussion on the limitations of the study and possible improvements is presented in Section 7 followed by conclusions in Section 8.

A.3 Forecast Set-up

A.3.1 Overview of MAPLE

In this section, we provide only a brief description of the MAPLE algorithm, which was originally developed by the radar group at the McGill University, Canada. The algorithm and its skill in forecasting rainfall events over the continental United States has been well documented in a series of papers (e.g., Germann and Zawadzki, 2002, 2004; Turner et al., 2004; Germann and Zawadzki, 2006). Recently, a thorough sensitivity analysis and a real-time verification of the MAPLE model was carried out using the radar network in South Korea (Bellon et al., 2010; Lee et al., 2010). The MAPLE forecast setup primarily consists of two steps:

(1) Velocity field estimation using the variational echo tracking algorithm

(2) Extrapolation of the current radar image honoring the motion field estimated in the above step

Variational Echo Tracking

The variational echo tracking (VET) algorithm was proposed by Laroche and Zawadzki (1994) to estimate the three-dimensional wind field from the single Doppler clear-air echoes. The technique was later modified by Germann and Zawadzki (2002) to obtain the velocity field from the radar-rainfall composites. The technique basically minimizes the following cost function

$$J_{VET}(\mathbf{u}) = J_\Psi + J_2 \tag{A.2}$$

The first term J_Ψ is the sum squares of residuals of the conservation equation.

$$
\begin{aligned}
J_\Psi = \int \int_\Omega \beta(\mathbf{x})[\Psi(t_0, \mathbf{x}) - \\
\Psi(t_0 - \Delta t, \mathbf{x} - \mathbf{u}\Delta t)]^2 \ dx \ dy
\end{aligned}
\tag{A.3}
$$

where $\beta(\mathbf{x})$ is the weighting factor reprsenting the data quality. The second term in the equation J_2 is a smoothness penalty function written as

$$
\begin{aligned}
J_2 = \gamma \int \int_\Omega \left(\frac{\partial^2 u}{\partial x^2}\right)^2 + \left(\frac{\partial^2 u}{\partial y^2}\right)^2 + 2\left(\frac{\partial^2 u}{\partial x \partial y}\right)^2 \\
+ \left(\frac{\partial^2 v}{\partial x^2}\right)^2 + \left(\frac{\partial^2 v}{\partial y^2}\right)^2 + 2\left(\frac{\partial^2 v}{\partial x \partial y}\right)^2 \ dx \ dy
\end{aligned}
\tag{A.4}
$$

where γ is a constant weight and u and v are the x- and y-components of the the velocity field $\mathbf{u}$ respectively. Similar to Germann and Zawadzki (2002), conjugate-gradient algorithm was used in

the global minimization of the above cost function. To avoid converging towards secondary minima, Germann and Zawadzki (2002) followed the scaling-guess procedure (Laroche and Zawadzki, 1994), where the VET algorithm is iteratively initiated and run at multiple scales starting with coarser scales and gradually moving down to finer scales. We adopted the same approach and estimated the velocity fields starting with a coarse resolution of 600×600 km^2 (one vector for the entire domain), 100×100 km^2 (6×6 vectors), and to a final resolution of 25×25 km^2 (24×24 vectors). The procedure was repeated every 5 min using 30 min of past radar-reflectivity composites. All the computations were carried out using radar-reflectivity fields in dBZ scale and the pixels with reflectivity value < 10 dBZ (rain rate of 0.1 mm/h) were considered to be non-rainy.

Radar Echo Extrapolation

There are various ways in which the velocity field from the VET technique can be used in extrapolation of radar echoes. Germann and Zawadzki (2002) described the following four methods: 1) constant vector forward scheme, 2) constant vector backward scheme, 3) semi-Lagrangian forward scheme, and 4) semi-Lagrangian backward scheme. In this study we employed semi-Lagrangian backward scheme in the radar echo extrapolation module. In the semi-Lagrangian backward scheme the origin of a parcel that would end up at a particular grid point in the forecast field is determined by following the streamlines upstream in space and backward in time. Semi-Lagrangian scheme also allows for the rotation in the displacement vector α for the extrapolation up to certain lead time τ.

Given the velocity field $\mathbf{u}$ at the time instant t_0 from the VET algorithm, the lead time τ is divided into N time steps of length Δt, and α is iteratively obtained as follows:

$$\alpha = \Delta t \mathbf{u}\left(t_0, \mathbf{x} - \frac{\alpha}{2}\right) \tag{A.5}$$

The origin of the parcel determined using backward scheme may not always coincide with a grid point in the current reflectivity field. In such a scenario, bilinear interpolation was carried out to estimate the reflectivity value at the origin. In addition, for longer lead times, it is theoretically possible that the backward scheme locates the origin of a parcel to be outside the domain covered by the radar composite. Such pixels are flagged out in the forecasts and not considered in the forecast evaluation.

A.3.2 Eulerian Persistence

In the Eulerian persistence, the current radar-rainfall image is taken as a forecast for all the lead times. According to equation A.1, the displacement vector α is equal to zero. The approach is simple and is usually taken as a baseline system in the forecast evaluation studies.

A.3.3 NWP model: COSMO2

COSMO model is developed as a part of major research cooperation between several national weather services in Europe. It is a high resolution, limited-area, nonhydrostatic numerical weather prediction model. There are many configurations of the model such as COSMO-LEPS, COSMO-EU, COSMO7, and COSMO2. Some of the main differences between the above COSMO versions is the spatial resolution, updating frequency, forecast range, and the spatial extent for which they are available. For example, COSMO7 has a resolution of 6.6 km, runs every 12 h, and has a forecast range of 24 h. For more information, please refer to the COSMO model documentation available online at http://cosmo-model.org. We selected COSMO2, which has a resolution of 2.2 km and updating frequency of 3 h because of the nowcasting requirements.

A.4 Data Catalogue

Radar-rainfall data of 20 summer (June, July, and August) rainfall events between 2005 and 2010 are used to evaluate the forecasts. We limited the selection of the events to the summer season to reduce the effects of seasonality on the verification results. The instantaneous reflectivity measurements from MeteoSwiss network of three Doppler radars undergo several steps of data processing and quality control process before being merged into 5-minute rain rate composites on a rectangular grid of 1 km spatial resolution. Some of the major steps in the data processing and quality control process are the identification and mitigation of ground clutter, correction for the vertical variability of the radar-reflectivity, polar-Cartesian grid transformation, and creating the reflectivity composite (e.g., Joss and Lee, 1995; Germann and Joss, 2002; Germann et al., 2006).

The 20 summer events form a total of 854 hours of rainfall. Table A.1 lists some basic features of the events while A.1 shows the spatial distribution of event-scale accumulation fields. Hereafter the events will be referred to by the names mentioned in the first column of table A.1. Although the selection of events was limited to summer months of June, July and August, the events displayed space-time structure that is quite different from each other (table A.1 and figure A.1). For example, the event 05231 is characterized by quasi-stationary behavior with widespread rainfall for several hours while the event 10157 contained several small and intense convective showers lasting for short duration. Two of the selected events (05231 and 07220) resulted in catastrophic flooding (e.g., Beniston, 2006; Jaun et al., 2008; Schmutz et al., 2008).

Even after various quality checks, the radar dataset is not free of errors and data artifacts. One
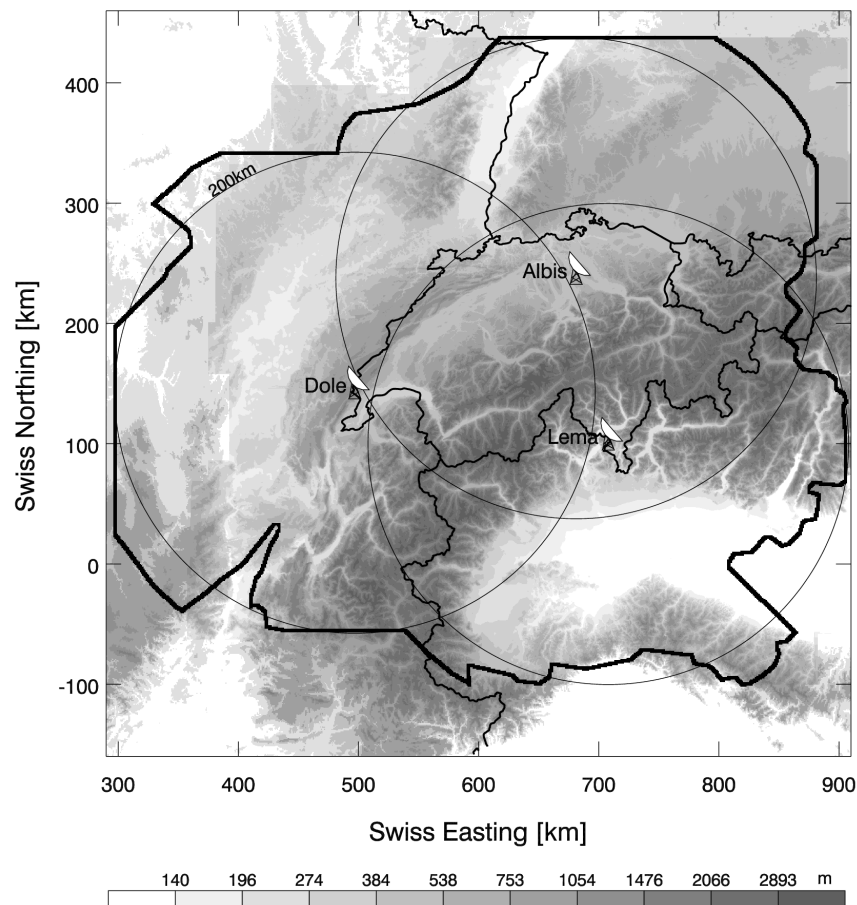
Figure A.1: *Map showing the complex orography of the study region, the radar quality mask, and location of the three radars within 620 × 620 km^2 domain.*

Table A.1: *List showing beginning, end, duration, and the total accumulation for each event. The events for which COSMO2 data was available are indicated by 'Y' in the last column*

Event ID	Begin	End	Duration [h]	Accumulation [mm]	COSMO2
05231	18/08/2005 10:05	23/08/2005 02:00	88.0	297.5	N
06175	24/06/2006 09:05	26/06/2006 02:00	41.0	156.8	N
06185	04/07/2006 09:05	06/07/2006 18:00	33.0	207.1	N
06202	21/07/2006 09:05	22/07/2006 18:00	33.0	104.7	N
07156	05/06/2007 10:35	05/06/2007 23:30	13.0	54.9	N
07171	20/06/2007 12:35	22/06/2007 13:00	24.5	193.9	N
07189	08/07/2007 01:05	09/07/2007 12:00	35.0	139.2	N
07220	08/08/2007 11:05	09/08/2007 16:30	53.5	258.2	Y
07240	28/08/2007 05:35	31/08/2007 05:30	72.0	263.4	Y
08181	29/06/2008 11:35	29/06/2008 23:30	12.0	72.3	Y
08194	12/07/2008 01:05	14/07/2008 07:00	54.0	233.0	Y
08214	01/08/2008 01:05	02/08/2008 01:30	23.5	111.5	Y
08227	14/08/2008 13:05	15/08/2008 19:00	30.0	140.6	Y
09176	25/06/2009 13:05	27/06/2009 18:00	29.0	133.3	Y
09215	03/08/2009 01:05	03/08/2009 15:00	14.0	46.5	Y
09219	07/08/2009 01:05	08/08/2009 18:30	41.5	129.2	Y
09221	09/08/2009 07:10	10/08/2009 08:00	24.9	100.5	Y
10157	06/06/2010 09:05	07/06/2010 04:00	19.0	86.6	N
10183	01/07/2010 10:05	04/07/2010 18:00	56.0	212.8	Y
10191	10/07/2010 10:05	12/07/2010 18:50	56.8	244.5	Y

such artifact can be clearly noticed in the accumulation fields in the south-west direction (A.1). To account for such artifacts (e.g., ground clutter, blocking by mountains), we performed a probability-based analysis using 854 hours of radar-reflectivity composites. For each pixel within the composite field, we estimated the probability that the reflectivity is greater than 10 dBZ. A pixel affected by the blocking would result in a very low probability of detection whereas a pixel affected by the ground clutter results in a high probability of detection. After trying out several cut-offs, the coverage and ground clutter probability thresholds were chosen as 2% and 75% respectively. It should be noted that the above brute-force approach is only aimed at identifying any remaining artifacts in the reflectivity composites after the rigorous physically based quality control process.

Around 28,000 pixels had probability of detection $< 2\%$ and therefore classified as affected by the radar beam blockage. While most of these pixels lie far from the location of the radar, some of them are related to the obstacle in the southwest direction of La Dole radar (A.2). None of the pixels had probability of detection $> 75\%$. We repeated the analysis for different probability thresholds. The number of pixels were sensitive to the lower threshold ($\sim$22,000 for 1% to $\sim$32,000 for 5%) but not to the upper threshold. We decided to use the threshold of 2 % and excluded 28,000 pixels from the further analysis.

A.5 Event Characteristics

In this section we characterize the space-time characteristics of each of the selected rainfall events. Better characterization of the rainfall events will lead to a better understanding of the forecast errors. The spatial structure of the reflectivity composite at each time step is characterized in the form of image mean flux (IMF), wet area ratio (WAR), and the two-dimensional semivariogram for the quality
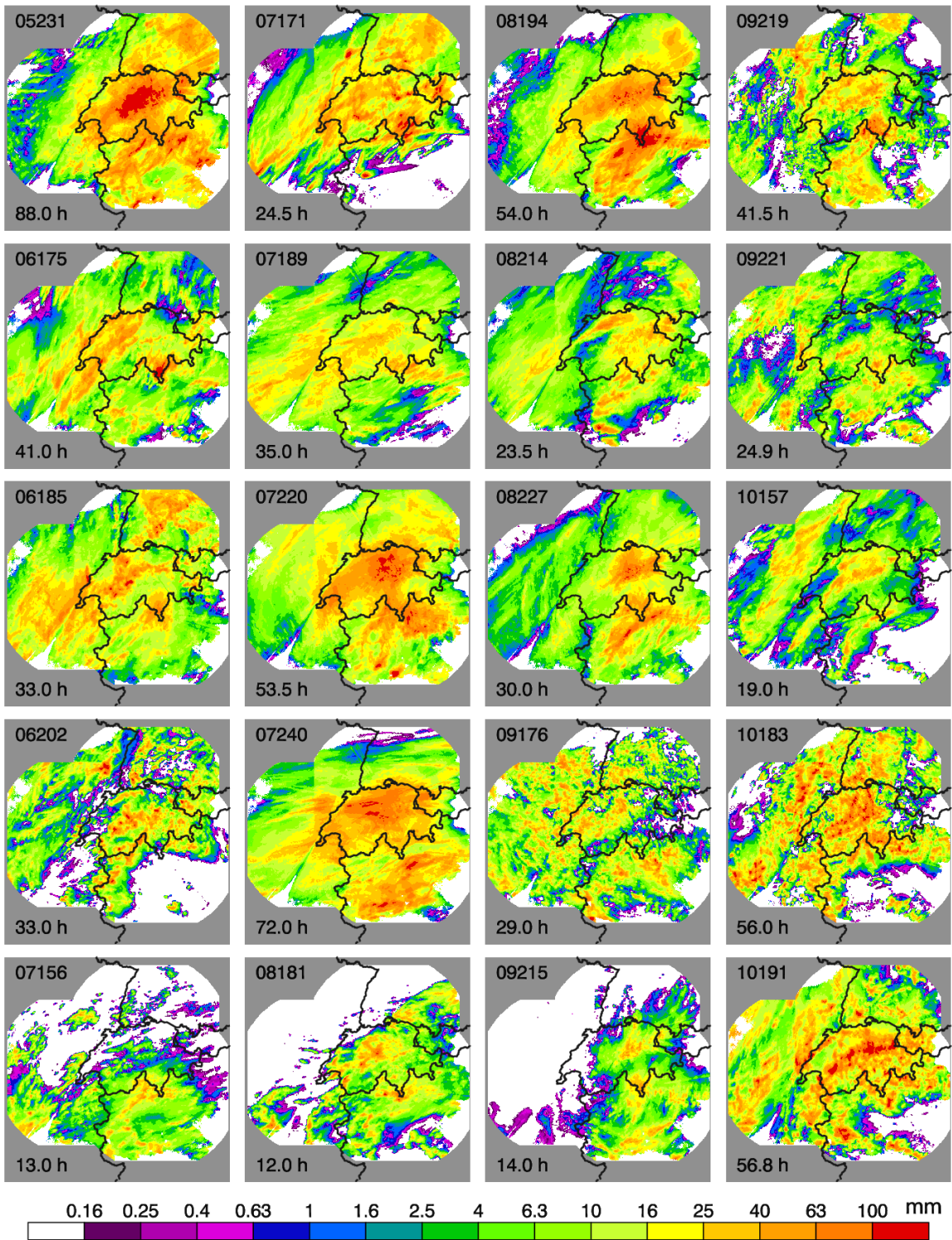
Figure A.2: *Spatial distribution of event-scale rainfall accumulation for each of the selected events over 620×620 km² domain broadly centered on Switzerland. The event ID and the duration are indicated on each panel.*

mask shown in figure A.2. Estimation of IMF and WAR was straightforward. The IMF is the average of rain rate values over all the pixels whereas WAR is the rainy fraction within the quality mask. Note that throughout the study, we have employed the Z-R relation $Z = 316R^{1.5}$ to convert reflectivity to rainrate.
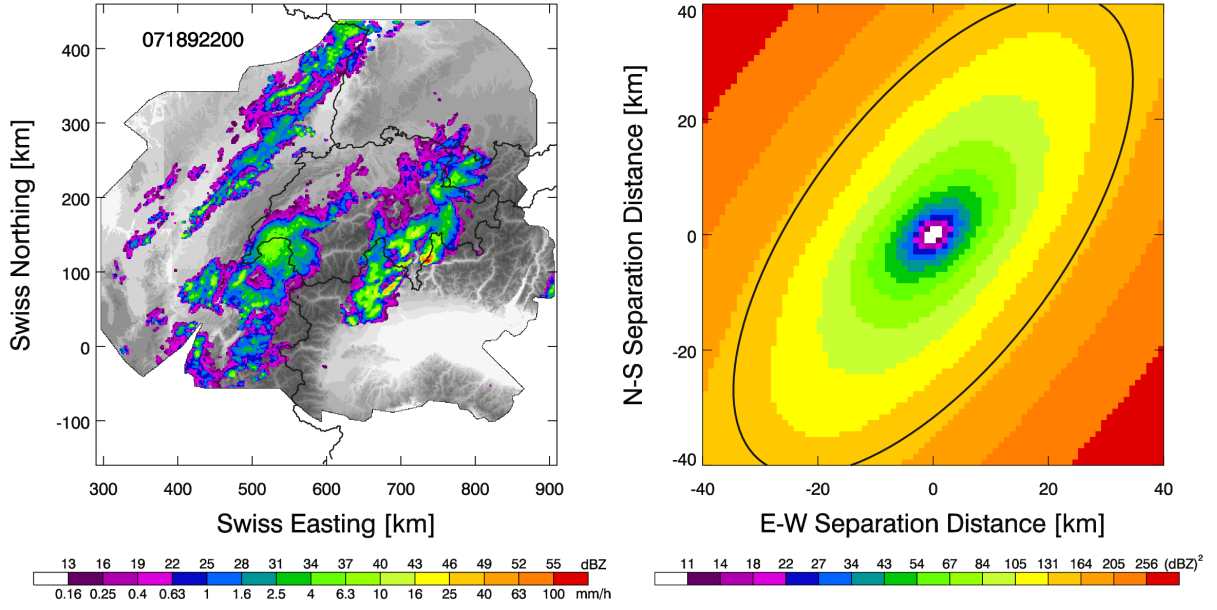
Figure A.3: *Sample 5-min radar field and the corresponding two-dimensional semivariogram in* $(dBZ)^2$. *The timestamp in yydddhhmm format is shown on the radar field. The figure also shows the elliptical Gaussian function fitted to the 2D variogram.*

The two-dimensional semivariogram was estimated as follows. For each possible inter-pixel combination within the quality mask (figure A.2), we estimated the semivariance using the classical method-of-moments estimator (e.g., Cressie, 1993)

$$\gamma(d) = \frac{1}{2n_d} \sum_{n_d} (Z_i - Z_j)^2 \tag{A.6}$$

where Z_i is the reflectivity value in dBZ for the pixel i, n_d is the number of pairs separated by the distance d, and $\gamma(d)$ is the semivariance estimate. The distribution of semivariance with each inter-pixel combination is referred to as two-dimensional semivariogram. We limited the estimation of semivariance to the 40 × 40 km grid. Although it is sufficient to display the semivariogram field for just two quadrants (because of the property of conjugate symmetry), we show it for all four quadrants for better visualization.

An example rain rate field at a particular time step within the event 07189 and the corresponding 2D semivariogram is shown in figure A.4. The presence of banded structure suggests clear anisotropy in the reflectivity (and rain rate) field. The 2D semivariogram was then fitted with a two-dimensional elliptical Gaussian function of the form

$$F(x, y) = A_0 + A_1 e^{-U/2} \tag{A.7}$$

where U is the elliptical function defined as

$$
\begin{aligned}
U &= \left(\frac{x'}{a}\right)^2 + \left(\frac{y'}{b}\right)^2 \\
x' &= x\cos\theta - y\sin\theta \\
y' &= x\sin\theta + y\cos\theta
\end{aligned}
\tag{A.8}
$$

In the above equation, $2a$ and $2b$ are the axis lengths in the unrotated X and Y respectively, and θ denotes the clockwise rotation of the ellipse in radians. The parameters were estimated using

83

Levenberg-Marquardt algorithm (e.g., Press et al., 1992). The 2D semivariogram and the corresponding parameters were estimated only for those time steps within the event for which rainy area is at least 4000 km^2 (WAR $\sim$ 0.015). This is done to reduce the effects of small sample size on the estimation of semivariance. Later in this study, we relate the event characteristics to the predictability of the forecasts from the MAPLE.

A.6 Forecast Evaluation Framework

Several verification techniques were proposed in the literature to characterize the forecast performance. However, no single verification technique (and the associated single skill score) gives a complete picture of the forecast performance. The skill scores can be broadly classified into those:
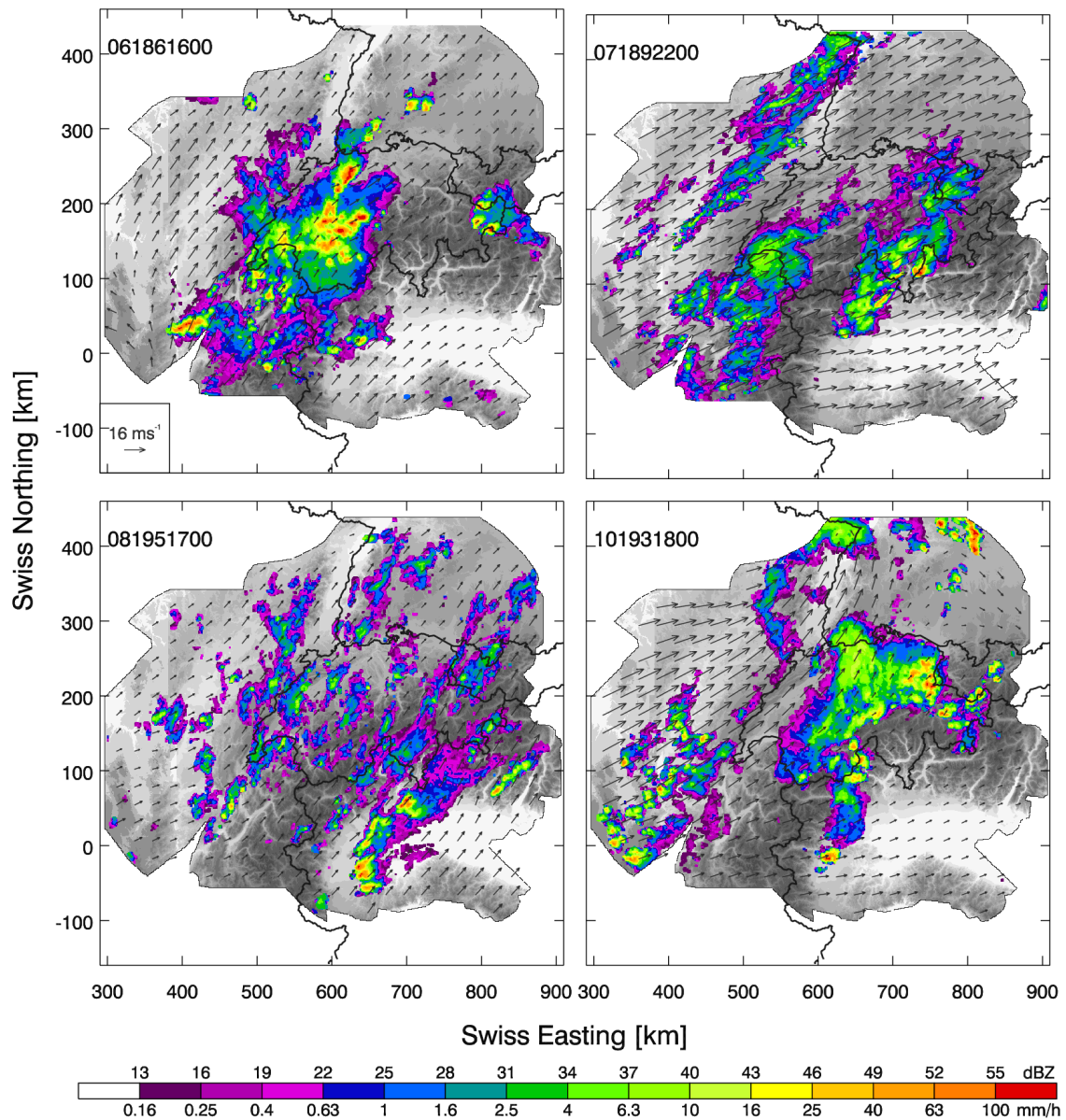
Figure A.4: *Sample 5-min radar fields and the corresponding velocities estimated using the variational echo tracking algorithm. The timestamp in yydddhhmm format is shown on each panel radar field.*

(a) that focus on the ability of forecasts to reproduce different classes of rainfall intensities (e.g., Gilbert skill score)

(b) that utilize the continuos spectrum of available forecast-observation pairs (e.g., mean absolute error)

(c) that consider certain neighborhood into account while performing evaluation (e.g., fractions skill score)

(d) that compare the spatial structure of forecasts and observations (e.g., semivariograms).

(e) that characterize how well a specific object is reproduced in the forecast (object-oriented evaluation)

We selected a combination of categorical, continuous, and neighborhood verification strategies to evaluate MAPLE, Eulerian, and COSMO2 forecasts. The evaluation was performed at the finest space and time resolutions; that is, 1 km in space and 5 min in time. Therefore, evaluation is conservative in the sense that any coarsening to larger scales would only mean better performance.

A.6.1 Categorical Verification

In this study we limit the categorical evaluation to binary rain/no-rain patterns. All the pixels with reflectivity value below certain threshold (Z_t) were considered as non-rainy and those with $Z \geq Z_t$ were considered as rainy. For each lead time, we applied the threshold to all the observed and forecast fields within an event, and prepared a 2 × 2 contingency table consisting of number of hits (a), false alarms (b), misses (c), and correct negatives (d) (table A.2). The above procedure was then repeated for each event, and for three reflectivity thresholds: 10 dBZ (R = 0.1 mm/h), 25 dBZ (R = 1.0 mm/h), and 35 dBZ (R = 5.0 mm/h). The contingency tables thus created were then used to compute the skill scores. It should be noted that the contingency table and the binary evaluation results are independent of the intensity scale (mm/h vs dBZ) as long as the pixel values and thresholds are converted appropriately using a Z-R relation.

Table A.2: *Two-dimensional contingency table*

	Forecast	
Observation	$R \geq R_t$	$R < R_t$
$R \geq R_t$	hit (a)	miss (c)
$R < R_t$	false alarm (b)	correct negative (d)

Some of the desirable properties of categorical scores are equitability, transpose symmetry, and independence to the base rate ($p = \frac{a+c}{n}$) of observations (e.g., Stephenson, 2000; Göber et al., 2004; Jolliffe, 2008; Hogan et al., 2009, 2010). An equitable skill score considers any improved skill in the forecasting system just by chance occurrence (random forecasts). It can be written as (e.g., Hogan et al., 2009):

$$\frac{X - X_r}{X_p - X_r} \tag{A.9}$$

where X is a function of the contingency table (a, b, c, d), X_p is the value of X for perfect forecast, and X_r is a function of random contingency table (a_r, b_r, c_r, d_r; table A.3). The elements of random contingency table were obtained using equations given by Stephenson (2000). The base rate p is an indicator of the sample climatology of the observations. A skill score that is highly sensitive to the base rate yields very small value for rare events making it difficult to compare the performance of

Table A.3: *Two-dimensional random contingency table*

	Forecast	
Observation	$R \geq R_t$	$R < R_t$
$R \geq R_t$	$a_r = (a+b)(a+c)/n$	$c_r = (a+c)(c+d)/n$
$R < R_t$	$b_r = (a+b)(b+d)/n$	$d_r = (b+d)(c+d)/n$

forecasts for such extreme cases. Therefore, it is important to select a skill score that is independent of the base rate of the event.

We selected frequency bias, probability of detection, false alarm ratio, Gilbert skill score, odds ratio, and symmetric extreme dependence score in categorical evaluation. Frequency bias (FB) is defined as the ratio of number of pixels in forecasts to the number of pixels in observed fields exceeding a given threshold. Probability of detection (POD), false alarm ratio (FAR) and Gilbert skill score (GSS), which is also known as equitable threat score, have been widely used in the literature. Their definitions can be found in any standard book on forecast verification (e.g. Joliffe and Stephenson, 2003; Wilks, 1995). The odds ratio is defined as the ratio of odds of correct detection to the wrong detection of precipitation over a certain threshold (e.g., Stephenson, 2000; Göber et al., 2004). If the logarithm of odds ratio (LOR) is less than 0, it means that the forecasts have no added value compared to the climatological mean. Symmetric extreme dependence score (SEDS) was proposed by Hogan et al. (2009). They demonstrated that the SEDS is a robust verification score particularly for the extreme events. The mathematical expressions of each skill score and the possible range of these scores are shown in table A.4.

Although FB, POD and FAR do not meet the requirements such as equitability, transpose symmetry and independence to base rate, we included them in categorical evaluation to compare the results of the present study with those reported in the literature. On the other hand, the GSS, SEDS, and LOR are equitable (for large samples) and transpose symmetric, whereas SEDS and LOR are independent of the base rate.

A.6.2 Continuous Verification

Continuous verification implies the use of the entire spectrum of the rainfall intensity scale to characterize the forecast performance. Similar to the categorical skill scores, there are several continuous verification measures which can be used to assess the quality of forecast. Some of the most widely used measures are correlation, mean absolute error, and root mean square error. We selected mean absolute error (MAE) and correlation coefficient for this study and estimated it using the following equation (e.g., Germann and Zawadzki, 2002)

$$r = \frac{\sum_{n}(Z_O Z_F)}{\left[\sum_{n}(Z_O)^2 \sum_{n}(Z_F)^2\right]^{1/2}} \tag{A.10}$$

where n denotes the number of pixels in the quality mask, r is the correlation coefficient, and Z_O and Z_F are the observed and forecast reflectivity fields (in dBZ scale) respectively. For an exponential decay of correlation coefficient with the lead time, the lifetime of forecasts can be defined as the time at which the correlation drops to $1/e$ (e.g., Germann and Zawadzki, 2002). We followed the same definition and estimated the lifetime of MAPLE, Eulerian and COSMO2 forecasts.

Table A.4: *Categorical skill scores*

Skill Score	Formula	Range
Frequency Bias (FB)	$\dfrac{a+b}{a+c}$	$[0,\infty]$
Probability of Detection (POD)	$\dfrac{a}{a+c}$	[0,1]
False Alarm Ratio (FAR)	$\dfrac{b}{a+b}$	[0,1]
Gilbert Skill Score (GSS)	$\dfrac{a-a_r}{a+b+c-a_r}$	[-1/3,1]
Symmetric Extreme Dependency Score (SEDS)	$\dfrac{log(a_r/n)}{log(a/n)}-1$	[0,1]
Log Odds Ratio (LOR)	$log\left(\dfrac{ad}{bc}\dfrac{b_r c_r}{a_r d_r}\right)$	$[-\infty,\infty]$

A.6.3 Neighborhood Verification

The skill scores discussed until now were based on pixel-to-pixel comparison of high resolution gridded forecast and observed rainfall fields. With large uncertainties in observations and in the QPF model output at high resolutions, the pixel-to-pixel approach is very restrictive and may not be a better indicator of forecast performance at fine scales. In recent years, studies have proposed and employed skill scores that take pixels from neighborhood into account while evaluating the gridded forecasts (e.g., Germann and Zawadzki, 2002, 2004; Roberts and Lean, 2008; Weusthoff et al., 2010; Zacharov and Rezacova, 2010). For a given pixel in a high resolution forecast field, the verification can be performed by considering a neighborhood only in forecast field, only in observation, or both in forecast and observed fields. Ebert (2008, 2009) provide comprehensive review of verification techniques falling into one of the above categories.

We employed fractions skill score proposed by Roberts and Lean (2008). For a given neighborhood around a pixel in forecast and observed fields, the fractional observed (P_O) and forecast (P_F) rain areas were computed. Fractions skill score (FSS) was then estimated using

$$
FBS = \frac{1}{n_n}\sum_{n_n}(P_F - P_O)^2
$$
$$
FSS = 1 - \frac{FBS}{\dfrac{1}{n_n}\left(\displaystyle\sum_{n_n} P_O^2 + \sum_{n_n} P_F^2\right)} \tag{A.11}
$$

where n_n indicates the number of neighborhoods in the study region. The fractions skill score ranges from 0 to 1; 0 indicating no skill and 1 indicating perfect skill. The value of FSS is obviously the smallest at the highest resolution and increases with the increase in the size of the neighborhood.

A.7   Forecast Evaluation Results

As mentioned in section 3, we selected 854 h of radar-rainfall data corresponding to 20 summer events (2005 - 2010) for this study. For each time step within the event, we estimated the storm motion field using the VET algorithm described in Section 2. Figure A.4 shows sample rainrate field and the corresponding storm motion field at different time steps and for different events. The current reflectivity field was then extrapolated following the storm motion field up to lead time of 5 h with a time resolution of 5 min. The Eulerian forecasts were generated in same manner except that the storm motion field was assumed to be zero. Thus, we have MAPLE and Eulerian forecasts every 5 min with a spatial resolution of 1 km and lead times varying from 5 min to 5 h for the 20 selected events. However, COSMO2 rainfall forecasts were only available starting from July 2007. Therefore we split the discussion of results into two parts: In the first part, we compare the skill scores of MAPLE and Eulerian persistence forecasts using 20 events from 2005 - 2010, and in the second part we compare skill scores of MAPLE, COSMO2, and Eulerian persistence forecasts using 12 events from 2007 - 2010.

A.7.1   MAPLE and Eulerian forecasts: 20 Events

We begin the verification with a comparison of the spatial distribution of event accumulations from MAPLE (3 h lead time) and radar observations for four events (figure A.5). Such a comparison gives an overall idea about the performance of the forecasting tool. MAPLE model does a good job in forecasting the spatial patterns of the event accumulations even for a lead time of 3 h (figure A.5). Although there are differences between MAPLE forecasts and observations when looking at specific locations, the general pattern of rainfall accumulations from MAPLE is similar to observations. We then quantified the skill in MAPLE forecasts at the highest resolution of 5 min in time and 1 km in space using the verification approaches discussed in previous section. All the verification except the estimation of MAE was carried out on the reflectivity values in dBZ scale.
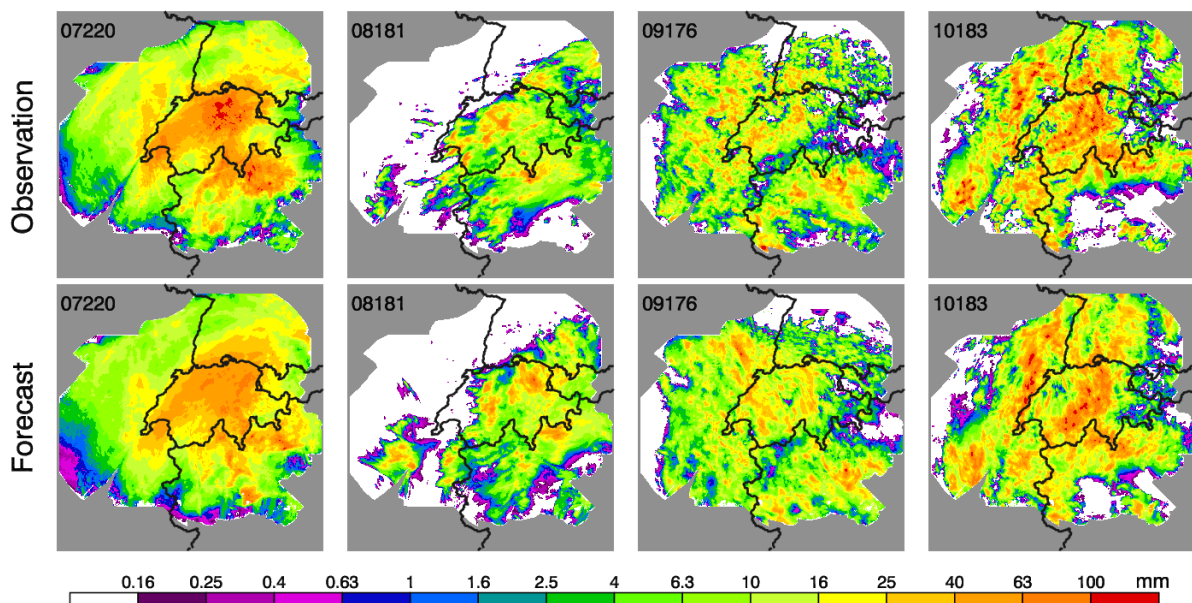
Figure A.5: *Comparison of observed and MAPLE forecasted rainfall accumulations for four of the selected events. The forecast accumulations are for a lead time of 3 hours.*

Binary Evaluation

For each combination of lead time and Z_t threshold, contingency tables (tables A.2 and A.3) were obtained by applying Z_t for all the observed and forecasted reflectivity fields within an event. From the contingency tables, the skill scores were estimated using equations given in table A.4. The forecasts for a particular event can be evaluated by plotting the skill score as a function of lead time for a certain Z_t. We obtained 20 such skill score vs lead time curves for the 20 events considered in this study. To get insight into the storm-to-storm variability in the forecast skill, we estimated the average, minimum, and maximum skill score of the 20 events for each lead time.
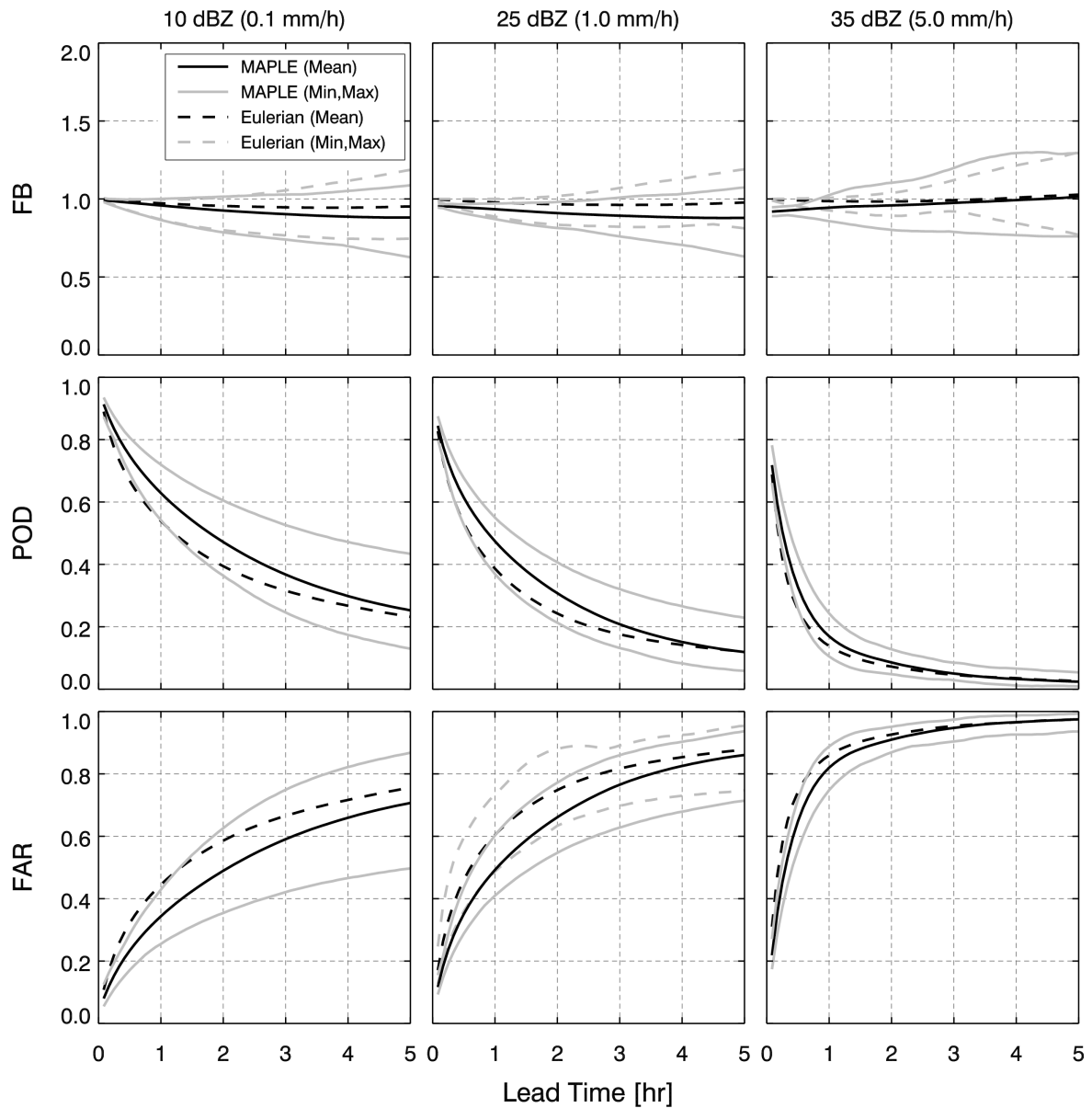
The variation of the frequency bias (FB), probability of detection (POD), and false alarm ratio (FAR) with the lead time is shown in figure A.6. The solid dark line indicates the average skill score from the MAPLE forecasts while the gray lines indicate the minimum and maximum scores (from 20 events). For $Z_t = 10$ dBZ, the average FB value varied from 0.99 at 5 min to 0.88 at 5 h. As the lead time increased from 5 min to 5 h, the number of pixels in MAPLE forecasts with $Z \geq Z_t$ gradually decreased in comparison to those of observed reflectivity fields. The behavior is similar for $Z_t = 25$ dBZ, where the average FB decreased from 0.96 at 5 min to 0.88 at 5 h lead time (figure A.6). However, for Z_t of 35 dBZ, the average FB increased slightly from 0.96 at 5 min to 1.02 at 5 h. From the figure A.6, it can also be seen that the storm-to-storm variability in the FB values is larger for higher threshold. The average FB of Eulerian persistence forecasts is very close to 1 for all the lead times (figure A.6). This is expected of the Eulerian persistence forecasts as they are theoretically unbiased.

Figure A.6 further shows that the skill in MAPLE forecasts as characterized by POD and FAR decreased with the increase in the lead time and Z_t. As pointed out by Golding (1998), the decrease in forecast skill with the increase in lead time is a reflection of the fact that in a chaotic system such as rainfall, there is an inevitable loss of information with the lead time. Whereas the decrease in forecast skill with the increase in Z_t is due to smaller localized precipitation systems at higher thresholds. From the figure A.6, it can also be seen that the inter-storm variability in the skill scores reduced with the increase in Z_t meaning that the forecast skill at higher thresholds is consistently lower for all the events. Later in this section, we analyze in detail the relation between the event characteristics and the skill in MAPLE forecasts. The skill in the Eulerian persistence forecasts as characterized by POD and FAR is lower than the MAPLE forecasts for all the lead times and for $Z_t = 10$ and 25 dBZ. The behavior is similar for higher threshold of 35 dBZ but only up to a lead time of 3 h. Beyond a lead time of 3 h, the POD and FAR of MAPLE and Eulerian forecasts are almost identical (figure A.6).

The GSS, SEDS, and LOR decreased with the increase in lead time and Z_t (figure A.7). For Z_t = 10 and 25 dBZ, all the three scores suggest better skill in MAPLE forecasts compared to that of Eulerian forecasts for all the lead times. For $Z_t = 35$ dBZ MAPLE outperforms Eulerian forecasts only for lead times up to three and a half hours. The logarithm of odds ratio for both the Eulerian and MAPLE forecasts is mostly above zero suggesting that the forecasts indeed have added value compared to the climatological forecasts. Similar to POD and FAR, the inter-storm variability in GSS decreased with the increase in Z_t (figure A.7).

Continuous Evaluation

We now proceed to continuous evaluation and estimate mean absolute error (MAE) and the correlation coefficient between the forecast and observed fields. A comparison of MAE in Eulerian and MAPLE forecasts is shown in figure A.8. The MAE in Eulerian forecasts is larger than the MAE in MAPLE forecasts for all the lead times. The MAE increases rapidly up to lead time of 1 h and reaches an asymptote for longer lead times of 4 - 5 h. Figure A.8 also shows the inter-storm variability of MAE in MAPLE forecasts. The correlation coefficient between the observed and forecast reflectivity fields was estimated for each event and all the lead times using equation A.10. The average, minimum and

Figure A.6: *Frequency bias (FB), probability of detection (POD) and false alarm ratio (FAR) of MAPLE and Eulerian forecasts as a function of lead time for three rain/no-rain thresholds. For each event, a skill score vs lead time curve was estimated by comparing all the 5 min observed and forecasted fields for all the lead times. The solid dark line represents the 20-event average, and the solid gray lines characterize event-to-event variability in MAPLE skill.*

maximum correlation coefficient of 20 events was then obtained for each lead time. The solid dark line in figure A.9 represents the variation of 20-event average correlation coefficient with the lead time whereas the solid gray lines indicate the variation of minimum and maximum correlations with the lead time. The correlations between MAPLE forecasts and observations displayed an exponential decay with lead time for all the events. Figure A.9 also shows the 20-event average correlation coefficients for the Eulerian persistence forecasts.

It may be recalled (from section 5) that for an exponential decay of correlation with lead time, the lifetime of forecasts is defined as the lead time at which the correlation drops to $1/e$ (e.g., Germann and Zawadzki, 2002). We fitted the correlations obtained for each event with an exponential function of the form $\exp[-(\tau/\tau_l)]$, where τ is the lead time and τ_l is the lifetime. The average lifetime for the
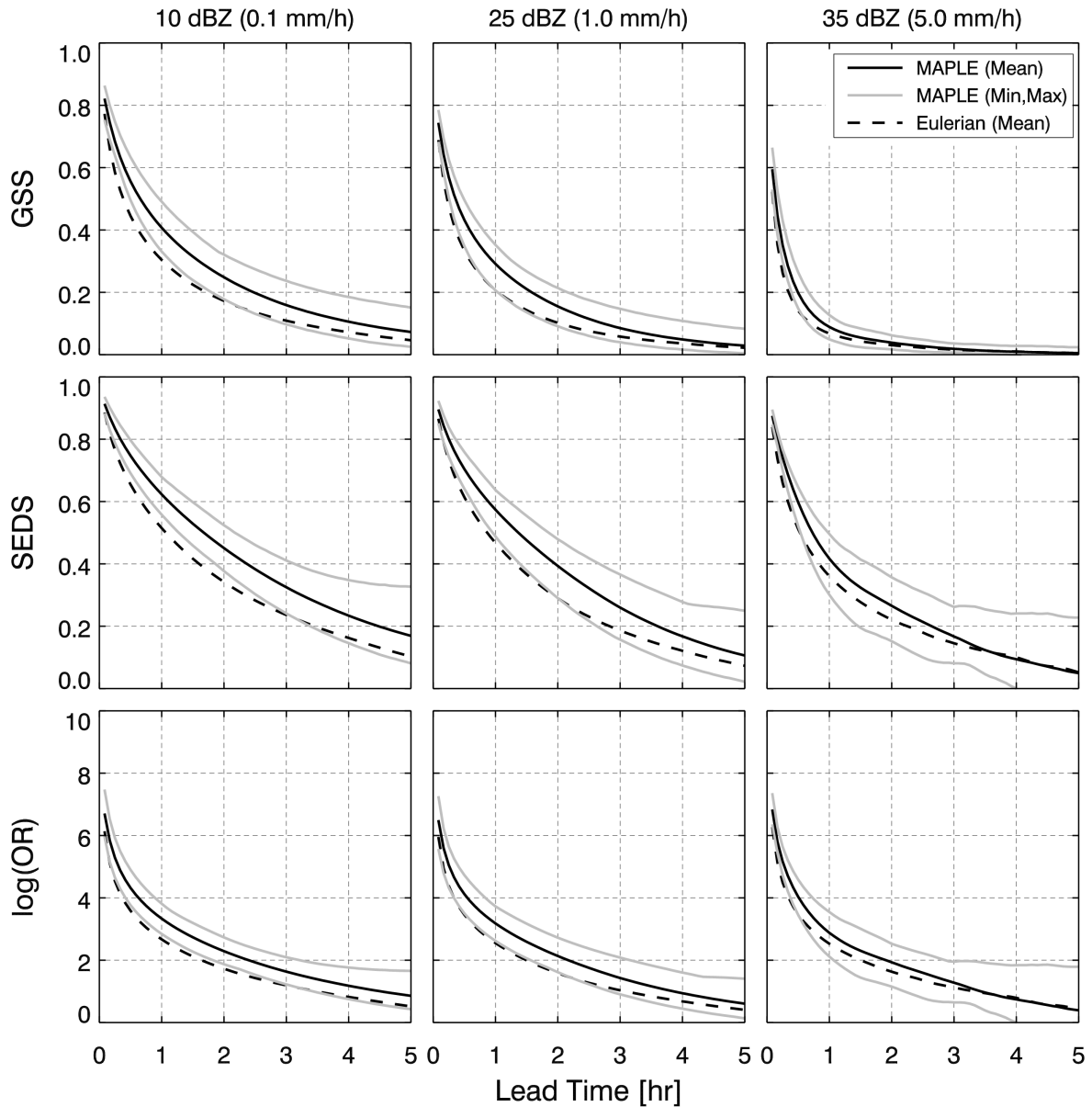
Figure A.7: *Same as figure A.6 but for the Gilbert skill score (GSS), symmetric extreme dependence score (SEDS), and odds ratio (OR).*

MAPLE forecasts was found to be around 3 h. It is lowest (2 h) for the event 10183 and highest (6.5 h) for the event 07220. The lifetime for the Eulerian forecasts was found to be around 2.1 h. That is, we gain a buffer of 1h in lifetime by moving from Eulerian to semi-Lagrangian (MAPLE) forecast space. It should be noted that the result depends on such factors as the geography of the region (e.g., complex orography vs flat terrain), the meteorological situation (e.g., convective vs stratiform events), and the data characteristics (e.g., space-time resolution).

Based on an analysis of 1424 h of warm season rainfall events over continental United States, Germann and Zawadzki (2006) reported average lifetime of MAPLE forecast to be 5.1 h. The study showed that the lifetimes are longer over the midwestern United States with long-living mesoscale precipitation systems, and shorter over Texas and Florida with pronounced convective activity. They also showed that the average lifetime of Eulerian persistence forecasts is around 2.9 h. That is, they obtained a gain of about 2.2 h by moving from Eulerian to semi-Lagrangian extrapolation approach.

One reason for the relatively shorter gain of 1 h obtained in the current study compared to that
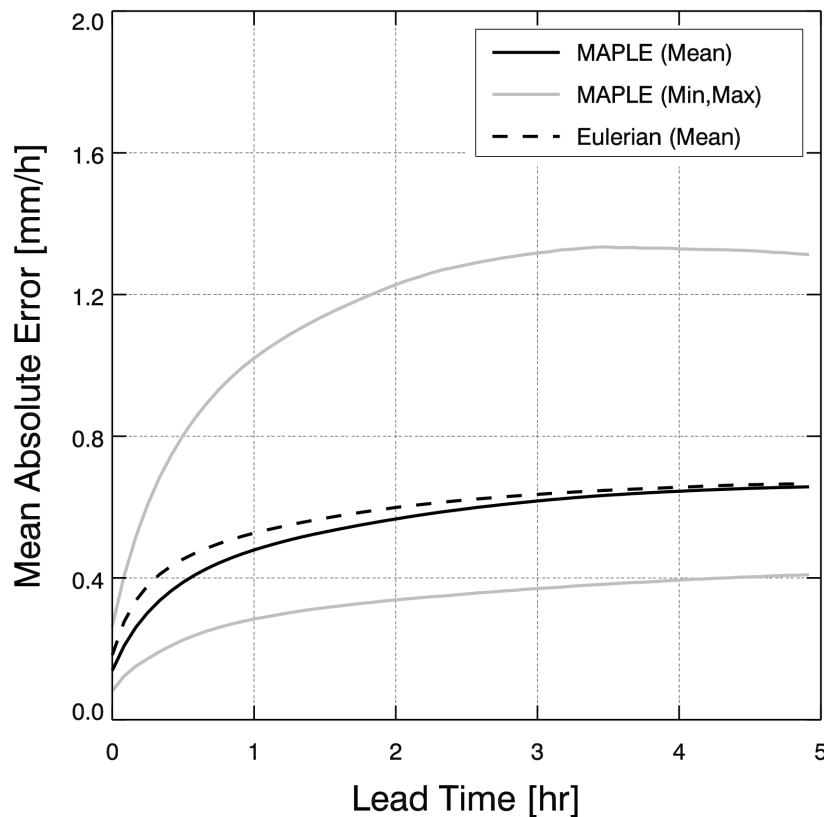
Figure A.8: *Mean absolute error (MAE) between observed and forecasted rainrate fields as a function of lead time. For each event, a single MAE vs lead time curve was estimated by comparing all the 5 min observed and forecasted fields for all the lead times. The solid dark line represents the 20-event average MAE, and the solid gray lines characterize event-to-event variability of MAE in MAPLE forecasts.*

of Germann and Zawadzki (2006) could be the presence of complex orography and its impact on the meteorological situation. As mentioned in the introduction, extrapolation techniques do not account for changes in the precipitation structure due to the orographic enhancement and dissipation. The size of the domain (2720 × 2720 km^2 in Germann and Zawadzki (2006) vs 620 × 620 km^2 in the current study) also plays a major role in the estimation of the correlations and the corresponding lifetimes. In a recent study (An investigation of the short-term predictability of precipitation using high-resolution composite radar observations by Ruzanski, E., and V. Chandrasekar submitted to Journal of Applied Meteorology and Climatology), the authors used high resolution (0.2 km) radar reflectivity fields with a spatial extent of 140 × 140 km^2 and reported lifetimes of Eulerian and Lagrangian forecasts to be around 15 min and 20 min respectively.

The correlations shown in figure A.9 were estimated by pooling together all the 5 min observed and forecast fields within an event. Therefore, we have one correlation function for each event and the corresponding lifetime represent the predictability of the event. To get an insight into the variability of lifetime within the event, we estimated the correlations for 5 min - 5 h forecast issued at each time step within the event. The lifetime at each time step was then estimated by fitting an exponential function. Figure A.10 shows the lifetime distribution for each of the 20 selected events in the form of boxplots. The events 07156 and 10183 display least variability in lifetimes whereas the event 07240 has highest variability and skewness.
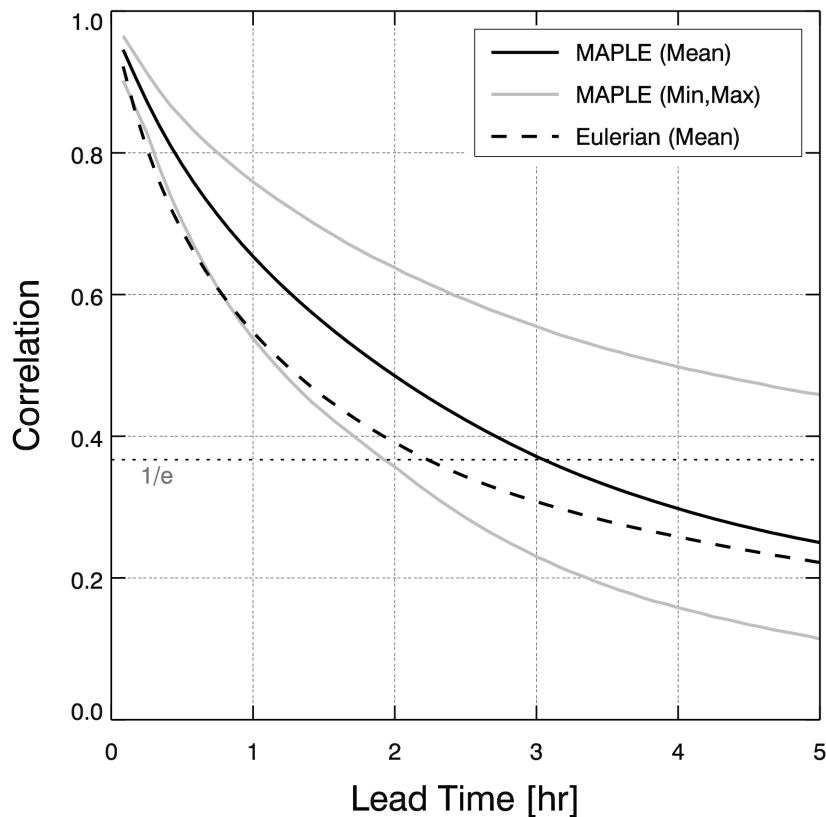
Figure A.9: *Correlation between observed and forecasted reflectivity fields as a function of lead time. For each event, a single correlation vs lead time curve was estimated by comparing all the 5 min observed and forecasted fields for all the lead times. The solid dark line represents the 20-event average correlation in MAPLE forecasts, and the solid gray lines characterize event-to-event variability in correlation. The lead time at which the correlation drops to 1/e (dark dotted line) is defined as the lifetime of forecasted fields. See section 5b for details.*

Germann and Zawadzki (2006) showed that the lifetime at each time step within the event depends on the precipitation area of the initial field. To further understand this dependence, we characterized the spatial structure of the initial reflectivity field at each time step using the spatial semivariogram described in section 4. The spatial semivariogram was then fitted with an elliptical Gaussian function (equations A.7 and A.8). That is, the spatial semivariogram of the reflectivity field at each time step was characterized in the form of major axis, minor axis and the eccentricity of the elliptical Gaussian function (see figure A.3 for an example). The correlations between observed and MAPLE forecast fields at lead times of 1 h, 2h, and 3h are plotted against the characteristics of the initial reflectivity field in figure A.11. The correlations were found to be higher for the reflectivity fields characterized by longer major and minor axis. It can be said that the MAPLE model results in better forecasts when the initial reflectivity fields are smoother in space. No such conclusion can be drawn for the relation between the eccentricity and the skill of MAPLE forecasts.

Neighborhood Evaluation

The verification results discussed so far were obtained by comparing pixel-to-pixel values at highest resolution. In this section we present the skill of MAPLE in forecasting the rainy area within spatial
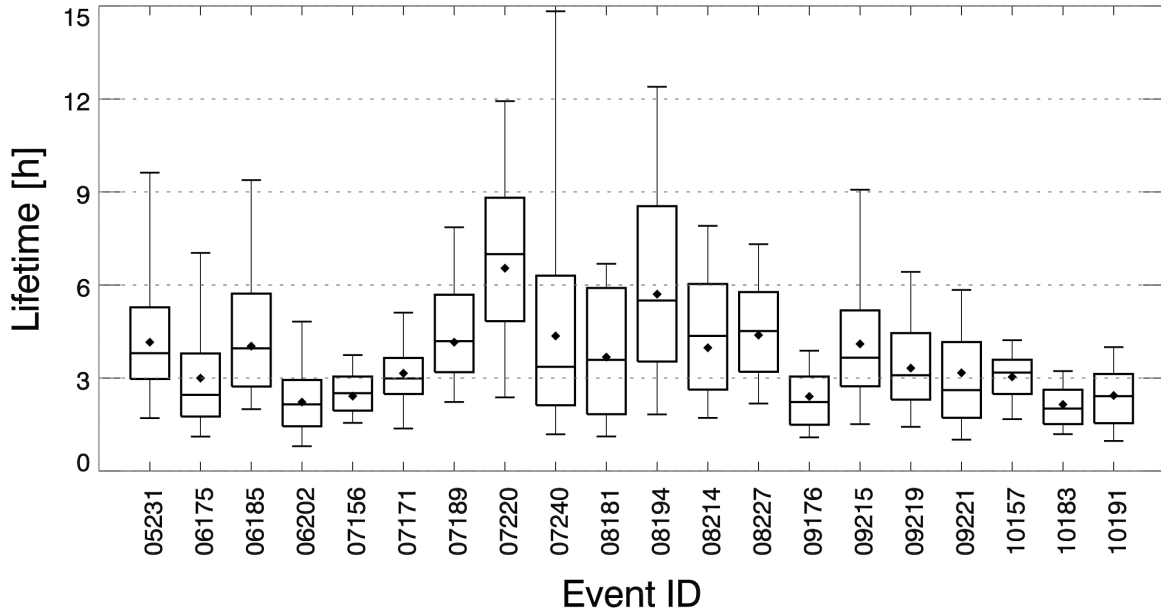
Figure A.10: *Distribution of MAPLE lifetimes at 5 min time scale for each of the selected events. The lifetimes obtained from figure A.9 are shown as solid diamonds. See text for details.*

neighborhood of varying sizes (3 km to 57 km). For each square neighborhood centered on pixels in observed and forecasted fields, the fractional observed (P_O) and forecasted (P_F) rainy areas were estimated by counting number of pixels exceeding a given Z_t value. Fractions skill score (FSS, section 5c) was then estimated using equation A.11. Figure A.11 shows the variation of average FSS of MAPLE and Eulerian persistence forecasts with the size of the spatial neighborhood for a fixed lead time of 3 h and different Z_t thresholds. The FSS was found to be lowest for the domain size of 3 km and increased with the size of the neighborhood. A non-zero FSS value for the smallest neighborhood size of 3 km implies reasonable skill even at that scales. For all the spatial scales, and for all three values of Z_t, the average FSS of MAPLE was found to be larger than that of Eulerian persistence forecasts (figure A.12). Similar to other verification scores, the FSS also decreased with the increase in the value of Z_t.

A.7.2 MAPLE, Eulerian and COSMO2: 12 Events

COSMO2 forecasts are available with a spatial resolution of 2.2 km and temporal resolution of 5 min. However the model is run every 3 h and it takes around 2 h for the latest run to be available because of data assimilation and dissemination. For each time step within the event, we had to take the 2 h lag time into account before selecting the appropriate COSMO2 run. The 2.2 km forecasts are regridded to 1 km so that we compare the results from COSMO2 with those from MAPLE and Eulerian persistence.

For each event we constructed the contingency tables for the lead times of 5 min to 5 h, and estimated the binary skill scores described in section 5. The 12-event average, minimum and maximum skill scores were then obtained and compared against the corresponding skill scores from MAPLE and Eulerian forecasts. Although we estimated all the skill scores, we present only the probability of detection (POD), false alarm ratio (FAR), and odds ratio (OR) in this section. From the figure A.13 it can be seen that COSMO2 forecasts have lower POD for shorter lead times. The POD of COSMO2 decreased with the increase in the lead time but not as rapidly as the extrapolation forecasts. The 12-event average POD curve of COSMO2 crossed the corresponding average MAPLE POD curve at
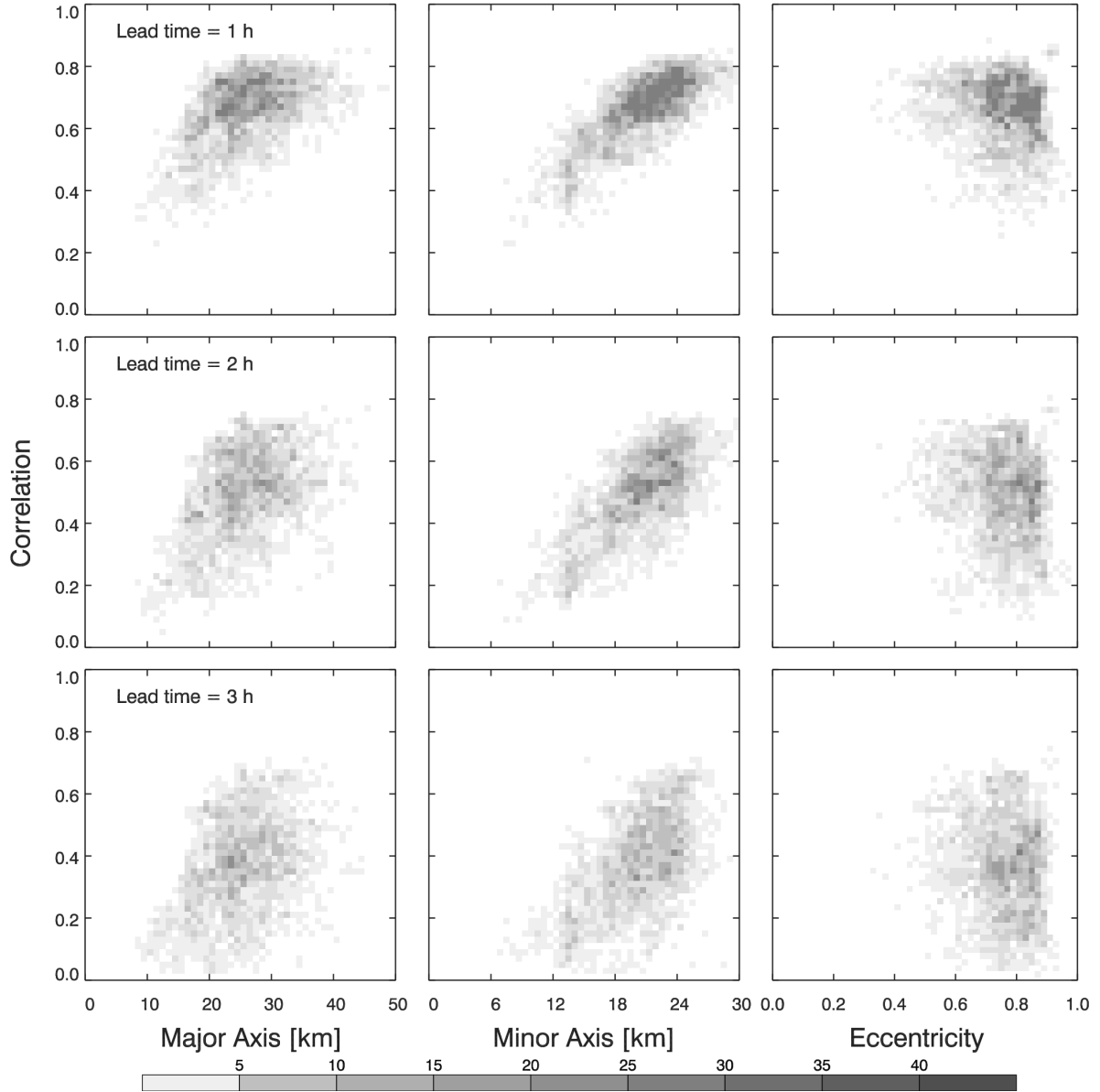
Figure A.11: *Scatter plot of MAPLE skill (correlation coefficient) against the smoothness (semivariogram) of the precipitation field. The color scale represents the number of points in each square.*

the lead times of 2 h, 2.2 h, and 2.4 h for the Z_t values of 10 dBZ, 25 dBZ, and 35 dBZ respectively. From the odds ratio results (bottom panels of figure A.13), it can be seen that the skill in COSMO2 forecasts exceeds the skill in MAPLE at lead times of 3.1 h, 2.6 h and 2.8 h for Z_t values of 10 dBZ, 25 dBZ, and 35 dBZ respectively.

As stated in the introduction, one of the objectives of this study is to find the crossover lead time beyond which the COSMO2 forecasts have better predictability than the extrapolation forecasts. Based on the binary verification scores presented in figure A.13 and by comparing other scores such as Gilbert skill score, and symmetric extreme dependence scores (figure not shown), we conclude that the crossover lead time is between 2 h and 3 h depending on the rain/no-rain threshold used.

We then estimated the correlation functions and the corresponding lifetimes for each of the 12 events. Figure A.14 shows the comparison of the 12-event average, minimum, and maximum correlation functions obtained from MAPLE, Eulerian and COSMO2 forecasts. Comparing the correlations of MAPLE and COSMO2 forecasts, it can be concluded that the average crossover time is around
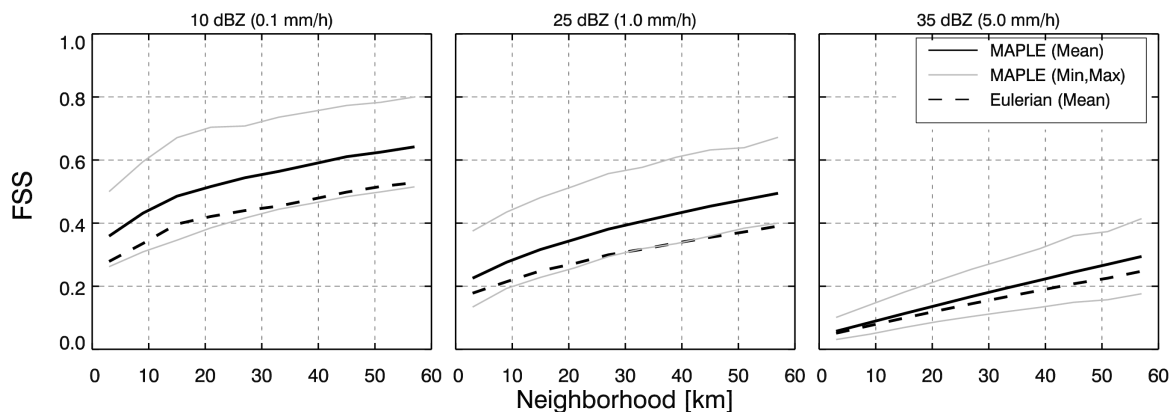
Figure A.12: *Fractions skill score (FSS) as a function of neighborhood size for a lead time of 3 h and for three rain/no-rain thresholds. For each event, a skill score vs neighborhood curve was estimated by comparing all the 5 min observed and forecasted fields. The solid dark line represents the 20-event average, and the solid gray lines characterize event-to-event variability in MAPLE skill.*

2.5 h with the minimum and the maximum values of 2.2 h and 3.2 h respectively (figure A.14). The 12-event average, minimum, and maximum MAE between the observed and forecast fields are shown in figure A.14. The crossover time based on MAE was found to be between 1.7 h and 2.7 h with an average value of approximately 2.4 h (figure A.15).

A.8   Orographic effects: Challenges and Future Plans

The main reason for the rapid decay of skill in extrapolation techniques is the lack of mechanism to account for the initiation, growth and dissipation of storms. As mentioned in the introduction, we aim to incorporate the effects of growth and dissipation into the MAPLE model to obtain improved rainfall nowcasts over the complex orography. We intend to approach the problem in a statistical manner, by training the MAPLE model using a large historical archive of radar-rainfall fields. The key is in arriving at a set of predictors based on archival dataset, and then using those predictors to incorporate the effect of orography into the output fields from MAPLE.

We believe that the orographic effect on the rainfall fields should be reflected in the velocity field estimated by the variational echo tracking algorithm. That is, any growth or blockage of rainfall patterns by the mountains should lead to reduction in the speed estimated from VET algorithm and should also affect the direction of the motion vectors . In the figure A.16, we show the average velocity field for the events 07189 and 10157. These fields were estimated by performing the weighted average of velocity fields at each time step within an event with the weights estimated as a function of the precipitation intensity. Note that weighting was performed to avoid the effect of interpolated motion vectors on the average velocity field.

The events shown in figure A.16 represent two extremes in the sense that for the event 07189, no effect of orography was seen in the motion vectors, and for the event 10157 the orographic effect is evident from the change in the velocity field above the Alps. The orographic effect can also be seen from the figure A.1, which shows the event scale accumulations. Therefore velocity field can be used as one of the predictors to induce the growth and dissipation of rainfall patterns. Another possible predictor is the time of the day. We are investigating the effect of diurnal variability on the performance of MAPLE. The forecast fields from the MAPLE model can therefore be corrected based on the time of the day.
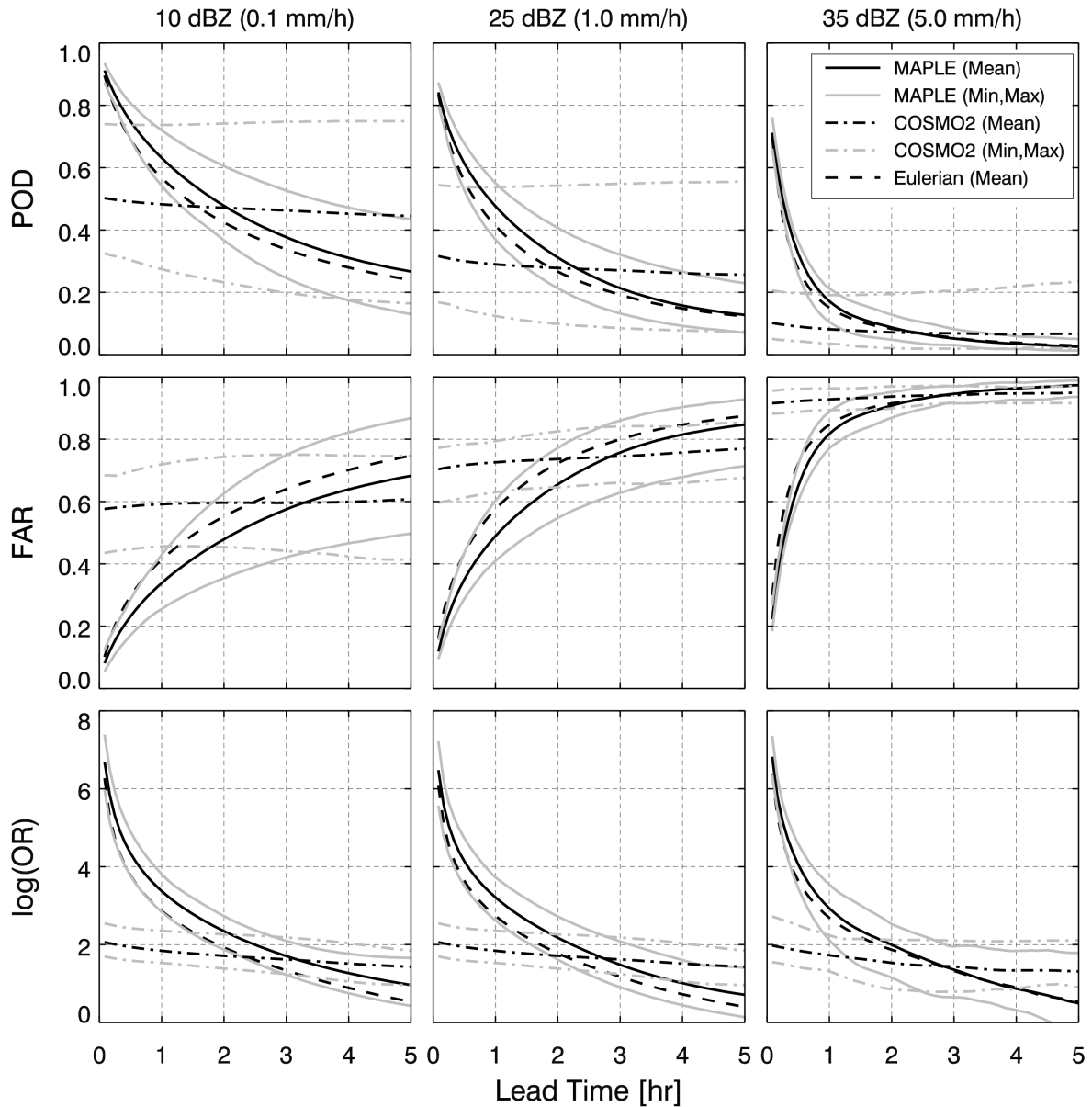
Figure A.13: *Probability of detection (POD), false alarm ratio (FAR), and odds ratio (OR) of MAPLE, Eulerian and COSMO2 forecasts as a function of lead time for three rain/no-rain thresholds.*

A.9 Summary and Conclusions

Very short-term forecasting (nowcasting) of precipitation at high spatial and temporal resolution is critical particularly for regions dominated with complex orography. In this study we carried out evaluation of high resolution forecasts from Eulerian, semi-Lagrangian (MAPLE), and numerical weather prediction models using 854 h of summer rainfall events between 2005 and 2010. Rigorous evaluation of 1 km, 5 min forecasts was performed using binary, continuous and neighborhood verification approaches. The forecasts from MAPLE outperformed Eulerian persistence forecasts for all the lead times and for different rain/no-rain thresholds. The results showed a relative gain of 1 h in lifetime of forecasts by adopting semi-Lagrangian extrapolation approach than simple Eulerian persistence.

Comparison of MAPLE forecasts with those obtained from the high resolution NWP model COSMO2 revealed that the extrapolation forecasts have much better skill for shorter lead times. However their skill decreased rapidly compared to NWP model output. The crossover lead time be-
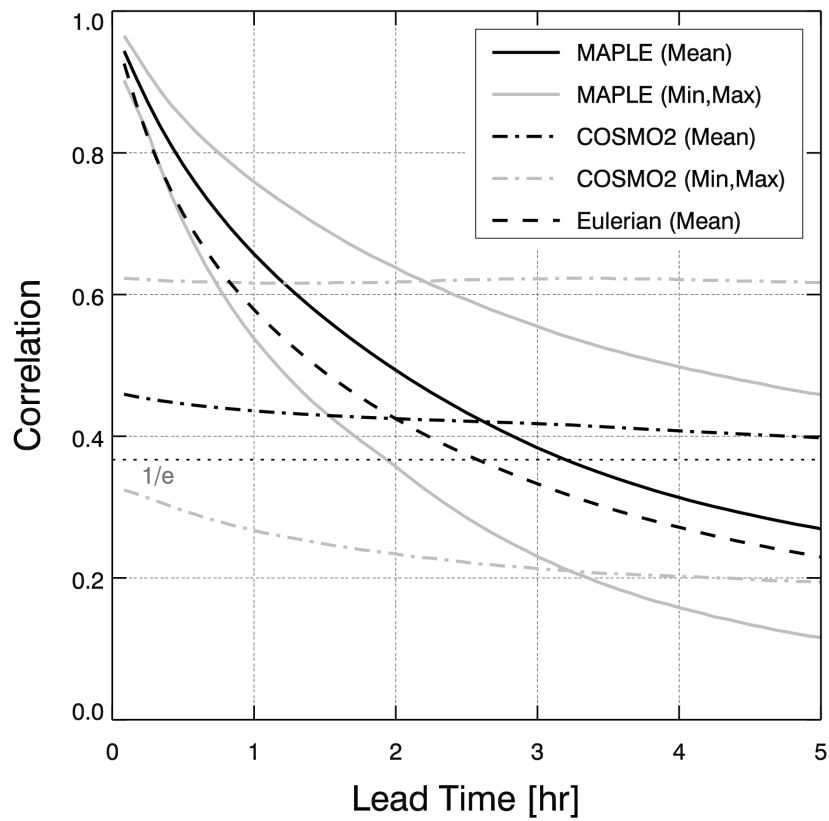
Figure A.14: *Correlation between 5 min observed and forecasted reflectivity fields obtained using Eulerian approach, COSMO2, and MAPLE.*

tween 5 min reflectivity fields with spatial resolution of 1 km. It also depends on the geography of the region and the meteorological situation. For example, Lin et al. (2005) compared the skill in hourly accumulations from four extrapolation and NWP model forecasts was found to be around 2.5 h for the different NWP models and radar nowcasts over U.S. and reported the crossover lead time to be around 6 h.
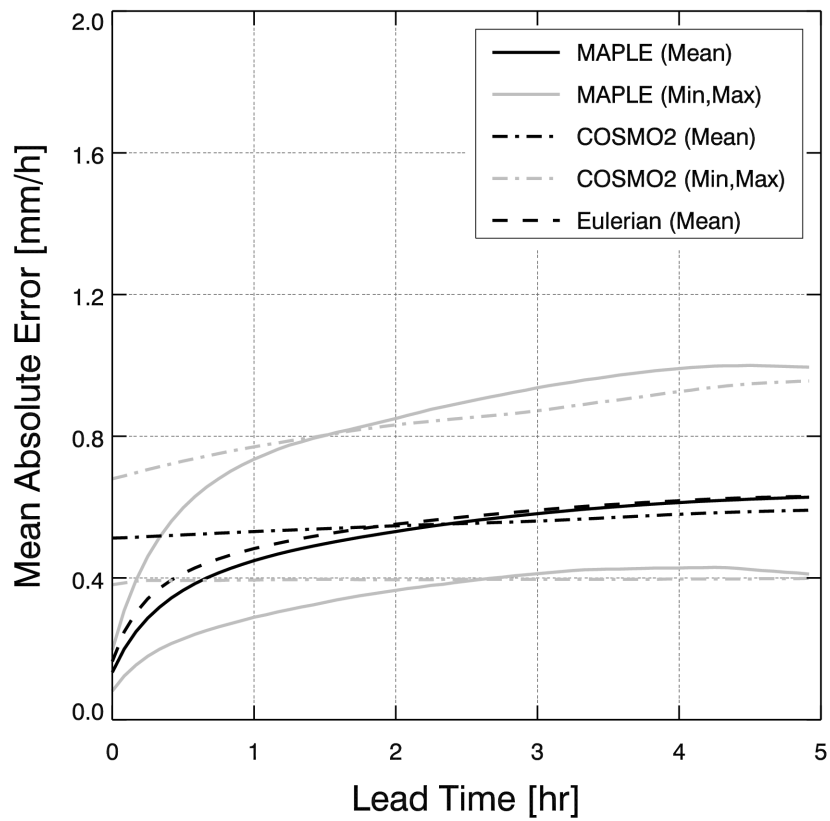
Figure A.15: *Mean absolute error in MAPLE, Eulerian, and COSMO2 forecasts as a function of lead time for for three rain/no-rain thresholds.*
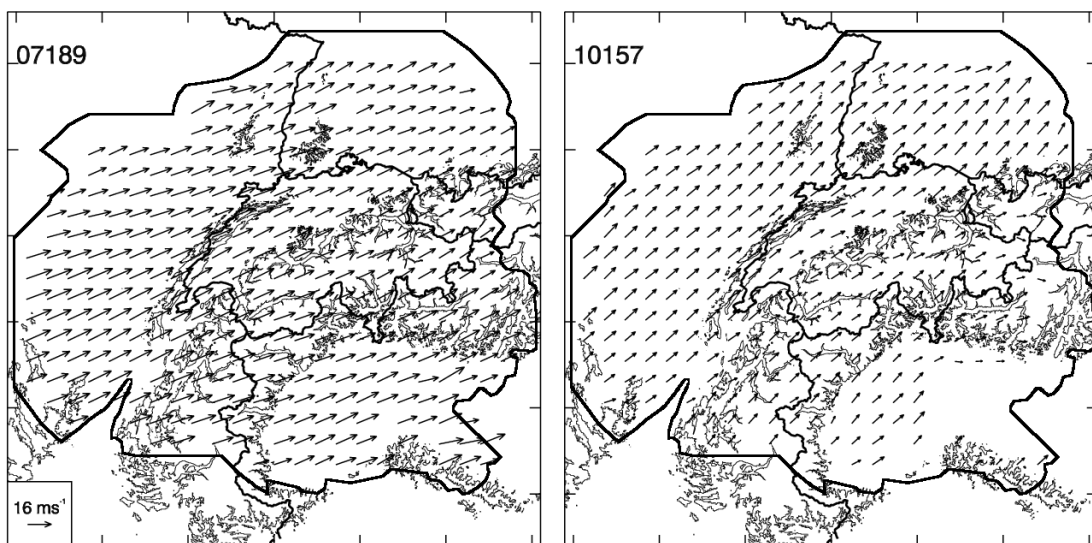

Figure A.16: *Average velocity field for the events 07189 and 10157.*

Bibliography

Ahrens, B., Jasper, K., and Gurtz, J.: On ALADIN precipitation modeling and validation in an Alpine watershed, Annales Geophysicae, 21, 627–637, 2003.

Alpert, P.: Mesoscale indexing of the distribution of orographic precipitation over high mountains., J. Climate. Appl. Meteor., 25, 532–545, 1986.

Alpert, P. and Shafir, H.: Mesogamma-scale distribution of orographic precipitation: numerical study and comparison with precipitation derived from radar measurements., J. Appl. Meteor., 1989.

Anders, A. M., Roe, G. H., Durran, D. R., and Minder, J. R.: Small-scale spatial gradients in climatological precipitation on the Olympic Peninsula., J. Hydrometeor., 8, 1068–1081, 2007.

Andrieu, H., French, M., Thauvin, V., and Krajewski, W. F.: Adaptation and application of a quantitative rainfall forecasting model in a mountainous region, Journal of Hydrology, 184, 243–259, 1996.

Atencia, A., Rigo, T., Sairouni, A., Moré, J., Bech, J., Vilaclara, E., Cunillera, J., Llasat, M. C., and Garrote, L.: Improving QPF by blending techniques at the Meteorological Service of Catalonia, Nat. Hazards Earth Syst. Sci., 10, 1443–1455, 2010.

Austin, G. L. and Bellon, A.: The use of digital weather radar records for short-term precipitation forecasting, Q. J. R. Meteorol. Soc., 100, 658–664, 1974.

Austin, P.: Relation between measured radar reflectivity and surface rainfall, Monthly Weather Review, 115, 1053–1070, 1987a.

Austin, P. M.: Relation between Measured Radar Reflectivity and Surface Rainfall, Mon. Wea. Rev., 115, 1053–1070, 1987b.

Bader, M. J. and Roach, W. T.: Orographic rainfall in warm sectors of depressions., Q. J. R. Meteorol. Soc., 103, 269–280, 1977.

Barros, A. P. and Lettenmaier, D. P.: Dynamic modeling of orographic induced precipitation., Rev. Geophys., 32, 265–284, 2010.

Barstad, I. and Smith, R. B.: Evaluation of an orographic precipitation model., J. Hydrometeor., 6, 85–99, 2005.

Bellon, A. and Austin, G. L.: The evaluation of two years of a real time operation of a short-term precipitation forecasting procedure (SHARP)., J. Appl. Meteor., 17, 1778–1787, 1978.

Bellon, A. and Austin, G. L.: The accuracy of short-term radar rainfall forecasts, Journal of Hydrology, 70, 35–49, 1984.

Bellon, A., Lee, G., and Zawadzki, I.: Error Statistics of VPR Corrections in Stratiform Precipitation, J. Appl. Meteor., 44, 998–1015, 2005.

Bellon, A., Zawadzki, I., Kilambi, A., Lee, H. C., Lee, Y. H., and Lee, G.: McGill Algorithm for Precipitation Nowcasting by Lagrangian Extrapolation (MAPLE) Applied to the South Korean Radar Network. Part I: Sensitivity Studies of the Variational Echo Tracking (VET) Technique, Asia Pacific Journal for Atmospheric Sciences, 46, 369–381, 2010.

Benestad, R. E., Hanssen-Bauer, I., and Chen, D.: Empirical-statistical downscaling, World Scientific, 2008.

Beniston, M.: August 2005 intense rainfall event in Switzerland: Not necessarily an analog for strong convective events in a greenhouse climate, Geophysical Research Letters, 33, L05701, 2006.

Berenguer, M., Corral, C., Sánchez-Diezma, R., and Sempere-Torres, D.: Hydrological Validation of a Radar-Based Nowcasting Technique, J. Hydrometeor., 6, 532–549, 2005.

Bergen, R. E. and Harnack, R. P.: Long-range temperature prediction using a simple analog approach., Mon. Wea. Rev., 110, 1083–1099, 1982.

Bergeron, T.: Preliminary results of Project Pluvius, IASH, Comm. Land. Eros., 53, 226–237, 1961.

Bo, L., Si-Xiong, Z., and Zhi-Gang, Y.: Forecasting the quasi-stationary front rainstorm in Southeast China using synthetically multilevel analog forecast technology., Atmospheric and Oceanic Science Letters, 2, 68–72, 2009.

Bougeault, P., Binder, P., Buzzi, A., Dirks, R., Houze, Jr., R. A., Kuettner, J., Smith, R. B., Steinacker, R., Volkert, H., and all MAP Scientists: The MAP Special Observing Period, Bull. Amer. Meteor. Soc., 82, 433–462, 2001.

Bousquet, O. and Smull, B. F.: Observations and impacts of upstream blocking during a widespread orographic precipitation event., Q. J. R. Meteorol. Soc., 129, 391–409, 2003.

Bowler, N., Pierce, C., and Seed, A.: Development of a precipitation nowcasting algorithm based upon optical flow techniques, Journal of Hydrology, 288, 74–91, 2004.

Bowler, N. E., Pierce, C. E., and Seed, A. W.: STEPS: A probabilistic precipitation forecasting scheme which merges an extrapolation nowcast with downscaled NWP, Q. J. R. Meteorol. Soc., 132, 2127–2155, 2006.

Brady, R. H. and Waldstreicher, J. S.: Observations of mountain wave-induced precipitation shadows over Northeast Pennsylvania, Wea. Forecasting, 16, 281–300, 2001.

Browning, K. and Collier, C.: Nowcasting of precipitation systems, Reviews in Geophysics, 27, 345–370, 1989.

Browning, K. A., Hill, F. F., and Pardoe, C. W.: Structure and mechanisms of precipitation and the effect of orography in a wintertime warm sector., Q. J. R. Meteorol. Soc., 100, 309–330, 1974.

Browning, K. A., Pardoe, C. W., and Hill, F. F.: The nature of orographic rain at wintertime cold fronts., Q. J. R. Meteorol. Soc., 101, 333–353, 1975.

Burlando, P., Montanari, A., and Ranzi, R.: Forecasting of storm rainfall by combined use of radar, rain gages and linear models, Atmospheric Research, 42, 199–216, 1996.

Cavalli, R.: Operational experience with the new generation of Swiss radars, in: COST-75 Advanced Weather Radar Systems — International Seminar, Locarno, pp. 159–164, 1998.

Collier, C. G.: Flash flood forecasting: What are the limits of predictability., Q. J. R. Meteorol. Soc., 133, 3–23, 2007.

Cornford, D.: A Bayesian state space modelling approach to probabilistic quantitative precipitation forecasting, J. Hydrol., 288, 92–104, 2004.

Cressie, N.: Statistics for Spatial Data, Wiley NY, 1993.

Delrieu, G., Creutin, J. D., and Saint-André, I.: Mean K-R Relationships: Practical Results for Typical Weather Radar Wavelengths, Journal of Atmospheric and Oceanic Technology, 8, 467–476, 1991.

Diomede, T., Nerozzi, F., Paccagnella, T., and Todini, E.: The use of meteorological analogues to account for LAM QPF uncertainty., Hydrol. Earth Syst. Sci., 12, 141–157, 2008.

Dolciné, L., Andrieu, H., and French, M.: Rainfall forecasting in a mountainous region using a weather radar and ground meteorological observations, Physics and Chemistry of the Earth, 22, 247–252, 1997.

Duband, D.: Reconnaissance dynamique de la forme des situations météorologiques. Application á la prevision quantitative des précipitations, PhD Thesis, Faculté des Sciences de Paris, France, 1970.

Dudis, J. J.: The stability of a saturated, stably-stratified shear layer., J. Atmos. Sci., 29, 774–778, 1972.

Durran, D. R.: Mountain waves and downslope winds, in: Atmospheric processes over complex terrain, pp. 59–81, W. Blumen, American Meteorological Society, Boston, USA, 1990.

Durran, D. R. and Klemp, J. B.: On the effects of moisture on the Brunt-Väisälä frequency., Journal of the Atmospheric Sciences, 39, 2152–2158, 1982.

Ebert, E.: Fuzzy verification of high–resolution gridded forecasts: a review and proposed framework, Meteorological Applications, 15, 51–64, 2008.

Ebert, E. E.: Neighborhood Verification: A Strategy for Rewarding Close Forecasts, Weather and Forecasting, 24, 1498–1510, 2009.

Ferretti, R., Low-Nam, S., and Rotunno, R.: Numerical simulations of the Piedmont flood of 4-6 November 1994., Tellus, 52, 162–180, 2000.

Foresti, L. and Pozdnoukhov, A.: Exploration of Alpine orographic precipitation patterns with radar image processing and clustering techniques., Meteorol. Appl., Submitted, 2011.

Fraedrich, K., Raible, C. C., and Sielmann, F.: Analog ensemble forecast of tropical cyclone tracks in the Australian region., Wea. Forecasting, 18, 3–11, 2003.

Fraser, A. B., Easter, R. C., and Hobbs, P. V.: A theoretical study of the flow of air and fallout of solid precipitation over mountainous terrain: Part I. Air flow model., J. Atmos. Sci., 30, 801–812, 1973.

Frei, C. and Schar, C.: A precipitation climatology of the Alps from high-resolution rain-gauge observations, International Journal of Climatology, 18, 873–900, 1998.

Gabella, M., Bolliger, M., Germann, U., and Perona, G.: Large sample evaluation of cumulative rainfall amounts in the Alps using a network of three radars, Atmospheric Research, 77, 256–268, 2005.

Georgakakos, K. P.: Design of national real-time warning system with capability for site-specific flash flood forecasts., Bull. Amer. Meteor. Soc., 67, 1233–1239, 1986.

Germann, U.: Vertical Wind Profile by SMA Doppler Weather Radars — A description of the Product, Technical report, Swiss Meteorological Institute, 1998.

Germann, U.: Radome attenuation — a serious limiting factor for quantitative radar measurements?, Meteorologische Zeitschrift, N.F., 8, 85–90, 1999.

Germann, U. and Joss, J.: Mesobeta Profiles to Extrapolate Radar Precipitation Measurements above the Alps to the Ground Level, J. Appl. Meteor., 41, 542–557, 2002.

Germann, U. and Joss, J.: Operational Measurement of Precipitation in Mountainous Terrain, in: Weather Radar: Principles and Advanced Applications, edited by Meischner, P., vol. XVII of Physics of Earth and Space Environment, chap. 2, pp. 52–77, Springer-Verlag, 2004.

Germann, U. and Zawadzki, I.: Scale-dependence of the Predictability of Precipitation From Continental Radar Images. Part I: Description of the Methodology, Mon. Wea. Rev., 130, 2859–2873, 2002.

Germann, U. and Zawadzki, I.: Scale-dependence of the Predictability of Precipitation From Continental Radar Images. Part II: Probability forecasts, J. Appl. Meteor., 43, 74–89, 2004.

Germann, U. and Zawadzki, I.: Predictability of Precipitation From Continental Radar Images. Part IV: Limits to prediction, J. Atmos. Sci., 63, 2092–2108, 2006.

Germann, U., Galli, G., Boscacci, M., and Bolliger, M.: Radar precipitation measurement in a mountainous region, Q. J. R. Meteorol. Soc., 132, 1669–1692, 2006.

Germann, U., Berenguer, M., Sempere-Torres, D., and Zappa, M.: REAL - Ensemble radar precipitation estimation for hydrology in a mountainous region, Q. J. R. Meteorol. Soc., 135, 445–456, 2009.

Göber, M., Wilson, C., Milton, S., and Stephenson, D.: Fairplay in the verification of operational quantitative precipitation forecasts, Journal of Hydrology, 288, 225–236, 2004.

Golding, B.: Nimrod: A system for generating automated very short range forecasts, Meteorol. Appl., 5, 1–16, 1998.

Grazzini, F.: Predictability of large-scale flow conducive to extreme precipitation over the Western Alps., Meteorology and Atmospheric Physics, 95, 123–138, 2007.

Grecu, M. and Krajewski, W. F.: A large-sample investigation of statistical procedures for radar-based short-term quantitative precipitation forecasting, J. Hydrol., 239, 69–84, 2000.

Hering, A., Morel, C., Galli, G., Sénesi, S., Ambrosetti, P., and Boscacci, M.: Nowcasting thunderstorms in the Alpine region using a radar based adaptive thresholding scheme, in: Proc. 3rd European Conf. on Radar Meteorology and COST-717 Final Seminar, 6–10 September 2004, Visby, Sweden, pp. 206–211, 2004.

Hill, F.: The use of average annual rainfall to derive estimates of orographic enhancement of frontal rain over England and Wales for different wind directions., Journal of Climatology, 3, 113–129, 1983.

Hobbs, P. V., Easter, R. C., and Fraser, A. B.: A theoretical study of the flow of air and fallout of solid precipitation over mountainous terrain: Part II. Microphysics., J. Atmos. Sci., 30, 813–823, 1973.

Hogan, R., O'Connor, E., and Illingworth, A.: Verification of cloud–fraction forecasts, Quarterly Journal of the Royal Meteorological Society, 135, 1494–1511, 2009.

Hogan, R., Ferro, C., Jolliffe, I., and Stephenson, D.: Equitability revisited: Why the "equitable threat score" is not equitable, Weather and Forecasting, 125, 710–7260, 2010.

Houze, Jr., R. A.: Cloud Dynamics, Academic Press, San Diego, USA, 1993.

Houze, Jr., R. A., James, C., and Medina, S.: Radar observations of precipitation and airflow on the Mediterranean side of the Alps: Autumn 1998 and 1999., Q. J. R. Meteorol. Soc., 127, 2537–2558, 2001.

Hutchinson, T. P.: A comment on correlation in skewed distributions., Journal of General Psychology, 124, 211–215, 1997.

James, C. N. and Houze, R. A.: A Real-Time four-dimensional Doppler dealiasing scheme, J. Atmos. Oceanic Technol., 18, 1674–1683, 2001.

James, C. N. and Houze, Jr., R. A.: Modification of precipitation by coastal orography in storms crossing Northern California., Mon. Wea. Rev., 133, 3110–3131, 2005.

Jaun, S., Ahrens, B., Walser, A., Ewen, T., and Schär, C.: A probabilistic view on the August 2005 floods in the upper Rhine catchment, Natural Hazards and Earth System Sciences, 8, 281–291, 2008.

Joliffe, I. and Stephenson, D. B.: Forecast Verification: A Practitioner's Guide in Atmospheric Science, John Wiley&Sons, Ltd, pp. 240, 2003.

Jolliffe, I.: The impenetrable hedge: a note on propriety, equitability and consistency, Meteorological Applications, 15, 25–29, 2008.

Joss, J. and Gori, E. G.: Shapes of Raindrop Size Distributions, J. Appl. Meteor., 17, 1054–1061, 1978.

Joss, J. and Lee, R.: The application of radar-gauge comparisons to operational precipitation profile corrections, Journal of Applied Meteorology, 34, 2612–2630, 1995.

Joss, J. and Waldvogel, A.: Precipitation measurement and hydrology, in: Radar in Meteorology: Battan Memorial and 40th Anniversary Radar Meteorology Conference, pp. 577–597, Amer. Meteor. Soc., Boston 1990, 1990.

Joss, J., Schädler, B., Galli, G., Cavalli, R., Boscacci, M., Held, E., Bruna, G. D., Kappenberger, G., Nespor, V., and Spiess, R.: Operational Use of Radar for Precipitation Measurements in Switzerland, vdf Hochschulverlag AG an der ETH Zürich, ISBN 3-7281-2501-6, 108pp, 1998.

Kappenberger, G. and Kerkmann, J.: Il tempo in montagna, Zanichelli, 1997.

Kitchen, M. et al.: Real-time correction of weather radar data for the effects of bright band, range and orographic growth in widespread precipitation, Q. J. R. Meteorol. Soc., 120, 1231–1254, 1994.

Koistinen, J., Michelson, D. B., Hohti, H., and Peura, M.: Operational Measurement of Precipitation in Cold Climates, in: Weather Radar: Principles and Advanced Applications, edited by Meischner, P., vol. XVII of Physics of Earth and Space Environment, chap. 3, pp. 78–114, Springer-Verlag, 2004.

Krajewski, W. F. and Smith, J. A.: Radar hydrology: rainfall estimation, Advances in Water Resources, 25, 1387–1394, 2002.

Kuo, Y. H. and Chen, G. T.-J.: The Taiwan Area Mesoscale Experiment (TAMEX): An overview, Bull. Amer. Meteor. Soc., 71, 488–503, 1990.

Lalas, D. P. and Einaudi, F.: On the correct use of the wet adiabatic lapse rate in stability criteria of a saturated atmosphere., J. Appl. Meteor., 13, 318–324, 1974.

Laroche, S. and Zawadzki, I.: A variational analysis method for retrieval of three-dimensional wind field from single-Doppler radar data, Journal of the atmospheric sciences, 51, 2664–2682, 1994.

Lee, G.-W. and Zawadzki, I.: Variability of Drop Size Distributions: Time-Scale Dependence of the Variability and its Effects on Rain Estimation, J. Appl. Meteor., 44, 241–255, 2005.

Lee, H. C., Lee, Y. H., Ha, J.-C., Chang, D.-E., Bellon, A., Zawadzki, I., and Lee, G.: McGill Algorithm for Precipitation Nowcasting by Lagrangian Extrapolation (MAPLE) Applied to the South Korean Radar Network. Part II: Real-Time Verification for the Summer Season, Asia Pacific Journal for Atmospheric Sciences, 46, 383–391, 2010.

Lee, W.-C., Wilson, J., Chen, Y.-L., Lin, Y.-L., Kuo, B., Fovell, R., Weckwerth, T., Sun, J., and Xiao, Q.: The Terrain-influenced Monsoon Rainfall Experiment (TiMREX): Scientific Overview Document, www.eol.ucar.edu/projects/timrex, 2007.

Leuenberger, D.: High-resolution radar rainfall assimilation: exploratory studies with latent heat nudging, Ph.D. thesis, ETH Zurich, 2005.

Leuenberger, D. and Rossa, A.: Revisiting the latent heat nudging scheme for the rainfall assimilation of a simulated convective storm., Meteorology and Atmospheric Physics, 98, 195–215, 2007.

Leuenberger, D. and Rossa, A. M.: Assimilation of Radar Information in aLMo, COSMO Newsletter (available at www.cosmomodel.org), 3, 164–172, 2003.

Liang, Q., Feng, Y., Deng, W., Hu, S., Huang, Y., Zeng, Q., and Chen, Z.: A composite approach of radar echo extrapolation based on TREC vectors in combination with model-predicted winds, Advances in Atmospheric Sciences, 27, 1119–1130, 2010.

Lin, C., Vasic, S., Kilambi, A., Turner, B., and Zawadzki, I.: Precipitation forecast skill of numerical weather prediction models and radar nowcasts, Geophysical Research Letters, 32, L14801, 2005.

Lorenz, E. N.: Atmospheric predictability as revealed by naturally occurring analogues., J. Atmos. Sci., 26, 636–647, 1963.

Mandapaka, P., Krajewski, W. F., Ciach, G. J., Villarini, G., and Smith, J. A.: Estimation of radar-rainfall error spatial correlation, Advances in Water Resources, 32, 1020–1030, 2009.

Mandapaka, P. V. and Germann, U.: Radar-rainfall error models and ensemble generators, in: Rainfall: State of the Science, edited by Testik, F. and Gebremichael, M., vol. 191 of Geophysical Monograph Series, American Geophysical Union, 2010.

Mandapaka, P. V., Villarini, G., Seo, B.-C., and Krajewski, W. F.: Effect of radar-rainfall uncertainties on the spatial characterization of rainfall events, Journal of Geophysical Research, 115, D17110, doi:10.1029/2009JD013366, 2010.

Mandapaka, P. V., Germann, U., Panziera, L., and Hering, A.: Evaluation of a radar-based lagangian extrapolation rainfall forecast technique (MAPLE) over complex orography, Wea. Forecasting, Submitted, 2011.

Mantilla, R., Gupta, V. K., and Mesa, O. J.: Role of coupled flow dynamics and real network structures on Hortonian scaling of peak flows, Journal of Hydrology, 322, 155–167, 2006.

Mecklenburg, S., Joss, J., and Schmid, W.: Improving the nowcasting of precipitation in an Alpine region with an enhanced radar echo tracking algorithm, J. Hydrol., 239, 46–68, 2000.

Medina, S. and Houze, J. R. A.: Air motions and precipitation growth in Alpine storms., Q. J. R. Meteorol. Soc., 129, 345–371, 2003.

Menabde, M., Veitzer, S., Gupta, V. K., and Sivapalan, M.: Tests of peak flow scaling in simulated self-similar river networks, Advances in Water Resources, 24, 991–999, 2001.

Mueller, C., Saxen, T., Roberts, R., Wilson, J., Betancourt, T., Dettling, S., Oien, N., and Yee, J.: NCAR auto-nowcast system, Weather and Forecasting, 18, 545–561, 2003.

Neiman, P. J., Ralph, F. M., White, A. B., Kingsmill, D. E., and Persson, P. O. G.: The statistical relationship between upslope flow and rainfall in California's Coastal Mountains: Observations during CALJET., Mon. Wea. Rev., 130, 1468–1492, 2002.

Neiman, P. J., , White, A. B., Ralph, F. M., Gottas, D. J., and Gutman, S. I.: A water vapour flux tool for precipitation forecasting., Water Management, 162, 83–94, 2009.

Novák, P., Březková, L., and Frolík, P.: Quantitative precipitation forecast using radar echo extrapolation, Atmospheric Research, 93, 328–334, doi:10.1016/j.atmosres.2008.10.014, 2009.

Obled, C., Bontron, G., and Garcon, R.: Quantitative precipitation forecasts: a statistical adaptation of model outputs through an analogues sorting approach, Atmospheric Research, 63, 303–324, 2002.

Panziera, L. and Germann, U.: The relation between airflow and orographic precipitation on the southern side of the Alps as revealed by weather radar, Q. J. R. Meteorol. Soc., 136, 222–238, 2010.

Pearson, K.: Notes on the history of correlation, Biometrika, 13, 25–45, 1920.

Pegram, G. G. S. and Clothier, A. N.: Downscaling rainfields in space and time, using the String of Beads model in time series model, Hydrol. Earth Syst. Sci., 5, 175–186, 2001.

Pierce, C., Ebert, E., Seed, A., Sleigh, M., Collier, C., Fox, N., Donaldson, N., Wilson, J., Roberts, R., and Mueller, C.: The Nowcasting of Precipitation during Sydney 2000: An Appraisal of the QPF Algorithms, Weather and Forecasting, 19, 7–21, 2004.

Pierce, C. E., Hardaker, P. J., Collier, C. G., and Haggett, C. M.: GANDOLF: a system for generating automated nowcasts of convective precipitation, Meteorol. Appl., 7, 341–360, 2000.

Press, W. H. et al.: Numerical Recipes in C — The Art of Scientific Computing, Cambridge University Press, 1992.

Radinovic, D.: An analogue method for weather forecasting using the 500/1000 mb relative topography., Mon. Wea. Rev., 103, 639–649, 1975.

Ralph, F. M., Persson, P. O. G., Reynolds, D., Nuss, W., Miller, D., Schmidt, J., Neiman, P. J., Bao, J. W., Jorgensen, D., Kingsmill, D., Toth, Z., Veldon, C., White, A., King, C., and Wurman, J.: The California Land-falling Jets Experiment (CALJET): objectives and designs of a coastal atmospheric-ocean observing system deployed during a strong El Nino, in: Pacific Northwest Weather Workshop, Seattle, WA., 1999.

Ralph, F. M., Neiman, P. J., Kingsmill, D. E., Perrson, P. O. G., White, A. B., Strem, E. T., Andrews, E. D., and Antweiler, R. C.: The impact of a prominent rain shadow on flooding in California's Santa Cruz Mountains: a CALJET case study and sensitivity to the ENSO cycle., Journal of Hydrometeorology, 4, 1243–1264, 2003.

Ralph, F. M., Neiman, P. J., and Wick, G. A.: Satellite and CALJET aircraft observations of atmospheric rivers over the eastern North-Pacific Ocean during the winter of 1997/1998., Mon. Wea. Rev., 132, 1721–1745, 2004.

Ralph, F. M., Neiman, P. J., and Rotunno, R.: Dropsonde observations in low-level jets over the Northeastern Pacific Ocean from CALJET-1998 and PACJET-2001: mean vertical-profile and atmospheric river characteristics., Mon. Wea. Rev., 133, 889–910, 2005.

Reyniers, M.: Quantitative Precipitation Forecasts based on radar observations: principles, algorithms and operational systems, Publication scientifique et technique 52, Royal Meteorological Institute of Belgium, 2008.

Rhea, J. O.: An objective orographically-based QPF aid for California, in: Western Region Technical Attachment, No.96-02. (www.wrh.noaa.gov/wrh/96TAs/TA9602/ta96-02.html), 1996.

Rinehart, R. E.: Radar for Meteorologists, Rinehart Publications (http://radarwx@aol.com), 2004.

Roberts, N. and Lean, H.: Scale–selective verification of rainfall accumulations from high-resolution forecasts of convective events, Monthly Weather Review, 136, 78–97, 2008.

Roberts, R., Sun, J., Nelson, E., Wilson, J., and Tsai, F. T.: Developing Applications for Nowcasting Heavy Rainfall over Complex Terrain, in: The Sixth European Conference on Radar in Meteorology and Hydrology, Sibiu, Romania, 2010.

Rodgers, J. L. and Nicewander, W. A.: Thirteen ways to look at the correlation coefficient., The American Statistician, 42, 59–66, 1988.

Roe, G. H.: Orographic Precipitation, Ann. Rev. Earth Planet. Sci., 62, 645–671, 2005.

Root, B., Knight, P., Young, G., Greybush, S., Grumm, R., Holmes, R., and Ross, J.: A fingerprint technique for major weather events., Journal of Applied Meteorology and Climatology, 46, 1053–1066, 2007.

Rotach, M. and co authors, .: MAP D-PHASE: Real-time demonstration of weather forecast quality in the Alpine region., Bull. Amer. Meteor. Soc., 90, 1321–1336, 2009.

Rotunno, R. and Ferretti, R.: Mechanisms of intense Alpine rainfall., Journal of the Atmospheric Sciences, 58, 1732–1749, 2001.

Rotunno, R. and Houze, R.: Lessons on orographic precipitation from the Mesoscale Alpine Programme., Q. J. R. Meteorol. Soc., 133, 811–830, 2007.

Ruosteenoja, K.: Factors affecting the occurrence and lifetime of 500 mb height analogues: a study based on a large amount of data., Mon. Wea. Rev., 116, 368–376, 1988.

Sawyer, J. S.: The physical and dynamical problems of orographic rain, Weather, 11, 375–381, 1956.

Schaake, J., Henkel, A., and Cong, S.: Applications of PRISM climatologies for hydrologic modeling and forecasting in the western U.S., in: 18th Conference on Hydrology, Seattle, WA., 2004.

Schmutz, C., Arpagaus, M., Clementi, L., Frei, C., Fukutome, S., Germann, U., Liniger, M., and Schacher, F.: Meteorologische Ereignisanalyse des Hochwassers 8. bis 9. August 2001, Arbeitsberichte der MeteoSchweiz 222, 2008.

Seed, A. W.: A Dynamic and Spatial Scaling Approach to Advection Forecasting, J. Appl. Meteor., 42, 381–388, 2003.

Sempere-Torres, D., Porra, J. M., and Creutin, J. D.: A general formulation for rain drop size distribution., J. Appl. Meteor., 33, 1494–1502, 1994.

Seo, D. and Smith, J.: Radar-based short-term rainfall prediction, Journal of Hydrology, 131, 341–367, 1992.

Sinclair, M. R.: A diagnostic model for estimating orographic precipitation., J. Appl. Meteor., 33, 1163–1175, 1994.

Smith, R. B.: The influence of the mountains on the atmosphere, in: Advances in Geophysics, vol. 21, pp. 87–230, Academic Press, 1979a.

Smith, R. B.: The influence of the mountains on the atmosphere, in: Advances in Geophysics, vol. 21, pp. 87–230, Academic Press, 1979b.

Smith, R. B.: Progress on the theory of orographic precipitation, in: Tectonics, Climate, And Landscape Evolution: Geological Society of America Special Paper 398. Chapter 1, S. D. Willet et al. Eds., Geological Society of America., 2006.

Smith, R. B. and Barstad, I.: A linear theory of orographic precipitation., J. Atmos. Sci., 61, 1377–1391, 2004.

Smith, R. B., Jiang, Q., Fearon, M. G., Tabary, P., Dorninger, M., Doyle, J. D., and Benoit, R.: Orographic precipitation and air mass transformation: an Alpine example, Q. J. R. Meteorol. Soc., 129, 433–454, 2003.

Smith, R. B., Barstad, I., and Bonneau, L.: Orographic precipitation and Oregon's climate transition, J. Atmos. Sci., 62, 177–191, 2005.

Sokol, Z., Kitzmiller, D., Pešice, P., and Guan, S.: Operational 0–3 h probabilistic quantitative precipitation forecasts: Recent performance and potential enhancements, Atmospheric Research, 92, 318–330, 2009.

Stephenson, D.: Use of the "odds ratio" for diagnosing forecast skill, Weather and Forecasting, 15, 221–232, 2000.

Steppeler, J., Doms, G., Schättler, U., Bitzer, H. W., a. Gassmann, Damrath, U., and Gregoric, G.: Meso-gamma-scale forecasts using the non hydrostatic model LM., Meteorology and Atmospheric Physics, 82, 75–96, 2003.

Stoelinga, M. T., Hobbs, P. V., Mass, C. V., Locatelli, J. D., Colle, B. A., Houze, R. A., Rangno, A. L., Bond, N. A., Smull, B. F., Rasmussen, R. M., Thompson, G., and Colamn, B. R.: Improvement of Microphysical Parameterization through Observational Verification Experiment (IMPROVE), Bull. Amer. Meteor. Soc., 84, 1807–1826, 2003.

Teweless, J. and Wobus, H.: Verification of prognosis charts., Bull. Amer. Meteor. Soc., 35, 455–463, 1954.

Toth, Z.: Long-range weather forecasting using an analog approach, J. Climate, 119, 1501–1511, 1991.

Tsonis, A. and Austin, G.: An evaluation of extrapolation techniques for the short-term prediction of rain amounts, Atmos.–Ocean, 19, 54–65, 1981.

Turner, B. J., Zawadzki, I., and Germann, U.: Predictability of Precipitation From Continental Radar Images. Part III: Operational Nowcasting Implementation (MAPLE), J. Appl. Meteor., 43, 231–248, 2004.

Van den Dool, H. M.: A new look at weather forecasting through analogues., Mon. Wea. Rev., 117, 2230–2247, 1989.

Van den Dool, H. M.: Searching for analogues, how long must we wait?, Tellus, 46A, 314–324, 1994.

Vasic, S., Lin, C., Zawadzki, I., Bousquet, O., and Chaumont, D.: Evaluation of precipitation from Numerical Weather Prediction models and satellites using values retrieved from radars, Monthly Weather Review, 135, 3750–3766, 2007.

Vignal, B., Andrieu, H., and Creutin, J. D.: Identification of Vertical Profiles of Reflectivity from Volume Scan Radar Data, Journal of Applied Meteorology, 38, 1214–1228, 1999.

Villarini, G. and Krajewski, W. F.: Review of the Different Sources of Uncertainty in Single Polarization Radar-Based Estimates of Rainfall, Surveys in Geophysics, 31, 107–129, 2010.

Webster, R. and Oliver, M. A.: Statistical Methods in Soil and Land Resource Survey, Oxford Univ. Press, 316pp, 1990.

Weusthoff, T., Ament, F., Arpagaus, M., and Rotach, M.: Assessing the benefits of convection permitting models by Neighborhood Verification-examples from MAP D-PHASE, Monthly Weather Review, 2010.

Wilks, D. S.: Statistical methods in the Atmospheric Sciences, Academic Press, 467pp, 1995.

Wilson, J.: Precipitation nowcasting: past, present and future, Sixth International Symposium on Hydrological Applications of Weather Radar, 2004.

Wilson, J. W., Feng, Y., Chen, M., and Roberts, R.: Nowcasting challenges during the Beijing Olympics: successes, failures, and implications for future nowcasting systems., Wea. Forecasting, 25, 1691–1714, 2010.

Yuter, S. E., Stark, D. A., Crouch, J. A., Payne, M. J., and Colle, B. A.: The impact of varying environmental conditions on the spatial and temporal patterns of orographic precipitation over the Pacific Northwest near Portland, Oregon., Journal of Hydrometeorology, accepted; doi:10.1175/2010JHM1239.1, 2011.

Zacharov, P. and Rezacova, D.: The effect of radar-based QPE on the Fractions Skill Score used at the QPF verification, Advances in Geosciences, 25, 91–95, 2010.

Zawadzki, I., Morneau, J., and Laprise, R.: Predictability of Precipitation Patterns: An Operational Approach, J. Appl. Meteor., 33, 1562–1571, 1994.

Zillgens, B., Merz, B., Kirnbauer, R., and Tilch, N.: Analysis of the runoff response of an Alpine catchment at different scales, Hydrology and Earth System Sciences Discussions, 2, 1923–1960, 2005.

Curriculum Vitae

Luca Panziera
born in Verona, Italy, on 25 August, 1982

Education

1988-1995	Primary and secondary school in Verona, Italy
1996-2001	High school in Verona (Don Nicola Mazza Institute, Liceo Classico)
Sept. 2001-March 2005	BSc in Meteorology at the University of Ferrara, Italy; thesis: Dynamic Climatology of snowfalls over Trentino
Summer 2004	Stage at Meteotrentino, Trento, Italy. Weather forecasts and study assessment of local probabilistic forecasts.
Sept. 2005-Sept. 2006	MSc in Weather, Climate and Modelling at the Department of Meteorology, University of Reading, United Kingdom; thesis: Weather developments leading to heavy snow in the South-Eastern Alpine region.
Nov. 2006-Dec. 2010	PhD Student at the Institute for Atmospheric Sciences, ETH, Zürich, Switzerland, working at MeteoSwiss, Locarno Monti, Switzerland, as part of European Project COST 731 (Nov. 2006 - Nov. 2009) and IMPRINTS (Dec. 2009 - Dec. 2010) thesis: Orographic Forcing, the key for heuristic nowcasting of rainfall in the Alps
Dec. 2010- Oct. 2011	Post-doctorate at MeteoSwiss, Locarno Monti, Switzerland

International Conferences

June 2007	International Conference on Alpine Meteorology, Chambery, France Oral presentation: Heuristic forecasting of orographic precipitation.
August 2007	AMS International Conference of Radarmeteorology, Cairns, Australia Poster presentation: Orographic forcing and Doppler winds, the key for nowcasting heavy precipitation in the Alps
May 2008	Joint MAP D-PHASE Scientific Meeting - COST 731 mid-term seminar, Bologna, Italy Oral presentation: Nowcasting of orographic precipitation using Doppler wind
August 2008	AMS Conference on Mountain Meteorology, Whistler, Canada Oral presentation: Orographic forcing and Doppler winds, the key for nowcasting heavy precipitation in the mountains
May 2009	International Conference on Alpine Meteorology, Rastatt, Germany Oral presentation: Probabilistic nowcasting of orographic rainfall
July 2009	First semester meeting IMPRINTS Project, Lugano, Switzerland
February 2010	IMPRINTS Project Meeting, Stresa, Italy. Oral presentations.
June 2010	IMPRINTS Project Meeting, Barcelona, Spain. Oral presentations.
September 2010	EMS Annual Meeting, Zürich, Switzerland Oral presentation: Evaluation of precipitation nowcasting techniques for the Alpine region

Supervision of students

Jeffrey Annis, 2008. *Describing the air flow responsible for heavy orographic precipitation using the Monte Lema radar.* MSc thesis, IACETH, Switzerland.
Davide Dalla Libera, 2009. *Stabilitá atmosferica e precipitazioni orografiche nell'area del Lago Maggiore.* BSc thesis, Universitá di Ferrara, Italy.

Scientific exchanges

August 2008: two weeks stay with S. Medina and R. Houze at the Department of Atmospheric Sciences, Seattle, University of Washington.
Three weeks collaboration with A. Atencia (Meteo Catalonia) during his STSM in Locarno Monti as part of COST-731.

Ronco S/Ascona, 20 November 2010

List of publications

Panziera, L. and B.Hoskins, 2007. Weather developments leading to heavy snow in the South-Eastern Alpine region. *Proceedings of International Conference on Alpine Meteorology 2007, Chambery, France, pp. 576-579.*

Panziera, L. and U. Germann, 2007. Heuristic forecasting of orographic precipitation. *Proceedings of International Conference on Alpine Meteorology 2007, Chambery, France, pp. 225-228.*

Germann, U. and L. Panziera, 2007. Which do you trust more: a radar echo 3 km above your head or a raingauge measurement 8 km away? *EGU General Assembly16-20 April 2007, Vienna, Austria.*

Panziera, L. and B. Hoskins, 2008. Large snowfall events in the south-eastern Alps. *Weather*, **63**: 88-93.

Panziera, L. and U. Germann, 2008. Orographic forcing and Doppler winds, the key for nowcasting heavy precipitation in the mountains. *Proceedings of the AMS Conference on Mountain Meteorology 2008, Whistler, Canada.*

Panziera, L. and U. Germann, 2010. The relation between airflow and orographic precipitation on the southern side of the Alps as revealed by weather radar. *Quarterly Journal of the Royal Meteorological Society*, **136**: 222-238.

Panziera, L., U. Germann, M. Gabella, P.V. Mandapaka, 2010. NORA - Nowcasting of Orographic Rainfall by means of Analogs. *Quarterly Journal of the Royal Meteorological Society*, submitted.

P. V. Mandapaka, U. Germann, L. Panziera and A. Hering, 2011. Evaluation of a radar-based lagangian extrapolation rainfall forecast technique (MAPLE) over complex orography. *Weather and Forecasting*, submitted.

Ringraziamenti

É passato un bel pó di tempo dai primi di agosto del 2006, quando una e-mail di Urs mi chiedeva se fossi ancora interessato ad un dottorato a Locarno Monti. A quei tempi non sapevo nemmeno dove si trovasse Locarno, e avevo solo una vaga idea di che cosa fosse il Canton Ticino. Da quel giorno Urs mi ha accompagnato in questa stupenda avventura con impegno, professionalitá e con tanta umanitá. É stato sempre molto stimolante per me discutere con lui. Urs: grazie di tutto!!

I would like to thank also Prof. Ulrike Lohmann, for having given me the opportunity to do a PhD far from Zürich, in ... die Sonnenstube der Schweiz. Many thanks also to the co-examiners Prof.Paolo Burlando and Prof. C. Mätzler. Even if we didn't have many contacts, they always supported my work.

Non avrei potuto trovare colleghi migliori a Locarno Monti: grazie di cuore a TUTTI per il vostro sostegno in questi anni. Mi sono sentito veramente parte di un team motivato in cui i rapporti sono andati ben oltre quelli puramente professionali. La passione di gka, l'entusiasmo di pam, l'esperienza di sza, la pazienza di mbc, le discussioni con mag, prm, e con tutti gli altri ... la lista sarebbe veramente troppo lunga per ricordarli tutti! Grazie LOM!!

E grazie cll per la pazienza, il sostegno, le training sessions, la sopportazione, le cene al Lungo, ...

La mia famiglia mi ha sempre sostenuto fin dall'inizio, non solo permettendomi di studiare ma anche dandomi la motivazione necessaria. Questa tesi é sicuramente frutto anche vostro. Grazie.

Motivazione alimentata anche dall'attivitá sportiva e dall'energia dell'acqua che corre. Grazie Ettore, grazie Alviano.